NEUTRON SOURCE RECONSTRUCTION FROM ONE-DIMENSIONAL IMAGER OF NEUTRONS AT THE Z FACILITY

A Dissertation

by

SIDNEY AUSTIN RICKETTS

Submitted to the Graduate and Professional School of
Texas A&M University
in partial fulfillment of the requirements for the degree of

DOCTOR OF PHILOSOPHY

Chair of Committee,	Jim Morel
Committee Members,	Sunil Chirayath
	Craig Marianno
	Peter Kuchment
	Michael Mangan
Head of Department,	Michael Nastasi

August 2024

Major Subject: Nuclear Engineering

ABSTRACT

Magnetized Liner Inertial Fusion is a concept fielded at Sandia National Laboratories' Z facility which uses deuterium fuel to produce 2.45 MeV neutrons upon reaching thermonuclear conditions. Characterizing the spatial structure of neutron production is expected to play a crucial role in improving the understanding of important unresolved physics. A one-dimensional imager of neutrons has been fielded on Z which allows emitted neutrons to pass through a tungsten rolled edge aperture and form an axially resolved neutron image on CR-39 based solid state nuclear track detectors. Image reconstruction methods have the ability to perform an inverse problem and produce an axial neutron emission profile, which to date has never been performed with this diagnostic. Here, an analytical forward model of the one-dimensional imager of neutrons has been developed, which produces instrument response function matrices needed for image reconstruction. Numerous image reconstruction methods are presented and tested in a sensitivity analysis of the forward model. A modified generalized expectation-maximization algorithm is then presented to reconstruct an axial neutron emission profile of the stagnated fusion plasma from experimental data. This approach is validated by comparing the reconstructed neutron emission profile to an x-ray emission profile provided by a time-integrated pinhole camera and shows quantitative agreement. It is expected that this spatial neutron emission information in conjunction to other diagnostics fielded on Z will improve our ability to resolve plasma conditions in future experiments.

DEDICATION

To my extraordinary mother, Ascension Ricketts, whose unconditional love has shaped my world.

ACKNOWLEDGMENTS

I would like to thank Dr. Jim Morel and Dr. Marvin Adams for patience, support, and encouragement throughout my time at Texas A&M. I am deeply grateful to my committee for their support throughout the numerous changes and advancements in this dissertation, with special appreciation to Dr. Michael Mangan for believing in me enough to undertake this project. I am also indebted to the multitude of friends and family members who have motivated me to reach this significant milestone. Above all, I would like to express my profound appreciation to my partner, Faithful Elizabeth Williams, for her unwavering love and support.

CONTRIBUTORS AND FUNDING SOURCES

Contributors

This work was supported by a dissertation committee consisting of Dr. Jim Morel as advisor, Dr. Sunil Chirayath and Dr. Craig Marianno of the Department of Nuclear Engineering, Dr. Peter Kuchment of the Department of mathematics, and Dr. Michael Mangan of Sandia National Laboratories. Further support was provided by Dr. Marvin Adams, Dr. David Fittinghoff, Dr. Petr Volegov, Dr. William Lewis, Dr. Owen Mannion, Dr. Jeffrey Fein, Dr. Adam Harvey-Thompson, and Dr. David Ampleford.

Experimental data from Chapter 5 was acquired by Gary Whitlow, Jose Torres, and Pat Cahall. The chemical etching and microscopic scanning was performed by Dr. Michael Mangan and Dr. Owen Mannion.

All other work conducted for the dissertation was completed by the student independently.

Funding Sources

Sandia National Laboratories is a multimission laboratory managed and operated by National Technology & Engineering Solutions of Sandia, LLC, a wholly owned subsidiary of Honeywell International Inc., for the U.S. Department of Energy's National Nuclear Security Administration under contract DE-NA0003525.

NOMENCLATURE

ICF	Inertial Confinement Fusion
DD	deuterium-deuterium
DT	deuterium-tritium
MagLIF	Magnetized Liner Inertial Fusion
ODIN	one-dimensional imager of neutrons
NIF	National Ignition Facility
HDPE	high density polyethylene
IRF	instrument response function
MCNP	Monte Carlo N-Particle Transport Code
SNR	signal-to-noise ratio
LSF	least squares fit
NNLSF	non-negative least squares fit
EM	expectation-maximization
MLE	maximum likelihood estimation
GEM	generalized expectation-maximization
MAP	maximum a posteriori
LHS	latin hypercube sampling
TIPC	time-integrated pinhole camera

TABLE OF CONTENTS

Page

LIST OF FIGURES

1. INTRODUCTION

1.1 Motivation

Sandia National Laboratories' Z facility is the world's largest pulsed power accelerator used to study high energy density and Inertial Confinement Fusion (ICF) science [1,2]. ICF is an approach to creating fusion reactions by compressing and heating a small mass of fusion fuel. Numerous diagnostics are fielded in ICF experiments to infer physical quantities related to the plasma and help to improve the performance of future ICF experiments.

Neutron imaging has long been used to investigate the performance of ICF experiments and improve the understanding of unresolved physics [3]. Different types of apertures, recording systems, and analysis methods are implemented in a diagnostic to attain information about the spatial distribution of neutrons in a plasma. The detection of hot spots, or areas of increased neutron production, provide insight into the efficiency of the fusion process. This information is critical in helping quantify how different experimental inputs lead to different experimental outputs.

In deuterium fuel, neutrons are produced through deuterium-deuterium (DD) or deuterium-tritium (DT) reactions

$$D + D \rightarrow \begin{cases} {}^{3}He(0.8\,MeV) + n(2.45\,MeV)\,50\% \\ p(3.02\,MeV) + T(1.01\,MeV)\,50\%, \end{cases} \tag{1.1}$$

$$D + T \rightarrow \alpha(3.6\,MeV) + n(14.1\,MeV). \tag{1.2}$$

In pure DD fuel, the primary interactions are DD reactions, while DT fusion occurs as a secondary reaction. Tritons are generated via Eq. 1.1 which interact with the background deuterium plasma and undergo DT reactions [4, 5]. The total neutron emission, or yield, of an experiment can be indicative of the fuel performance. Currently at the Z facility, primary DD yields of 1.1×10^{13} have been achieved using an experimental load design known as Magnetized Liner Inertial Fusion (MagLIF) [6].

A one-dimensional imager of neutrons (ODIN) [7,8] has been fielded at the Z facility to image neutrons emitted during thermonuclear reactions, and spatially resolve the neutron emission along the axial extent of the fuel column. We anticipate that data from ODIN will contribute to improving our understanding of the degree of liner mix into the fuel column and the symmetry of the fuel column. Previous analysis has only de-magnified the recorded images by the magnification of the diagnostic to approximate the neutron source emission profiles [8]. The objective of this research is to use image reconstruction to improve the imaging the spatial production of primary neutrons in stagnation columns of MagLIF experiments. This has shown to be successful for 2-D neutron imaging performed at the National Ignition Facility (NIF) [9]. Presented is an analytical forward model of ODIN, a sensitivity analysis of the forward model, source reconstruction of ODIN data with various methods, and finally fielding recommendations and future improvements for neutron imaging at the Z facility.

1.2 Magnetized Liner Inertial Fusion

Sandia's Z facility can store up to 22 MJ in its 36 capacitor banks and can discharge that energy in $\sim$100 ns. The resulting linearly rising pulse has a peak electrical power of 80 TW and a peak current of up to 30 MA [1]. Z's ability to compress matter to extreme pressures (>1 Mbar) makes it a valuable platform to study a wide range of high energy density (HED) physics. Figure 1.1 shows the $\sim$33 m cross section of Z with the various stages of pulse compression, a plot of the peak electrical power near 80 TW, and a photo of two workers inside the center section for scale.

MagLIF [6, 10, 11] experiments are a subset of ICF experiments performed on the Z facility to investigate thermonuclear fusion conditions. Figure 1.2 shows the three stages in a MagLIF experiment: magnetization, laser preheat, and compression. The DD fuel is held in a cylindrical beryllium tube, or liner, with dimensions of 1 cm tall, $\sim$4-6 mm diameter, and $\sim$0.5-1.5 mg/cm^3 [12]. During the magnetization stage, external field coils apply a 10-20 T axial magnetic field in order to suppress radial thermal conduction loss [5, 13]. A kilojoule-class laser [14] is used to preheat the fuel to 100's of eV through a thin CH window in order to reduce the required compression to reach fusion conditions [15]. Finally, the liner is compressed by the magnetic field

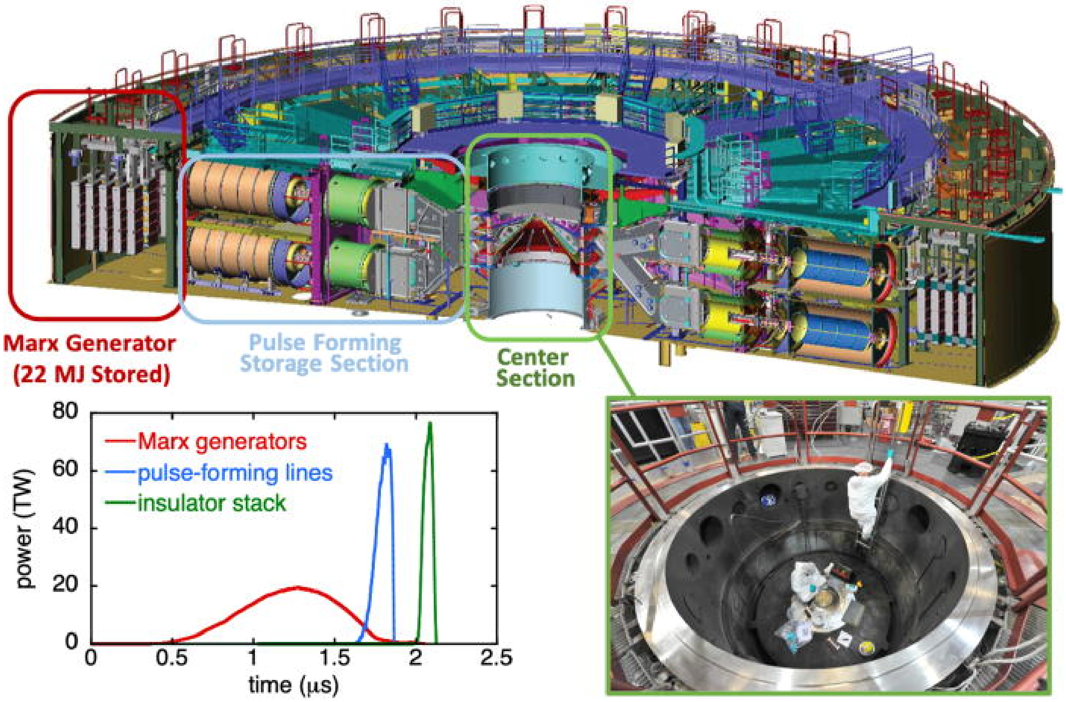

Figure 1.1: Cross section of Z ($\sim$33 m) showing the stages of pulse compression. A peak electrical power of 80 TW is capable as shown in the lower left plot. A photo of the center section with two workers is shown for scale in the bottom right [1].

generated from a $\sim$100 ns rise time 20 MA current generated by Z [16, 17, 18]. The resulting implosion produces an $\sim$1 cm tall < $\sim$100 μm wide neutron emitting stagnation column for $\sim$2 ns [11]. Present neutron yield levels of DD MagLIF experiments are $\sim 10^{12}$ to $\sim 10^{13}$ [6]. These yields limit the capability of neutron pinhole imaging, therefore a one-dimensional diagnostic was built for imaging MagLIF experiments [7].

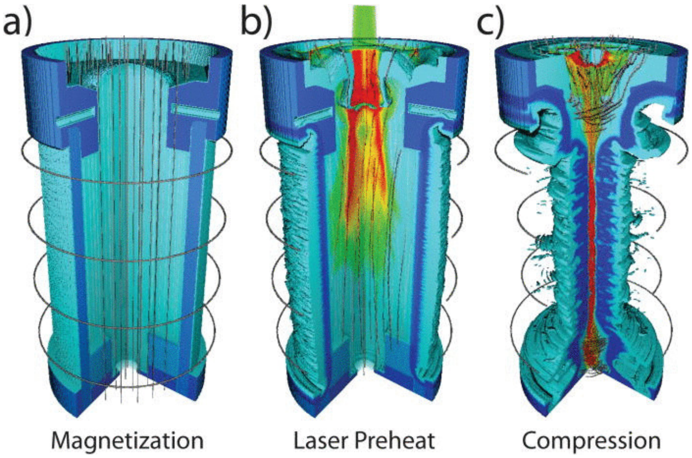

Figure 1.2: Three stages of MagLIF [10]. (a) Magnetization of the target with external magnetic field coils. (b) Laser preheating of target through CH window. (c) Pulsed power compression and implosion of target. Reprinted from [5], with the permission of AIP publishing.

1.3 One-Dimensional Imager of Neutrons

ODIN [8] consists of two rolled edge tungsten pieces placed between the experimental target and detector package as shown in Figure 1.3. There are two locations where detector packages can be mounted, the primary and secondary. The primary detector location is placed nominally 101.5 cm from the target, and the secondary is 17.75 cm in front of the primary (83.75 cm from the target). Neutrons emitted from the target during the experiment pass freely through the aperture or attenuate in the tungsten to reach the detector package. The entrance of the detector housing has a shield of stainless steel that allows neutrons to pass to the detector package, but blocks other particles produced in the nuclear reactions and to prevent debris from hitting the CR-39. The yellow area in Figure 1.3 represents the unattenuated path to reach the detectors.

1.3.1 Aperture

The aperture is held within a stainless steel housing and mounted by one end onto an aperture ring which surrounds the target. Each piece of tungsten has a radius of curvature of 50 cm, but only a height of five cm. The cuts on each side of the tungsten are manufactured asymmetrically about the apex of curvature. One cut is three cm from the apex and the other is seven cm, making the

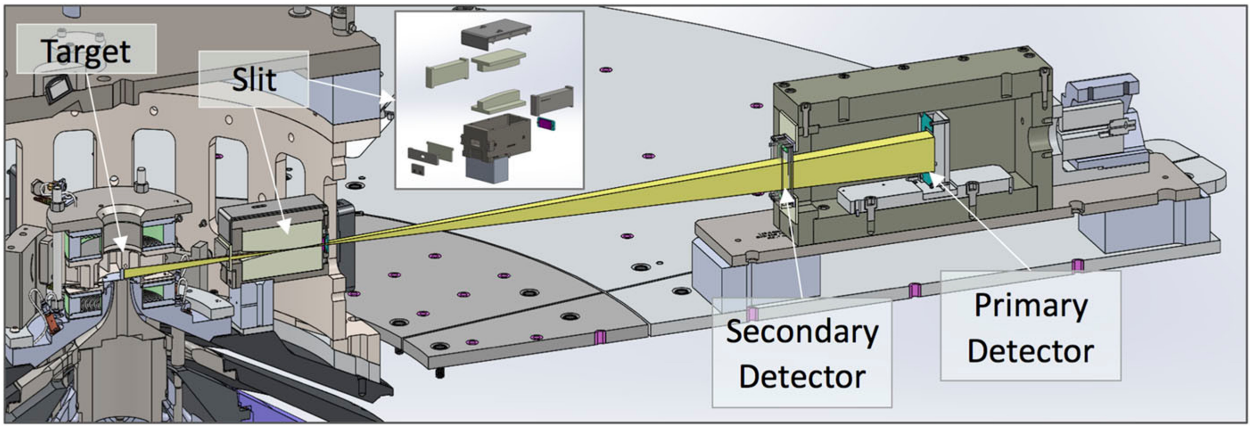

Figure 1.3: Summary of ODIN fielding. Yellow area is ray trace of unattenuated neutron path from the MagLIF target, through the tungsten aperture, to the detector housing. Reprinted from [8], with the permission of AIP publishing.

length of the aperture ten cm. The apex can be placed at 18 cm or 22 cm from the source by flipping the orientation of the aperture by 180 degrees. While changing the orientation moves the aperture apex, the housing itself does not change location on the aperture ring. Changing the orientation of the aperture alters the magnification of the image on the detector plane from 4.6 with the apex at 18 cm, and 3.6 with the aperture at 22 cm. The spacing size of the aperture is determined by tungsten spacers put in place on either side of the aperture. Options for the aperture spacing are 250 µm, 500 µm, and 750 µm. Images of the aperture and the mounted aperture housing are shown in Figure 1.4 (a) and 1.4 (b), respectively. The orientation shown is with the aperture apex located at 22 cm, orienting the larger aperture opening towards the source.

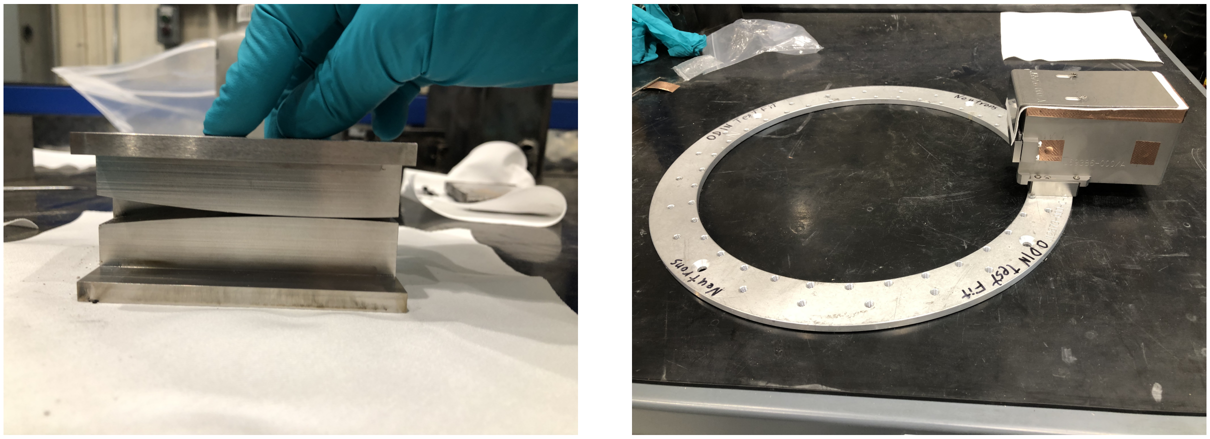

(a) (b)

Figure 1.4: (a) Image of 250 μm spaced tungsten aperture before being placed in aperture housing. (b) Aperture housing mounted to aperture ring.

1.3.2 Detector

ODIN uses multiple detector packages, each containing a 1 mm thick high density polyethylene (HDPE) converter foil and a 1 mm thick CR-39 nuclear track detector [19]. These detectors were chosen for ODIN because they can survive the harsh environment created during MagLIF experiments and are insensitive to the large x-ray background created by the source [20]. CR-39 is a transparent plastic in which charged particles leave latent destructive tracks along their trajectory. Neutrons that reach the detector can scatter elastically and produce recoil protons, which can also generate a latent track. The DD neutron efficiency on the front face (oriented towards the incoming neutrons) of CR-39 is 1.1×10^{-4} tracks per neutron and 3.3×10^{-4} tracks per neutron for the back face (oriented away from incoming neutrons) [20]. If HDPE is placed in front of the CR-39, forward scattering protons are generated within the HDPE and interact with the CR-39, thus increasing number of tracks observed on the front face.

ODIN's primary detector location places multiple 6x6 cm detector packages in row within a tungsten housing, as shown in Figure 1.5 (a). Alignment pins through the upper right and lower left corner of the detector packages keep them in place during the experiment. A serial number is laser etched onto the front back face of each CR-39 detector for identification. Figure 1.5 (b) shows a CR-39 detector and indicates the location of the alignment pinholes and serial number. Aligning multiple detector packages allows for multiple neutron images to be recorded during each experiment.

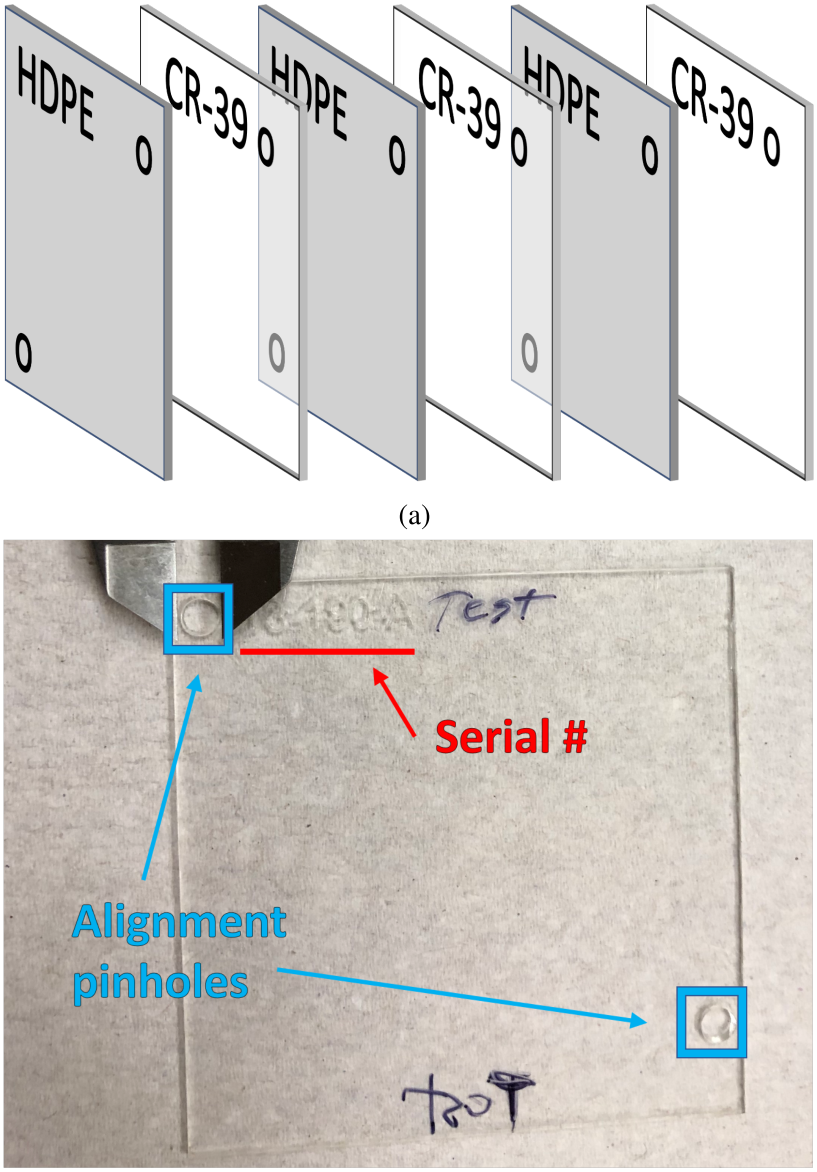

(a)

(b)

Figure 1.5: (a) Visualization of multiple CR-39 detector package setup within ODIN. (b) Image of CR-39 nuclear track detector with highlighted locations of alignment pinholes and etched identification serial number.

Following an experiment, a chemical etching process is performed to reveal the latent tracks in the CR-39 [21]. The etching process uses a sodium hydroxide solution to dissolve the surface layer of the CR-39. Areas of damage will have an increased etch rate compared to the rest of the surface and create conical pits, or tracks, on the surface of the CR-39. A microscopic scanning system then measures each pit's location, diameter, contrast, and eccentricity [22]. This can be performed on both the front and back face of each piece of CR-39. An example of a microscope imaged pieced of CR-39 exposed to 3.0 MeV protons is shown in Figure 1.6 [23]. Each track's diameter is related to the energy, charge, and atomic mass of the charged particle which generated the track [23]. The contrast measured is calculated as the percent difference of either the darkest pixel, or average pixel darkness of a track to the background brightness. We are interested in tracks on the etched surface which tend to be darker than the surrounding area. Intrinsic noise in the CR-39 often appears as lighter tracks, and can be caused by imperfections in the plastic or debris on the surface during the scanning process. The eccentricity of a track is measured by the track boundary in comparison to a perfect circle. Neutrons that enter from a non-incident path, such as those that scatter with in the Z environment, will leave a more eccentric track caused by the angle in which the charged particle was generated.

The discrimination settings used for ODIN data were determined by two primary parameters, eccentricity and contrast. Eccentricity can be set to a max upper limit of 10%, meaning only tracks with less than 10% of the max eccentricity were kept. Next, a plot of track contrast vs diameter is plotted at various contrast upper limits. This was performed to attempt to eliminate intrinsic noise from the CR-39 which is usually higher in contrast, and smaller in diameter as shown in the upper left of Figure 1.7 (b) and (c). As the contrast is lowered, a 2-D Gaussian distribution can be seen to be forming as shown in Figure 1.7 (d). This is believed to the be the distribution of generated tracks from the recoil protons induced within the CR-39.

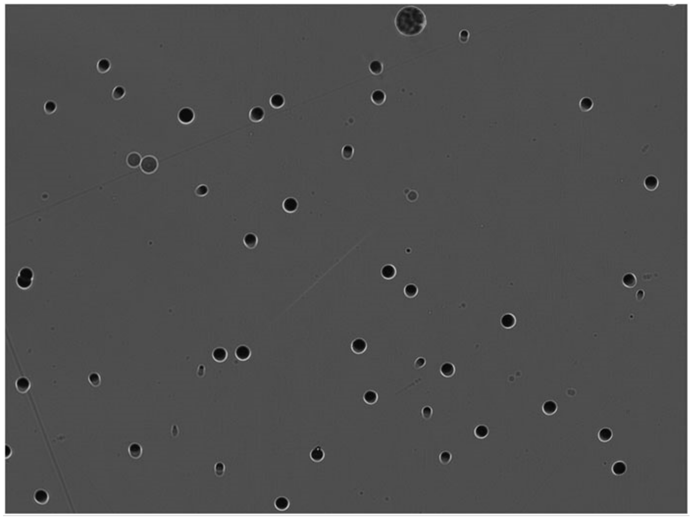

Figure 1.6: Microscopic image of CR-39 exposed to 3.0 MeV protons. Track diameter and contrast variations are related to the energy of the originating protons. Reprinted from [23], with the permission of AIP publishing.

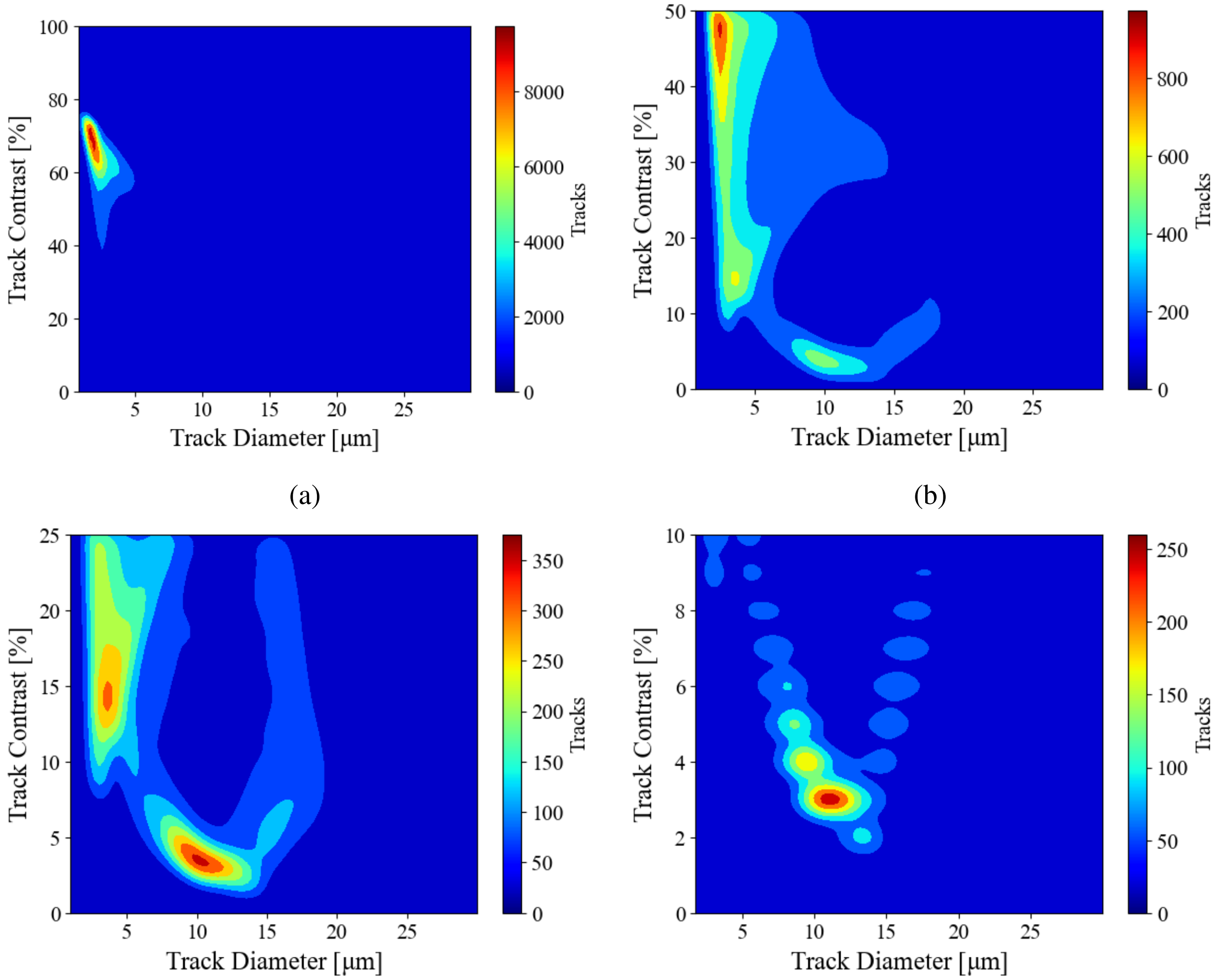

(a)

(b)

(c)

(d)

Figure 1.7: Contrast vs Diameter for ODIN CR-39 track data with decreasing contrast upper limit. (a) Shows a maximum contrast upper limit dominated by noise. Plots (b) and (c) are dominated by noise in the higher contrast and lower diameter regions. (d) Shows a 2-D Gaussian distribution formed, believed to be generated tracks from recoil protons induced within the CR-39.

1.3.3 Data

By using the track diameter, eccentricity and contrast, tracks due to primary neutrons passing through the aperture can be discriminated from tracks due to other sources, including intrinsic noise. The discrimination settings differ between front and back scans of CR-39 as the primary interactions which leave tracks differ. On the front face, most tracks are generated by the forward scattering recoil protons induced by the HDPE, but protons generated within the CR-39 are also present. However, on the back face, the HDPE does not increase the tracks generated and most are caused by recoil protons induced within the CR-39 itself. This leads to a broader distribution of track diameters on the front surface, as it has two sources of track generation, and a narrower distribution of track diameter on the back surface.

Once the data is discriminated, it can be binned to a resolution that provides reasonable statistics. Figure 1.8 shows the discriminated track data from MagLIF experiment z3289. ODIN's resolving axis is along the axial extent of the stagnation column, therefore, the data across the non-resolving axis is integrated to produce an axial detector response profile. In Figure 1.8 (a) there are significant drops in tracks at the edge of the CR-39, alignment pinholes, and etched serial number. When including these features, the integrated data will have non-physical decreases in counts at these locations. To account for this, Figure 1.8 (b) shows a subset of the scanned data which removes the edges, pinholes, and serial number. Figure 1.9 shows the integrated data across the non-resolving axis for the scans in Figure 1.8. The integrated cut data removes the decreases in signal near -2 and 2.5 cm, along with the sharp drop offs at the edge of the CR-39.

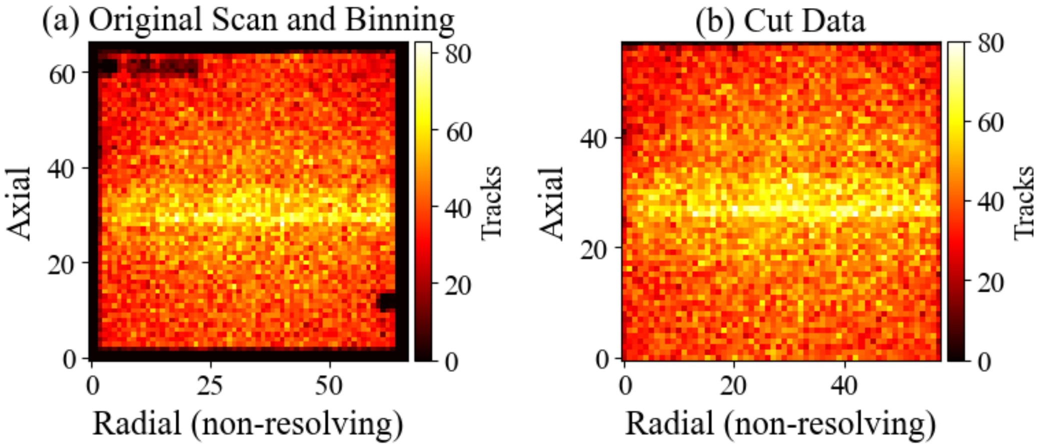

Figure 1.8: Discriminated CR-39 tracks for experiment z3289. (a) Binned ODIN data showing alignment pinholes and serial number. (b) Binned subset of data cut to remove alignment pinholes and serial number. Bin sizes are set to ∼900 μm.

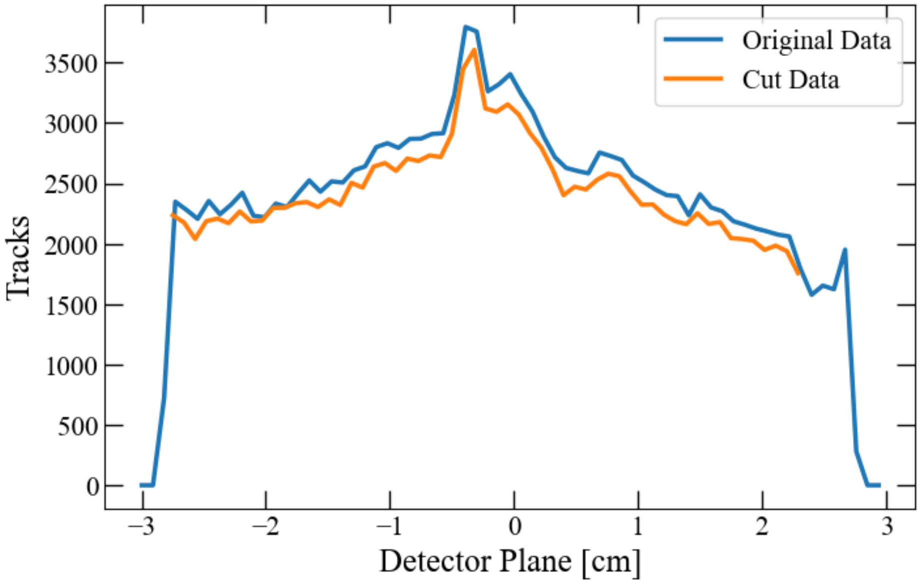

Figure 1.9: Integrated axial track data for z3289 original scan (blue solid) and subset cut data (orange solid).

1.4 Previous ODIN Data Analysis

Previous CR-39 analysis has only been performed at a rudimentary level [8]. CR-39 scans were discriminated and rebinned near the instrument's resolution (∼500 µm) as shown in Figure 1.10 (a). The rebinned data was then integrated along the non-resolving axis to produce a detector response profile. This response profile was rescaled by the magnification of the experiment (3.6), and inverted to approximate the neutron emission profile. Finally, the axial effective throughput and HDPE/CR-39 efficiency were incorporated into the approximate neutron emission profile. Information from x-ray imaging was used as a comparison to the axial neutron emission profile as shown in Figure 1.10 (b). X-ray data was used because it shares many of the same features of neutron emission profiles and has previously been measured with high accuracy. As stated previously, there have been no attempts to perform any type of source reconstruction on ODIN data.

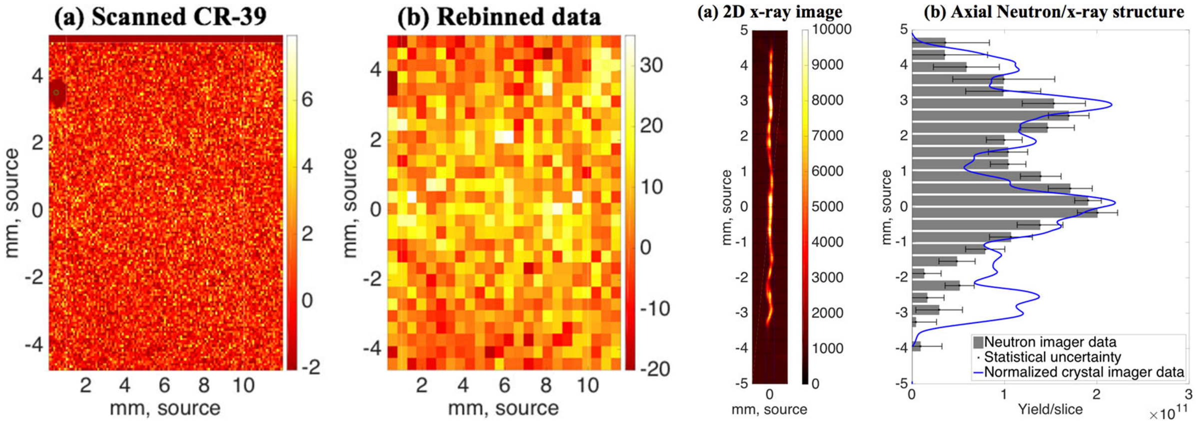

(a) (b)

Figure 1.10: (a) Scanned CR-39 at microscope resolution (left) and rebinned to ∼500 µm (right). (b) X-ray imaging of stagnation column (left) and comparison of axial emission structures (right). Reprinted from [8], with the permission of AIP publishing.

1.5 Image Reconstruction

Image reconstruction involves understanding the transformation process of a neutron producing source to the observed measurement. In MagLIF experiments, neutrons are emitted spatially along the burning plasma, transformed by the tungsten aperture and CR-39, resulting in observable tracks. This process can be represented mathematically by the Fredholm integral equation of the first kind, a tool typically used in various types of inverse problems such as image reconstruction. The generic equation has the form

$$\int_a^b P(x,y)G_0(y)\,dy = N_0(x), \quad c \leq x \leq d, \tag{1.3}$$

where $P(x,y)$ is the kernel/instrument response function (IRF) matrix that encapsulates the aperture and CR-39 transformation of the neutron source emission, $G_0(y)$, resulting in an observable measurement, $N_0(x)$. The observable in reality is distorted by noise, which is represented as

$$Y(x) = N_0(x) + noise. \tag{1.4}$$

It is common to discretize Eq. 1.3 since the data in question is commonly binned such as pixels in an image.

$$\sum_{j=1}^{m} P_{ij}G_j = Y_i, i = 1, 2, \ldots, n, \tag{1.5}$$

where P_{ij} is the IRF matrix, G_j is the neutron emission from source bin j, and Y_i is the observable measurement in detector bin i. The IRF matrix can be formed by any model that produces the appropriate transformation of a discretized source. Chapter 2 details the generation of IRF matrices using an analytical model of ODIN. If the IRFs and noise type can be estimated, different recovery methods can be performed to estimate the original source.

With the true source being unknown and the measurement distorted by noise, the problem is ill-posed. The criteria to be a well posed problem are: 1) the solution must exist, 2) the solution must be unique, and 3) the solution must be stable. In the case of neutron imaging, the first condition may not be met as the IRF matrix may not be an exact representation of the physical system, therefore, a solution may not exist. Also, if a solution exists, it may not be unique with the given IRF matrix. Stability of a solution involves the condition number of a matrix, which is the ratio of the highest to the lowest singular values from a singular value decomposition of the matrix. A high condition number will propagate noise from the measurement into large variations in the solution, creating instability.

With the IRF and noise estimations, direct matrix inversion or iterative recovery methods can be implemented to estimate the source. Direct matrix inversion methods involve calculating a solution directly from a system of linear equations. Iterative methods are algorithms that iterate towards a solution. To ensure that a solution exists, one can search for a solution in "weak form" which minimizes some functional difference between the model and experimental data. Imposing other conditions onto the solution can attempt to make the solution unique and stable. This is known as "regularization" and can include constraints such as non-negativity or smoothing criteria. A description of reconstruction techniques is presented in Chapter 3.

2. ODIN FORWARD MODEL

As previously shown in Eq. 1.3, the IRF matrix is key in performing image reconstructions. In order to develop the IRF matrices needed for image reconstruction, an analytical forward model has been developed based on some of the parameters of ODIN. This chapter outlines an analytical forward model of ODIN, including key assumptions and approximations. To ensure the validity of this model, a comparison is made to an IRF matrix formulated from Monte Carlo N-Particle Transport Code (MCNP) [24, 25]. Finally, an example of synthetic data generation using the forward model is shown.

2.1 Analytical Forward Model

The analytical forward model of ODIN is a generated from a 2-D representation of the system because there is no resolving power in the radial axis. Figure 2.1 shows a 2-D diagram of the forward model (not to scale). The neutron emitting source region is shown in solid red at the source plane and the CR-39 detector region is shown in blue at the detector plane. A centralized point source's neutron paths are shown in shades of dark blue as unattenuated and light blue as attenuated. A second point source at the lowest extent of the source is generating neutron paths similarly in shades or orange. For a 1 cm tall source, the CR-39 detector has a direct unattenuated neutron path for any point along the source. Each source points remaining attenuated signal is collected across the entire detector region.

The forward model of ODIN has a series of initial assumptions made to simplify the model. First, the neutron emitting source region is a zero diameter line source, rather than the volumetric region of burning plasma. There is also no region of liner material that neutrons would need to attenuate through. For 2.45 MeV neutrons, approximately 15% of neutrons scatter off a beryllium liner with an areal density of 1 g/cm^2 [26]. Of these interactions, approximately 95% are elastic scatters which still interact with the CR-39 detector (or HDPE converter foil) at a lower energy. Therefore, the overwhelming majority of signal is from unattenuated neutrons from the plasma

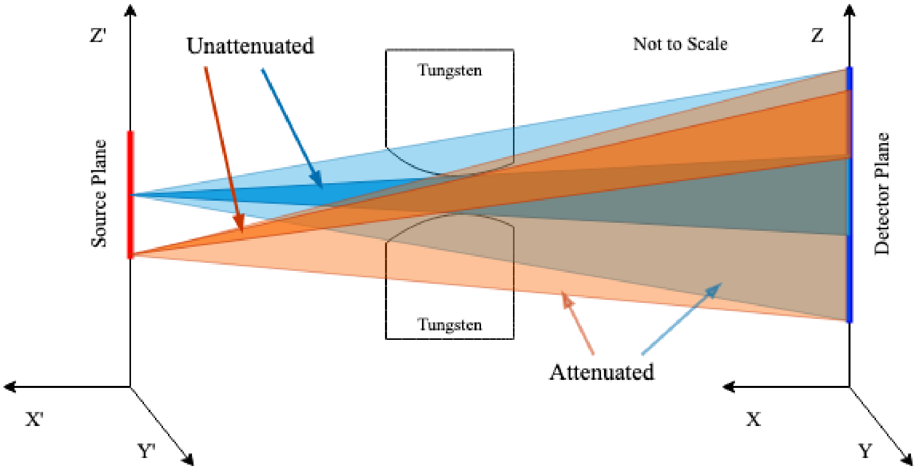

Figure 2.1: 2-D model of ODIN components including source area (red line), detector area (blue line) and tungsten aperture (not to scale). Possible attenuated and unattenuated neutron paths from two point sources to detector plane are shown in light blue/orange and dark blue/orange shaded regions, respectively.

column. Second, source points along the line source isotropically emit neutrons. This is indicated in Figure 2.1, where neutron paths reach the entire detector region. Third, scattered neutrons are neglected in the model, and only attenuation through the aperture is calculated. In the data discrimination process, described in Section 1.3.3 tracks with high eccentricity and contrast are removed. This is an attempt to eliminate contributions from scattered neutrons, which reach the detector from angles other than through the aperture region. Finally, the neutron path length in the CR-39 is set to 1 mm, or the thickness of the CR-39 itself.

The derivation for the IRF matrices is as follows. Neutrons are emitted from a line source with density defined as

$$\int_{z}^{z+\Delta z} S(z)\,dz, \tag{2.1}$$

where $S(z)$ is the neutrons emitted per source bin of Δz height along the source plane. Scalar fluence at a point on the CR39 piece is defined as

$$\phi(x,y,z) = \int_{\Delta z_{src}} S(z')\,dz' \frac{e^{-\tau(x,y,z,z')}}{4\pi d(x,y,z,z')^2}, \tag{2.2}$$

where $e^{-\tau(x,y,z,z')}$ is the attenuation of neutrons through tungsten, and $d(x,y,z,z')$ is the distance from the source plane emission to the detector plane interaction point. We are interested in determining the total tracks generated from interactions in a volumetric detector bin i

$$Tracks(bin\!:\!i) = \int_{\Delta x_{CR39}} dx \int_{\Delta y_{CR39}} dy \int_{\Delta z_i} dz\, \Sigma_s^{HDPE} \phi(x,y,z), \tag{2.3}$$

where Σ_s^{CR39} is the macroscopic scattering cross section of HDPE.

A series of approximations were then made to numerically solve for the number of tracks in a piece of CR-39. The line source is divided into quadrature point sources z_p with spacing Δz_p within source bin b with spacing Δz_b. The x distance from the source plane to image plane is a set value of x_d. This distance is much larger than the width of the detector piece (101.5:6 cm) and ODIN only has resolving power along the z-axis. Therefore, the assumption is made that the influence of detector position change in the y axis is zero. Midpoint approximations allow the x and y integrals in equation (2.3) to be simplified to Δx_{CR39}, the thickness of the CR39 piece in the x-axis, and Δy_{CR39}, the width of the CR39 piece in the y-axis. The z integral in equation (2.3) is divided similarly to the line source. The detector plane interactions are divided into quadrature points z_h with spacing Δz_h within detector bin i with spacing Δz_i. These approximations allow the scalar fluence from equation (2.2) to be approximated as

$$\phi(x,y,z) \approx \sum_b \sum_{p \in b} \Delta z_p S_b \frac{e^{-\tau(x,0,z,z_p)}}{4\pi[x^2 + (z_h - z_p)^2]}, \tag{2.4}$$

where S_b is the number of neutrons emitted from source bin b. Leaving the model approximation for detector bin i response from source bin b as

$$Tracks(bin\!:\!i) \approx \Sigma_s^{HDPE} \Delta x_{CR39} \Delta y_{CR39} S_b \Delta z_i \Delta z_b \underline{\sum_{h \in i} \frac{\Delta z_h}{\Delta z_i} \sum_{p \in b} \frac{\Delta z_p}{\Delta z_b} \frac{e^{-\tau(x,0,z,z_p)}}{4\pi[x^2 + (z_h - z_p)^2]}}. \tag{2.5}$$

Equation (2.5) is written such that the underlined portion can be plotted as the scalar fluence on the detector plane. If there is only one point source per source bin, the model will produce the point spread functions shown in Figure 2.2. This image shows generated spread functions for 21 source points spaced every 0.05 cm along a 1 cm tall source profile. These point spread functions have a flat top from the unattenuated neutron paths, such as the dark blue/orange shaded regions in Figure 2.1. The long tails of each function are caused by the attenuation through the tungsten aperture, such as the light blue/orange shaded regions in Figure 2.1. As the source point moves up or down the source plane, the aperture spacing seen by the emitting source becomes smaller, hence the decreasing size in the point spread function flat tops. It can be seen that all the point spread functions for a 1 cm tall source have a direct line of sight to the detector region. However, this is not the case when the aperture orientation is changed, and the apex is placed 18 cm from the source.

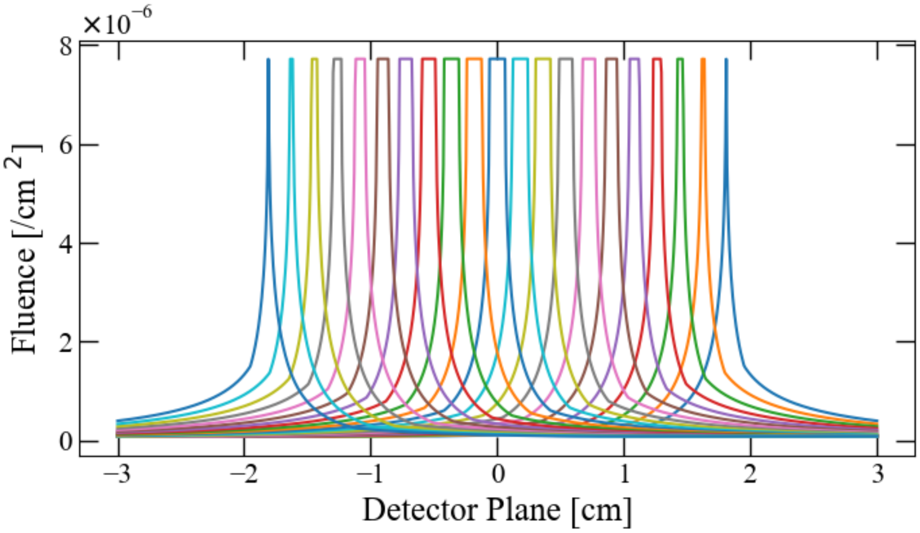

Figure 2.2: Scalar fluence at the detector plane for 21 point spread functions generated from evenly spaced source points every 0.05 cm along a 1 cm tall source profile.

If multiple point sources are used per bin, the point spread functions from each bin are averaged with one another. Figure 2.3 (a) shows a high fidelity line spread function from 21 source bins, each containing 14 source points, at every interaction point on the detector. Figure 2.3 (b) has the detector interactions averaged to the number of chosen detector bins, which is representative of the underlined portion of Eq. 2.5. The IRF matrix used for reconstructions will be a variation of Figure 2.3 (b) with a chosen number of source bins (number of columns) and detector bins (number of rows).

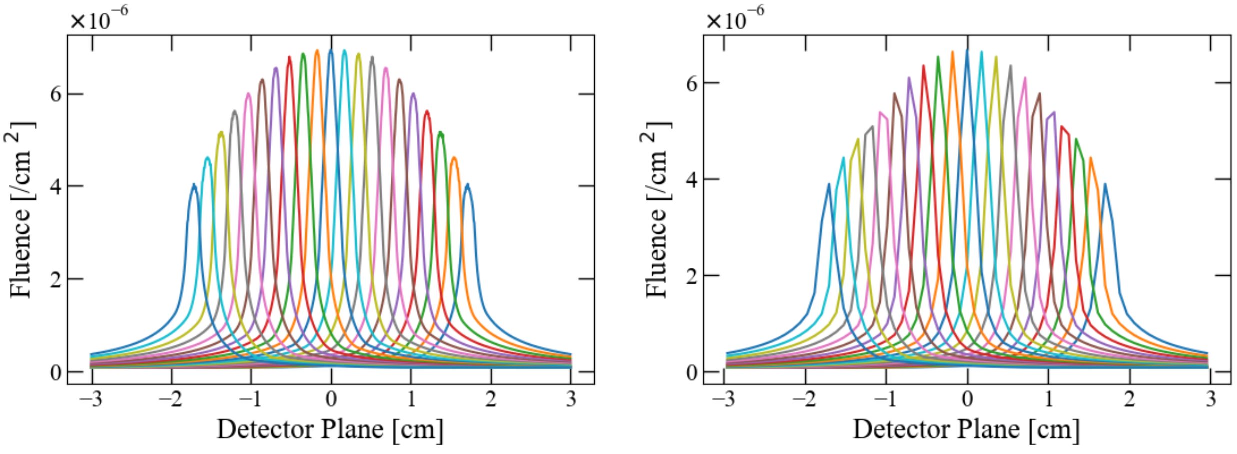

(a) (b)

Figure 2.3: Structure of 21 IRFs with 14 source points in each source bin. (a) High fidelity line spread function of every interaction point on the detector. (b) Averaged line spread function to chosen number of detector bins (67).

Determining the optimal IRF matrix size is challenging. First the data must be discriminated and binned to a certain resolution. This detector resolution is dependent on the number of tracks generated in the experiment. A high number of tracks will create a better signal-to-noise ratio (SNR). In the case of Poissonian statistics, this is calculated by $\sqrt{Tracks}/Tracks$. With a set number of tracks generated by the experiment, increasing the detector resolution (by decreasing bin width) will decrease the SNR.

An IRF matrix with a greater number of rows than columns is called an "overdetermined" system. Conversely, a greater number of columns is called an "underdetermined" system. The source resolution can be set to a resolution better than the previously calculated value of 500 µm, but is subject to the SNR of the data. A simple method to calculate the source bin size is to use the magnification of the experimental configuration. For a magnification of 3.6, simply use source bins that are a factor of 3.6 smaller than the detector bins. There is however some limit for this, as the detector resolution can be increased to some point that the source resolution becomes meaningless.

2.2 MCNP Comparison

Given the assumptions and simplifications, it is obvious that the analytical model will not be an exact representation of the system. Scattering in particular is not included in this model, which is an effect that would be perpetuated by all materials in the surrounding environment. Luckily CR-39 track eccentricity allows for discrimination against particle interactions that come from a non-incident angle. However, scattered neutrons can still occasionally reach the detector at the correct angle of interest. To compare how well the analytical model represents a model which includes scattering, MCNP [24,25] simulations were performed to generate the IRFs in Figure 2.2.

The MCNP simulation environment contains the tungsten rolled edge aperture and a single piece of CR-39. An F4 mesh tally was placed over the volume of the CR-39 detector and simulations were performed with neutrons emitted from point sources. Repeating the process generating Figure 2.2, point sources were placed every 0.05 cm in space along the z-axis from -0.5 to 0.5 cm in height. Individual mesh configurations were made for each simulation with 50 evenly spaced bins in the y-direction and 90 bins in the z-direction. To encapsulate the peaks of each response function, the binning in the z-axis placed 50 bins over a 1 cm to capture the peak, and 20 bins on either side of the peak to capture the tails. The mesh tally is then integrated across the y-direction to generate a 1-D profile. Figure 2.4 shows the 21 MCNP generated response functions.

When compared to the functions generated by the analytical model, the max absolute difference between corresponding peaks is less than 1.25%. This is likely due to the simplifications of the analytical model including not accounting for scattering, and distance variation of rays in the Y-direction. Source reconstructions performed with the MCNP IRF matrix created nearly identical solutions to the analytical model. This indicates that the analytical model is a reasonable approximation of response functions. Furthermore, for a 1 cm tall uniform source, Ref [8] estimates $\sim$650 tracks/cm^2 and this forward model approximates $\sim$635 tracks/cm^2. The ability to use the forward

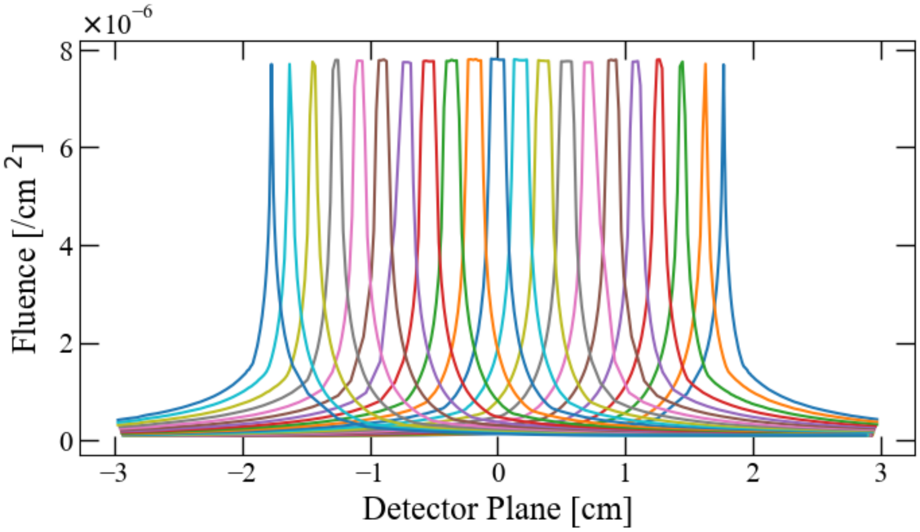

Figure 2.4: Scalar fluence for MCNP generated point spread functions from evenly spaced source points every 0.05 cm along a 1 cm tall source profile.

model over MCNP simulations greatly reduces the time needed to generate IRF matrices.

2.3 Synthetic Data Generation

The analytical forward model can be used to generate synthetic detector responses for various source profiles. Comparing a source reconstruction to the true model input can provide valuable information about the influence source types as well as which reconstruction method is optimal. When generating the synthetic datasets, various source profiles representative of MagLIF experiments are passed through the forward model, generating a nominal detector response. To simulate the experimental variation in data collection, samples are drawn from a Poisson distribution about the nominal response. This is repeated I times, with I being the number of bins on the detector, resulting in a 2-D image representing a piece of CR-39. As previously stated, the experimental data can be integrated across the non-resolving axis to produce a 1-D detector response. Figure 2.5 shows an example of synthetic data generation with (a) the Gaussian source input with 1×10^{13} neutrons emitted, (b) the nominal detector response, (c) the 2-D Poissonian sampled data, and (d) the axial 1-D synthetic data. The IRF matrix size used for synthetic examples is 31 source bins x 67 detector bins. This source resolution $\sim$322 µm, better than ODIN's resolution, but less than

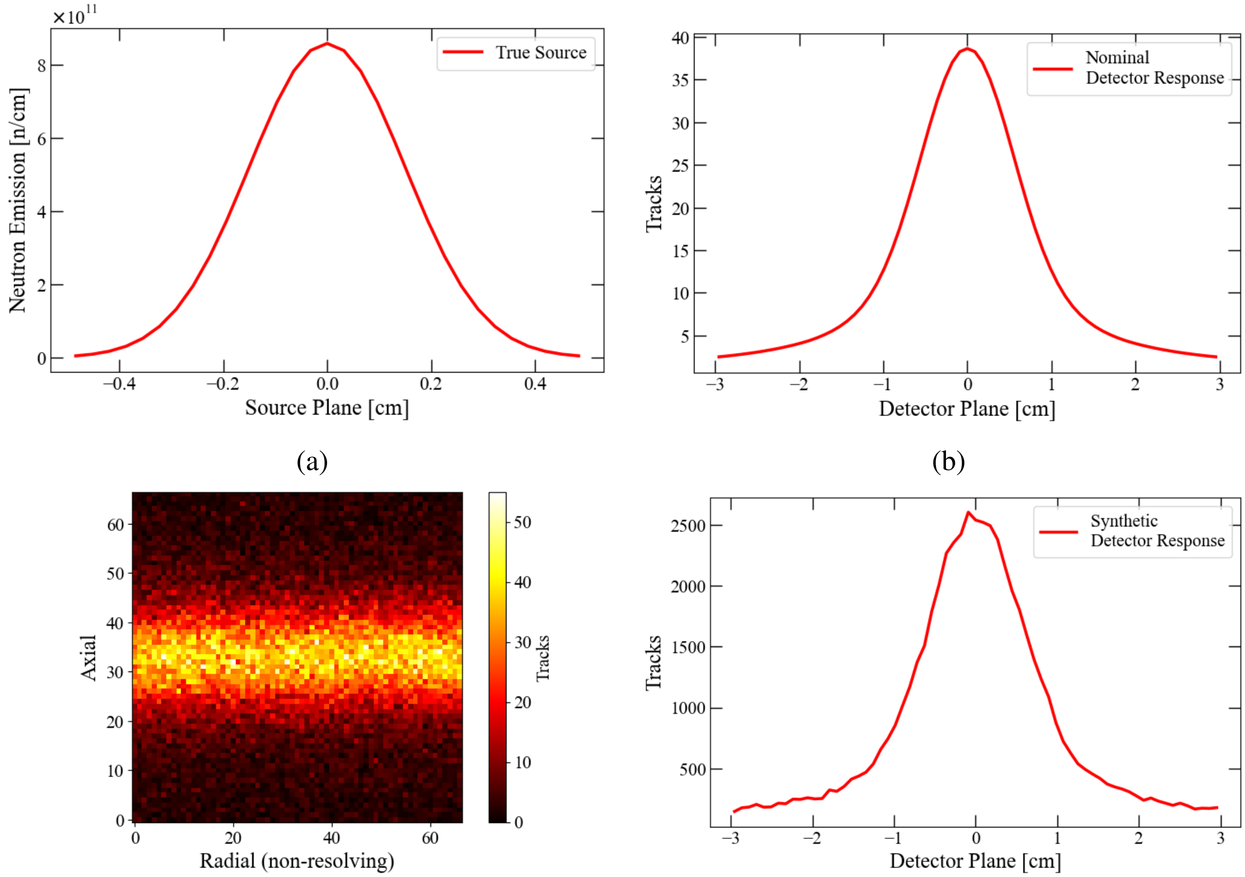

(a) (b)

(c) (d)

Figure 2.5: Analytical forward model synthetic data generation. (a) Gaussian source input with 1×10^{13} neutrons emitted. (b) Forward model output of nominal detector response. (c) Poissonian samples of nominal detector response to generate 2-D synthetic CR-39 response. (d) 2-D data integrated across the non-resolving axis to produce 1-D synthetic detector response profile.

the 3.6 magnification resolution of ∼249 µm. In future figures, synthetic sources and detector data will be shown as solid red lines.

3. IMAGE RECONSTRUCTION METHODS

Ideally, MagLIF experiments would produce a uniform stagnation column along the axial extent of the target, creating an axially uniform neutron emission seen by ODIN. Currently the MagLIF platform produces inconsistent stagnation column structures between each experiment. This can be due to numerous factors including intentional changes in experimental parameters such as magnetic field strength, laser energy, or current amplitude. However, there can also be perturbations caused by undesired effects such as instabilities, mix, or human error in experiment assembly. Any number of these factors can change the neutron emission profile and cause high frequency features, or "hot spots," where neutron production is increased. The amplitude and frequency of these hot spots vary, and it is crucial to not mistake areas of neutron production for noise in the reconstruction. Conversely, it is important to not mistake noise fluctuations in the reconstruction for hot spots.

The following sections will describe in detail different methods of image reconstruction with varying complexity. Synthetic data from three different source profiles were used as metrics to compare the viability of each method. Reconstructed sources will be able to be compared to the true synthetic source to quantify how each method performs. The first emission profile was a broad Gaussian, representing a low frequency emission profile over the axial extent, referred to as "low frequency". Next was two narrow Gaussian peaks of differing amplitudes with no signal in areas around the peaks, representing two individual hot spots, referred to as "high frequency". A combination of the two previous profiles was chosen as the third source, with a low frequency background and a single high frequency peak, referred to as "mixed frequency". Figure 3.1 shows all three of the synthetic source profiles, as well as the synthetic detector response generated by the analytical forward model previously described.

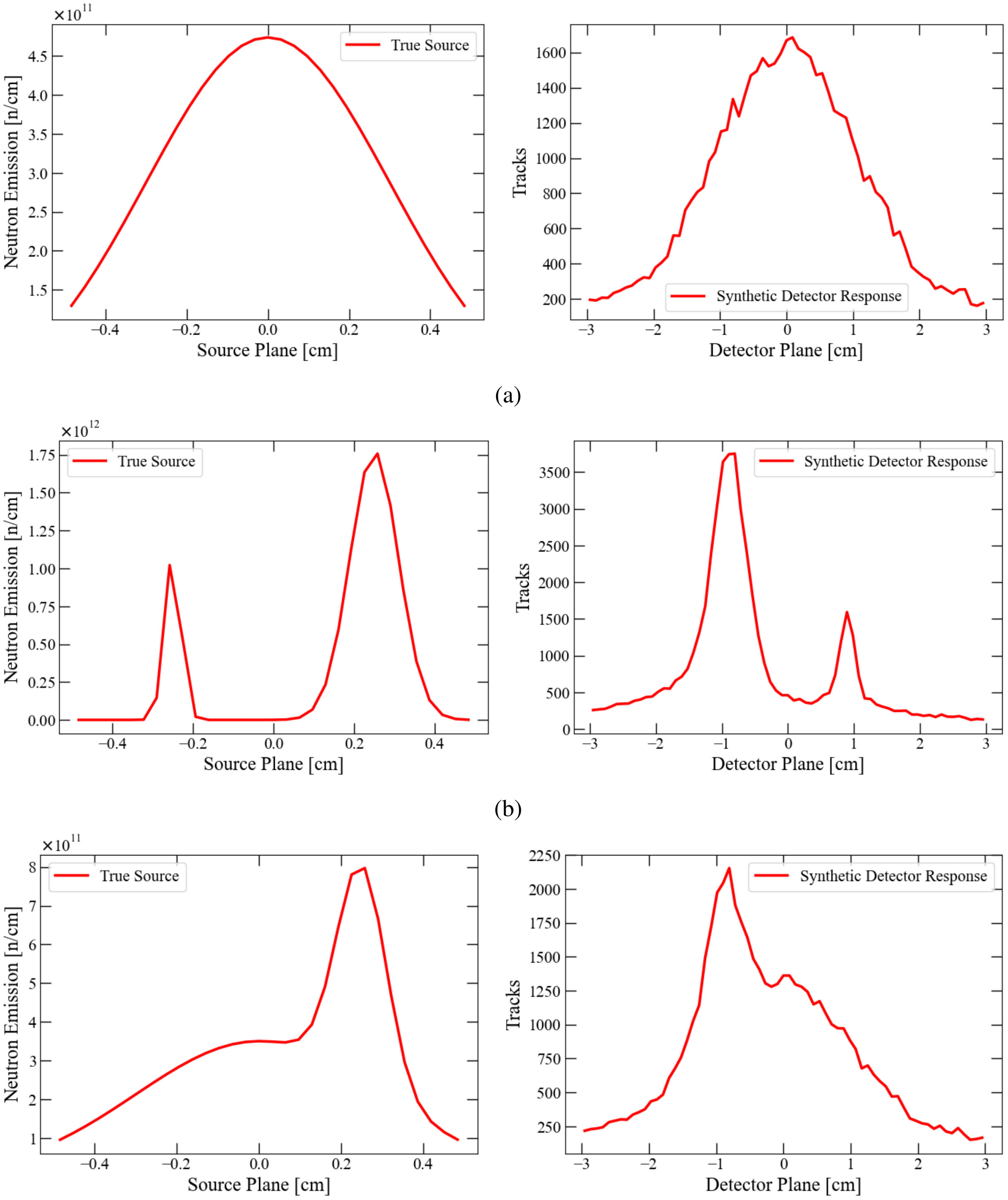

(a)

(b)

(c)

Figure 3.1: Synthetic source and detector response profile for (a) low frequency Gaussian across entire source extent ("low frequency"), (b) two high frequency Gaussians of varying amplitudes ("high frequency"), and (c) a combination of a high frequency Gaussian with a low frequency background ("mixed frequency").

3.1 Direct Matrix Inversion

As previously stated in Chapter 1, direct matrix inversion reconstruction methods involve using a system of linear equations to directly calculate a solution. These systems of equations are made up of the variables in Eq. 1.5 and can be subject to conditions when determining a solution.

3.1.1 Least Squares Fit

A least squares fit (LSF) is the most widely used direct matrix inversion method in which unknown parameters in a model are calculated to best fit the given data. The quantity S_i is defined as the expected value given model parameters G_j

$$S_i = \sum_{j=1}^{m} P_{ij} G_j. \tag{3.1}$$

The difference between given data and a model's expected value is known as the residual. The residual is be defined as

$$R_i = Y_i - S_i. \tag{3.2}$$

Here the unknown parameters in the model fit would be G_j , therefore the residual can be expressed as a function of the vector G. A LSF chooses the solution G which minimizes the sum of squares of the residual:

$$LSF : \min_{G} \sum_{i=1}^{n} R_i(G)^2 = \min_{G} \sum_{i=1}^{n} (Y_i - \sum_{j=1}^{m} P_{ij} G_j)^2. \tag{3.3}$$

Presented in Figures 3.2 to 3.4 are the LSF reconstructions and forward fit comparisons for each of the three synthetic sources. The forward fit is the reconstructed source forward propagated through the analytical IRF matrix. In (a) of each figure, the normalized LSF source reconstruction is compared to the true source, and the lower plot is the difference between the true and reconstructed source (or source residual). The (b) section of each figure compares the normalized forward fit from the reconstructed source to the normalized synthetic detector response. Below this is the residual between the normalized track profiles. Values in these figures are normalized to compare with iterative method results presented in the next section.

In Figure 3.2 (a) it can be seen that the reconstructed source is greatly over-fitting the low frequency source profile. However, Figure 3.2 (b) shows the residual to be rather small, indicating a good fit to the synthetic data. Figures 3.3 (a) and 3.4 (a) also show over-fitting in the source reconstructions, while synthetic data comparison in Figures 3.3 (b) and 3.4 (b) remain indicative of proper fitting. The cause of this is in the methodology of a LSF, which seeks to only minimize the residual. This can even lead to non-physical solutions, such as the reconstructed source in Figure 3.3 (a). In areas with no emission, such as -0.3 to -0.5 cm and 0.1 to -0.2 cm, the LSF solution provides elements with negative neutron emission. This is clearly a not physically possible in the experiment and reveals a fault in this methodology for certain emission profiles. To combat this flaw, more complex methods are needed.

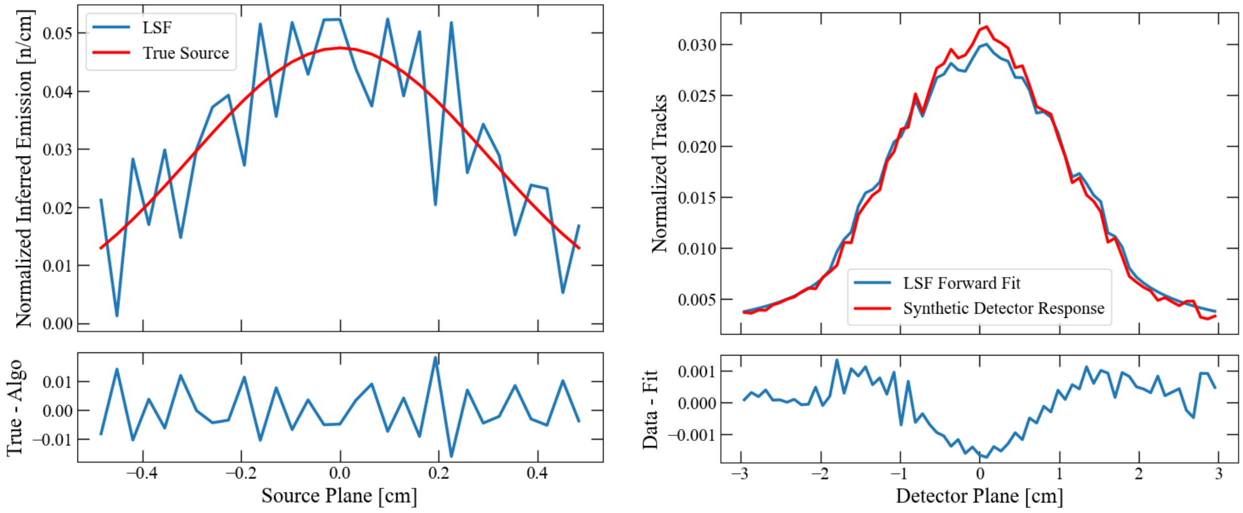

(a) (b)

Figure 3.2: LSF reconstruction of low frequency synthetic source. (a) Source comparison between true source and reconstructed source with corresponding source residual. (b) Synthetic detector response compared to LSF reconstruction forward fit and corresponding residual.

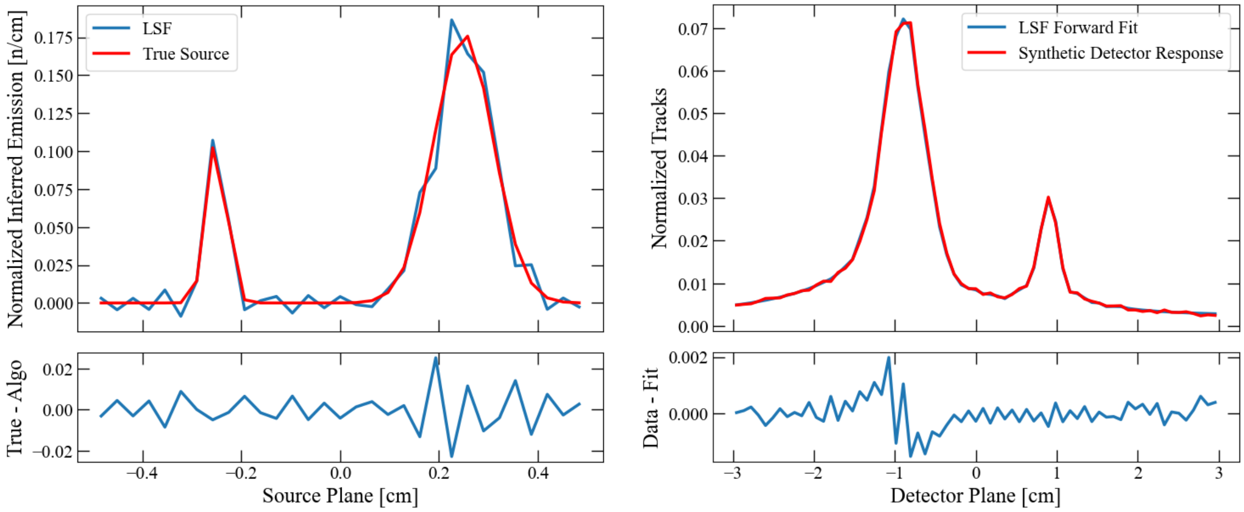

(a) (b)

Figure 3.3: LSF reconstruction of high frequency synthetic source. (a) Source comparison between true source and reconstructed source with corresponding source residual. (b) Synthetic detector response compared to LSF reconstruction forward fit and corresponding residual.

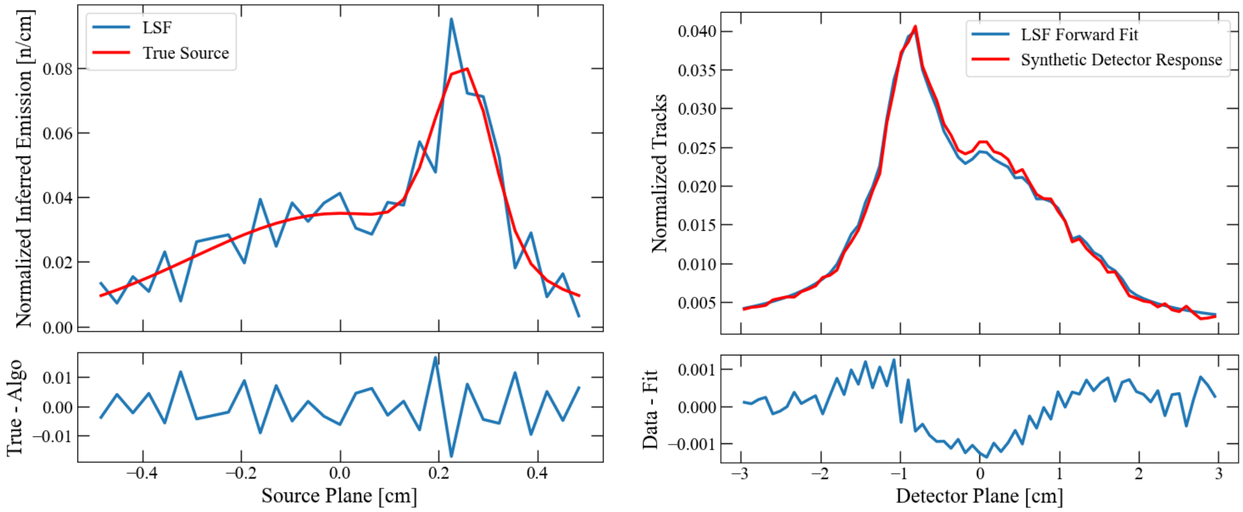

(a) (b)

Figure 3.4: LSF reconstruction of mixed frequency synthetic source. (a) Source comparison between true source and reconstructed source with corresponding source residual. (b) Synthetic detector response compared to LSF reconstruction forward fit and corresponding residual.

3.2 Iterative Methods

Iterative methods differ from direct matrix inversion methods by instead searching for a solution through iterative steps. It is common to normalize quantities in iterative algorithms such as the experimental data $y_i = Y_i/\sum_{i=1}^{n} Y_i$ as well as the columns, or spread functions of the IRF matrix $p_{ij} = P_{ij}/\sum_{i=1}^{n} P_{ij}$. The returned solution is a normalized vector expressed as a probability distribution $g_j = G_j/\sum_{j=1}^{m} G_j$.

These algorithms require an initial input guess for the source, and a stopping criteria to check for convergence of the solution. For this work the initial input for each iterative method was a normalized uniform source. A chi-squared goodness of fit test was used for a convergence metric defined as

$$\chi^2 = \sum_{i=1}^{n} \frac{(y_i - s_i)^2}{s_i}, \tag{3.4}$$

where $s_i = \sum_{j=1}^{m} p_{ij} g_j$. The absolute difference of chi-squared between iteration steps was used as the stopping criteria. For the examples below, a value of 10^{-3} was the chosen stopping criteria with a maximum number of iterations set to 10^3.

3.2.1 Non-Negative Least Squares Fit

A non-negative least squares fit (NNLSF) is a constrained form of a LSF [27,28].[1] This method still seeks to minimize the residual, but does not allow the fitting parameters in the model to be negative values. A NNLSF is represented as

$$NNLSF : \min_{G} \|Y - PG\|_2^2, \tag{3.5}$$

where all $G_j \geq 0$ and $\| \cdot \|_2$ is the Euclidean norm.

As this method will only differ when the reconstructed source contains negative elements, there is no difference between LSF and NNLSF in reconstructions for the low frequency (Figure 3.2) and

---

[1] The NNLSF algorithm from SciPy was used for this work. The algorithm uses an initial input of an array of zeros, and a stopping critera of 10^{-6} according to [28].

mixed frequency (Figure 3.4) synthetic sources. The high frequency source, which includes areas with no emission, was corrected by the NNLSF method as shown by the orange line in Figure 3.5. Features near the hot spots remain similar to the LSF reconstruction, and the areas with negative neutron emission have been eliminated. The forward fit remains to be well fit to the synthetic data, indicated by the small change in residual in Figure 3.5 (b).

While the high frequency source is well reconstructed with the NNLSF method, the low frequency and mixed frequency sources are still over-fitted. Therefore, further methods should be investigated in search of a method which will accurately reconstruct any source profile.

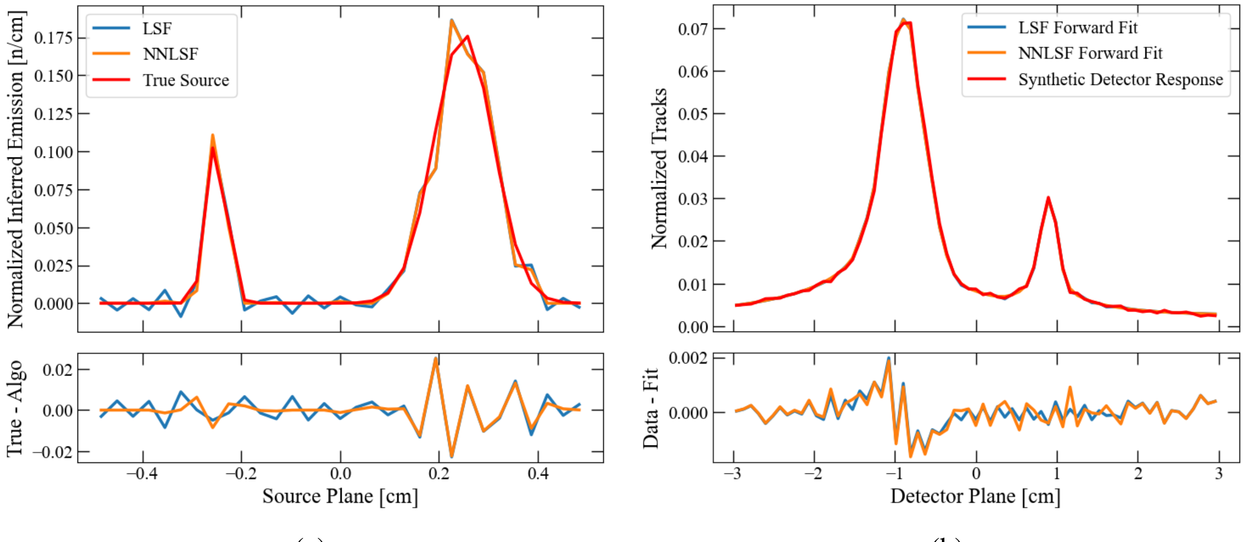

(a) (b)

Figure 3.5: NNLSF and LSF reconstruction of high frequency synthetic source. (a) Source comparison between true source and reconstructed sources with corresponding source residuals. (b) Synthetic detector responses compared to NNLSF and LSF reconstruction forward fits and corresponding residuals.

3.2.2 Maximum Likelihood Estimation

The most widely used iterative method is the expectation-maximization (EM) algorithm which converges to a solution that maximizes a likelihood function [29, 30, 31, 32]. This method successfully reconstructed 2-D images on ICF experiments at the NIF [9]. In the case of Eq. 1.3, the likelihood function can be written as a function of g_j

$$L(g) = p(y|g). \tag{3.6}$$

where $p(y|g)$ is the probability the measurement y was generated from a given source g. Usually the logarithm of the likelihood function is maximized for convenience:

$$g_{MLE} = arg \max_g \log L(g) = arg \max_g \log p(y|g), \tag{3.7}$$

where g_{MLE} is the solution, or maximum likelihood estimation (MLE).

The likelihood function in Eq. 3.7 differs between different noise distributions such as Poissonian or Gaussian, and result in altered EM algorithms [9, 33]. When assuming a Poissonian noise distribution, the likelihood function is defined as the joint probability the observed values y_i given by

$$L(g) = \prod_{i=1}^{n} \frac{g^{y_i} e^{-g}}{y_i!}. \tag{3.8}$$

While the log likelihood can be expressed as

$$\log L(g) = \sum_{i=1}^{n} [-g + y_i \log(g) - \log(y_i!)]. \tag{3.9}$$

This leads to the following iterative process referred to as MLE_Poiss:

$$g_j^{(t+1)} = g_j^{(t)} \sum_{i=1}^{m} p_{ij} \frac{y_i}{s_i^{(t)}}, \tag{3.10}$$

where $s_i^{(t)} = \sum_{j=1}^{m} p_{ij} g_j^{(t)}$ is the expected value of the model at the iteration step t This algorithm requires that all quantities be positive which ensures that the solution is also positive.

Given a Gaussian noise distribution the likelihood function can be written as

$$L = -\frac{1}{2} \sum_{i=1}^{n} \frac{(y_i - s_i)^2}{\sigma_i} + constant, \tag{3.11}$$

where σ_i are the variances of the corresponding ith experiment bin [33]. This leads to the following iterative process referred to as MLE_Gauss:

$$g_j^{(t+1)} = g_j^{(t)} \left(1 + h \sum_{i=1}^{m} p_{ij} \frac{y_i - s_i^{(t)}}{\sigma_i^2} \right), \tag{3.12}$$

where h is step size. The step size may be set to 1, or optimized at each iteration to speed up convergence [33]. The solution, g_j, must be normalized at each iteration step for both MLE_Poiss and MLE_Guass. Eq. 3.12 matches Eq. 3.10 when assuming a step size $h = 1$ and noise dispersion $\sigma_i = s_i$. If the noise dispersions, σ_i, belong to a normal distribution the maximum likelihood estimation matches a LSF. Both MLE_Guass and LSF do not require positive solutions and are susceptible to producing non-physical solutions.

Figures 3.6 to 3.8 show the MLE_Gauss (blue dotted) and MLE _Poiss (purple dashed) reconstructions for all three synthetic source profiles. The source reconstructions in (a) of each figure are less deviated from the true source than LSF or NNLSF reconstructions. However, the residuals in (b) of each figure have similar peak deviations from the detector response data, and are more oscillatory than previous LSF and NNLSF residuals. These features indicate the source is being more accurately reconstructed, in exchange for a less accurate forward fit. Each method is attempting to compensate for the underlying noise distribution in the synthetic data. Therefore the residuals should represent a noise distribution, making them more oscillatory in shape.

The high frequency source in Figure 3.7 (a) is once again the source with the best reconstruction, although the MLE_Gauss has some negative emission values similar to the LSF reconstruction in Figure 3.3 (a). Similarly to previous reconstructions, the low and mixed frequency sources are being over-fit by each MLE method. While there are improvements in reconstruction by the iterative methods, it is clear these MLE algorithms are susceptible to the noise from the dataset being amplified by the condition of the IRF matrix, resulting in noisy unacceptable solutions. Imposing regularization in these algorithms can reduce over-fitting and smooth the solutions. This can be performed in different ways including stopping the algorithm before the solution converges, or by adding a penalization term to the likelihood function to stabilize the solution.

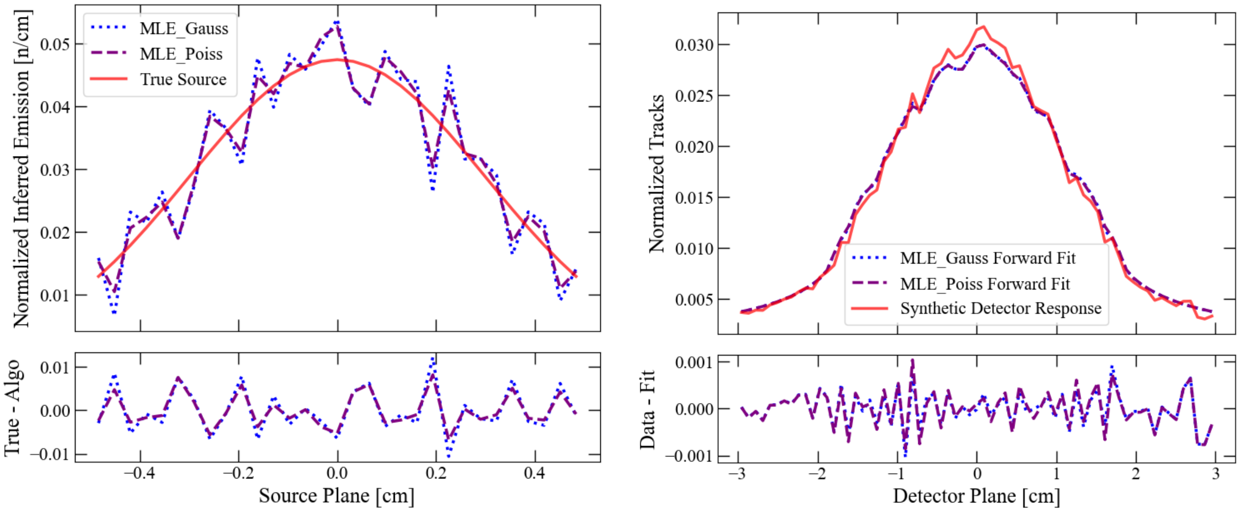

(a) (b)

Figure 3.6: MLE_Gauss and MLE_Poiss reconstructions of low frequency synthetic source. (a) Source comparison between true source and reconstructed sources with corresponding source residuals. (b) Synthetic detector response compared to MLE_Gauss and MLE_Poiss reconstruction forward fits and corresponding residuals.

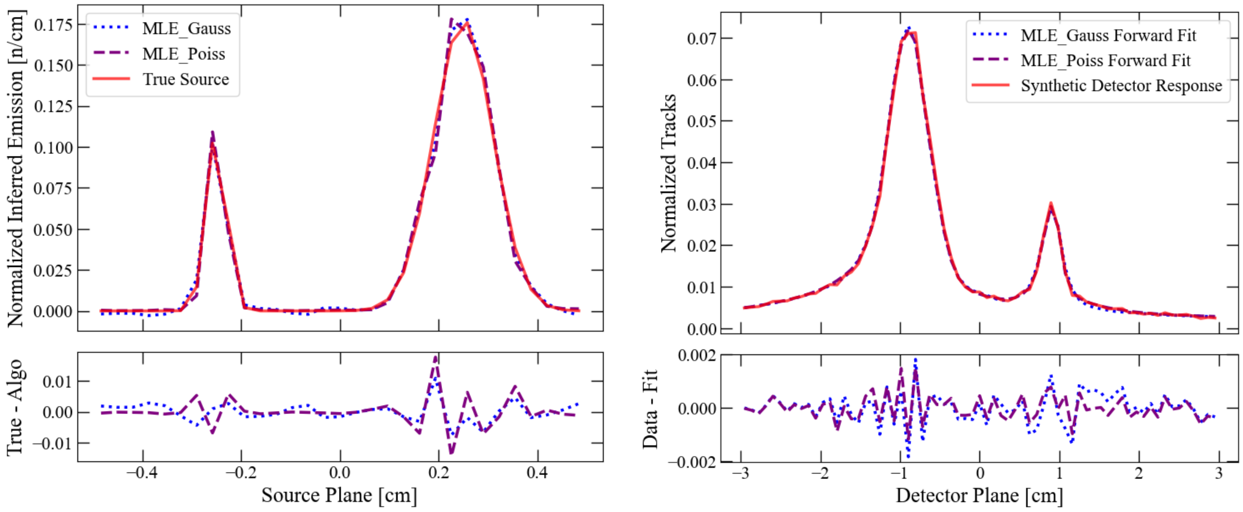

(a) (b)

Figure 3.7: MLE_Gauss and MLE_Poiss reconstructions of high frequency synthetic source. (a) Source comparison between true source and reconstructed sources with corresponding source residuals. (b) Synthetic detector response compared to MLE_Gauss and MLE_Poiss reconstruction forward fits and corresponding residuals.

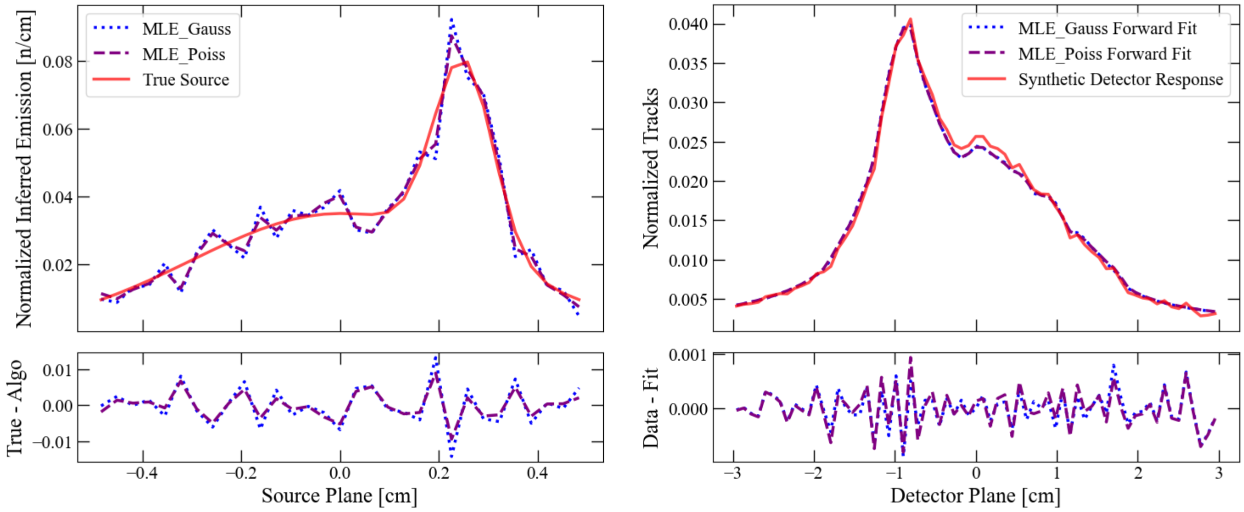

(a) (b)

Figure 3.8: MLE_Gauss and MLE_Poiss reconstructions of mixed frequency synthetic source. (a) Source comparison between true source and reconstructed sources with corresponding source residuals. (b) Synthetic detector response compared to MLE_Gauss and MLE_Poiss reconstruction forward fits and corresponding residuals.

3.2.3 Generalized Expectation-Maximization

The generalized expectation-maximization (GEM) [34] algorithm is an iterative method which follows closely to the MLE_Poiss algorithm. This algorithm is based on maximum a posteriori (MAP) estimation which requires a an added penalization term for regularization to Eq. 3.7

$$g_{MAP} = arg\max_{g} \log p(y|g) + \log p(g). \tag{3.13}$$

If $p(g)$ (known as the "prior") is chosen as uniform over the acceptable parameter space, then $p(g)$ is a constant and the solution matches Eq. 3.7. A Gibbs prior potential function can be added as the prior in the likelihood function

$$g_{GEM} = arg\max_{g} \log p(y|g) - \frac{1}{\beta}\sum_{c\in C} V_c(g), \tag{3.14}$$

where $V_c(g)$ is a Gibbs prior potential function with C number of neighbors, and β is a regularization parameter. Gibbs prior potential functions between solution element neighbors are calculated and used as a form of regularization to add smoothing to the solution where large discontinuities could be present. The number of neighbors can be determined by the dimensions of the problem, where higher dimensions have more neighboring elements.

The iterative procedure is composed of two repeated steps, expectation and maximization. With the added prior, the maximization step must be solved iteratively. Therefore, there is an iteration within each iteration step of the GEM algorithm. For Poissonian data and using Gibbs priors, the following two variables are needed for the expectation step:

$$a_j = \sum_i P_{ij}, \tag{3.15}$$

and

$$b_j^{(t)} = \sum_i \frac{y_i P_{ij} g_j^{(t)}}{\sum_q P_{iq} g_q^{(t)}}. \tag{3.16}$$

The potential function used in this work was $V(g_\ell; g_j) = (g_\ell - g_j)^2$ where g_j is the current element being visited and g_ℓ is a neighboring pixel. Choosing an initial source with all elements $g_j > 0$ ensures that the solution is non-negative due to the gradient ascent approach used. The algorithm presented here outlines the GEM procedure for Poissonian data using Gibbs priors and can be found in [34].

Step 1

For all solution elements, compute $g_j^{EM} = b_j^{(t)}/a_j$. If P_{ij} has already been normalized, then $a_j = 1$ for all j.

Step 2

Visit each solution element sequentially and complete steps 2a-2d for each element.

Step 2a

Compute C_1 and C_2:

$C_1 = a_j(-g_j^{(t)} + g_j^{EM} \log g_j^{(t)}) - \sum_c \frac{V(g_\ell; g_j^{(t)})}{\beta}$

$$C_2 = \frac{1}{\beta} \sum_c \frac{\partial}{\partial g_j^{(t)}} V(g_\ell; g_j^{(t)})$$

Step 2b

Set $\alpha = 1$.

Compute $g_j^{(t+1)} = g_j^{EM} - \dfrac{C_2 g_j^{(t)}}{a_j}$

If $g_j^{(t+1)} > 0$ go to 2d

if $g_j^{(t+1)} \leq 0$ compute $\alpha = \dfrac{0.5}{1 - \dfrac{g_j^{EM}}{g_j^{(t)}} + \dfrac{C_2}{a_j}}$

Step 2c

$$\text{Compute } g_j^{(t+1)} = (1-\alpha) g_j^{(t)} + \alpha \left\{ g_j^{EM} - \frac{C_2 g_j^{(t)}}{a_j} \right\}$$

Step 2d

$$\text{Check if } a_j(-g_j^{(t+1)} + g_j^{EM} \log g_j^{(t+1)}) - \sum_c \frac{V(g_\ell; g_j^{(t+1)})}{\beta} \geq C_1.$$

If yes, update the current element to $g_j^{(t+1)}$ and proceed to the next element. If no, divide α by 2 and return to Step 2c.

It can be seen that the regularization parameter, β, appears in the denominator of the added prior. Therefore, as β approaches $+\infty$ the regularization contribution approaches zero and the algorithm converges to a MLE_Poiss reconstruction. The impact of regularization terms are increased the smaller β becomes, and the solution becomes increasingly smoothed.

Figure 3.9 shows and example of source reconstruction of the low frequency synthetic source with varying magnitudes of β. High β values in Figure 3.9 (a) are nearly identical, and closely match the MLE_Poiss reconstruction. The reconstruction begins to smooth in Figure 3.9 (b), as higher frequencies in the reconstruction are eliminated. Finally, the solution begins to overcompensate the smoothing in Figure 3.9 (c) and flatten the signal too much. Given these reconstructions the optimal regularization parameter for this source profile lies somewhere near the range $\beta = 1$ to 0.1.

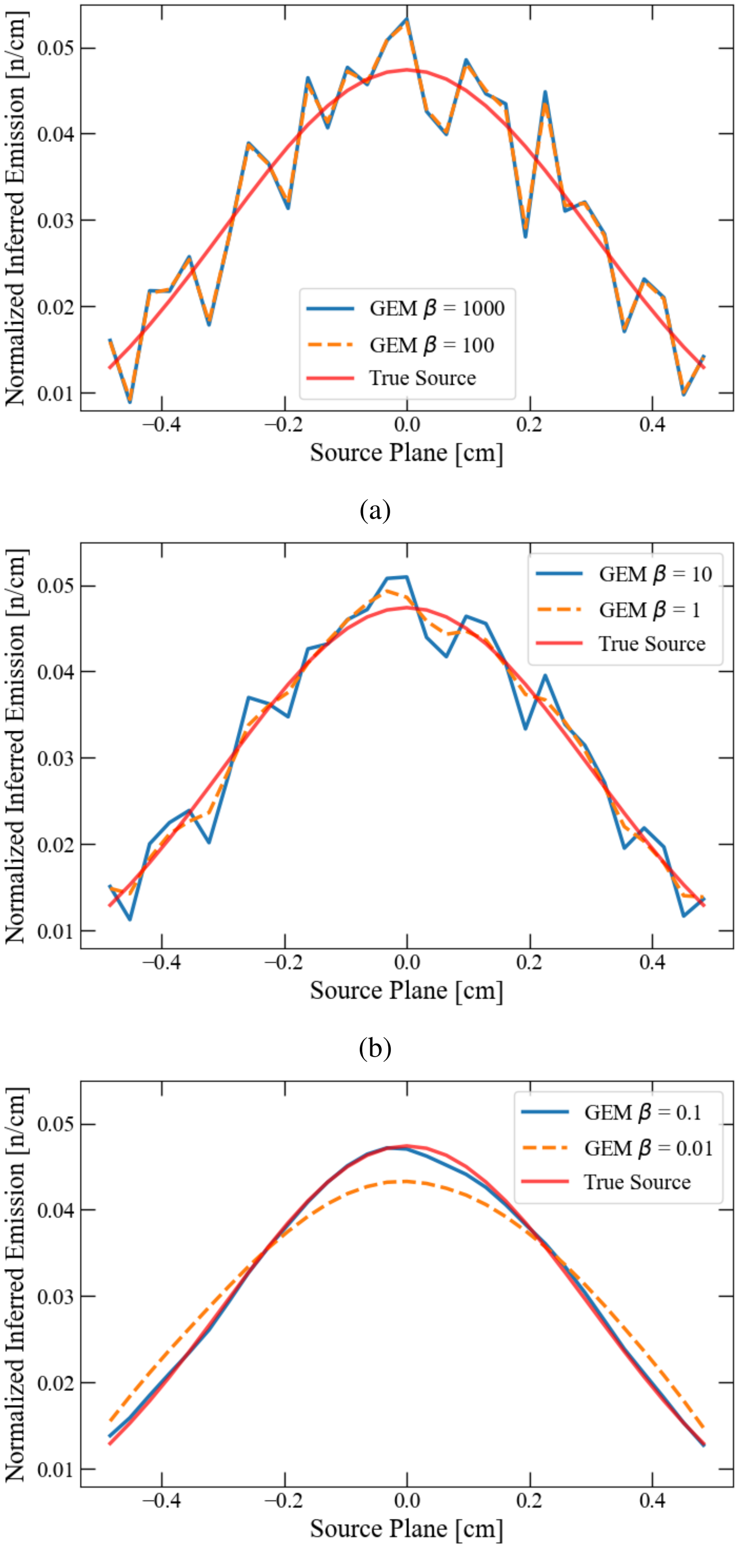

(a)

(b)

(c)

Figure 3.9: GEM reconstructions compared to low frequency synthetic source with varying regularization parameters: (a) $\beta = 1000$ and 100, (b) $\beta = 10$ and 1, (c) $\beta = 0.1$ and 0.01.

The process for choosing the optimal regularization parameter is challenging for ill-posed problems. To balance smoothing and over-fitting solutions, the L-curve method is a common approach to determining a regularization parameter [35, 36]. Figure 3.10 provides and example of an L-curve with the residual norm on the x-axis and solution norm on the y-axis. As regularization is increased, more smoothing is implemented, and the residual norm grows. With less regularization, the solution becomes over-fitted, and the solution norm grows. The optimal regularization parameter lies at the corner of the L-curve.

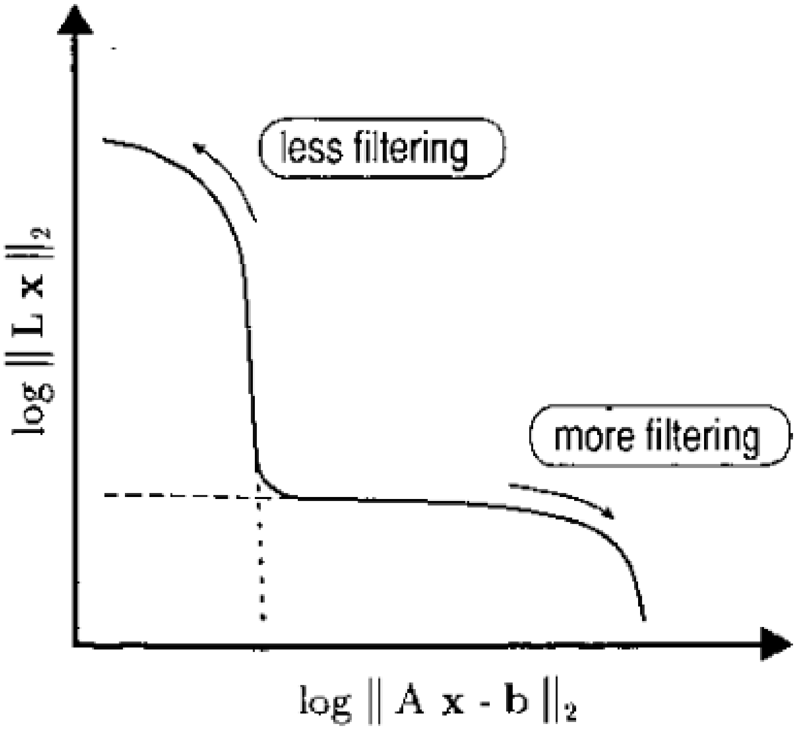

Figure 3.10: Example plot of an L-curve on a log-log scale. Reprinted from [35], with the permission of IOP publishing.

However, due to the non-negativity constraint on GEM solutions, the L-curve approach cannot be used. The non-negativity constraint does not allow for over-fitting beyond a certain extent, so the solution norm reaches an equilibrium above a certain β value. This causes the L-curve to stop at the intersection of the two legs, and not complete the upper portion of the "L."

In order to consistently select an appropriate value of β, an alternative method must be used. One such method is a k-fold cross validation, often used in statistical machine learning to perform such hyperparameter selections [37]. This method tests the performance of a solution generated from a subset of the data, with the remaining held-out data not used during the reconstruction. The generated solution by a given β can be forward modeled and quantified how well it fits the held-out data using a metric such as chi-squared.

To implement this process, indices of the entire dataset are randomized, then split evenly into k sections. $k-1$ sections are chosen as the training data points which are used to generate a GEM source reconstruction. The generated source is then passed through the forward model and a chi-squared goodness of fit test is calculated with the remaining section of data points, the validation data. The chi-squared is calculated k number of times, each time using a different section as the validation data. By completing this process over a range of β values, k curves of goodness of fit are be generated as a function of β for both the training and validation datasets. The optimal β value is determined by taking the mean of the validation curves, and choosing the value with the best fit. In the case of chi-squared, the β with the lowest chi-squared value is selected as the optimal regularization parameter.

Figures 3.11 to 3.13 show GEM (solid black) reconstructions for all three synthetic source profiles. In (a) of each figure is the chi-squared vs β plot resulting from a k-fold cross validation in log-log scale with β values ranged from 10^{-4} to 10^{3}. The max β was set to 10^{3} because near this value the influence of regularization begins to become negligible and higher β values do not significantly change the solution. This is supported by Figure 3.9 (a) and in (a) of each subsequent Figure as the chi-squared begins to stabilize in value with higher β values. The chi-squared vs β plots include the training (solid blue), validation (solid orange), and validation mean (dotted blue) curves. A dashed black vertical line indicates the β value with the lowest chi-squared value in the validation mean curve, which is selected as the optimal regularization parameter.

In (b) of each figure is the GEM source reconstruction using the determined optimal β value compared with the MLE source reconstructions and the true source. Below this is the corresponding source residuals for each source reconstruction. The optimized GEM method performed reconstruction better the MLE methods as shown by the smaller source residual in all three source profiles. Optimal β values scaled with the frequency of the source features as expected, with decreased β values smoothing the solution.

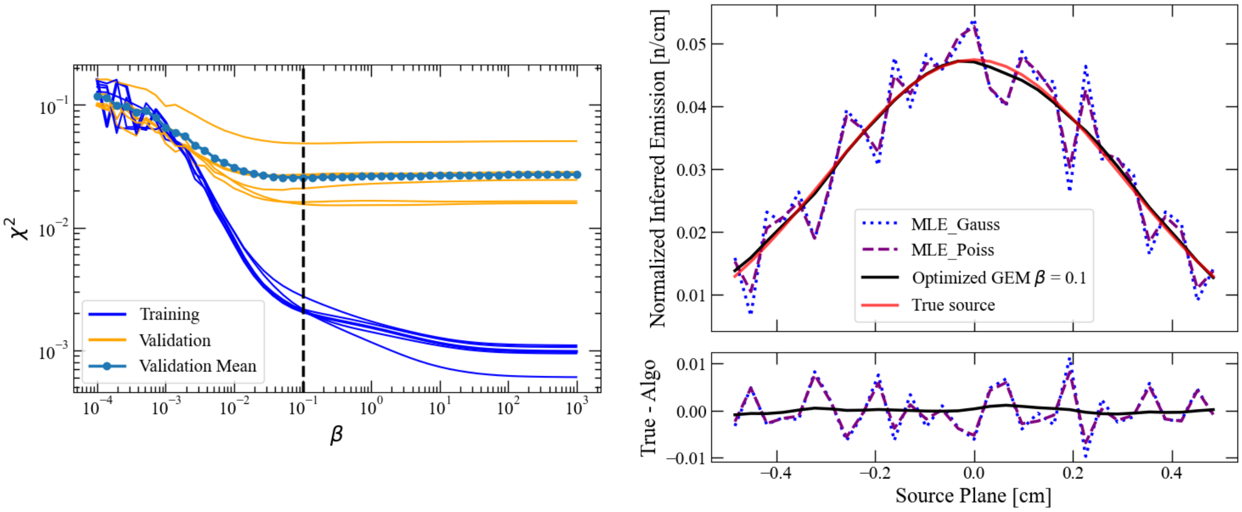

(a) (b)

Figure 3.11: Low frequency source GEM reconstruction. (a) k-fold cross validation results to determine chi-squared training, validation, and validation mean curves as a function of β. The dashed black vertical line indicates the β corresponding to the lowest validation mean chi-squared. (b) Source reconstruction and residual for MLE_Gauss, MLE_Poiss, and GEM using the optimal regularization parameter ($\beta = 0.1$).

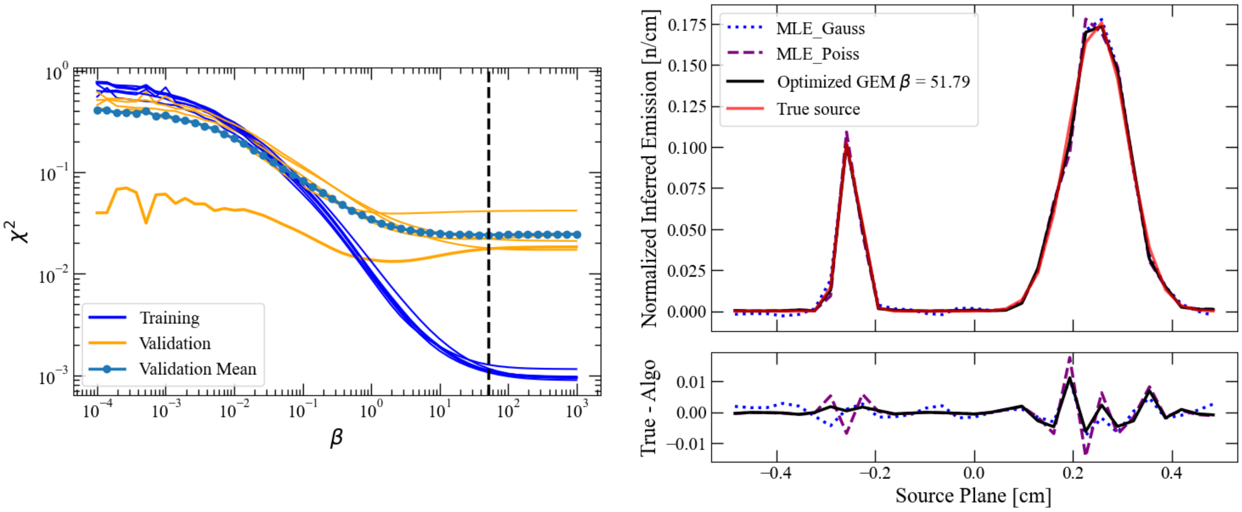

(a) (b)

Figure 3.12: High frequency source GEM reconstruction. (a) k-fold cross validation results to determine chi-squared training, validation, and validation mean curves as a function of β. The dashed black vertical line indicates the β corresponding to the lowest validation mean chi-squared. (b) Source reconstruction and residual for MLE_Gauss, MLE_Poiss, and GEM using the optimal regularization parameter ($\beta = 51.79$).

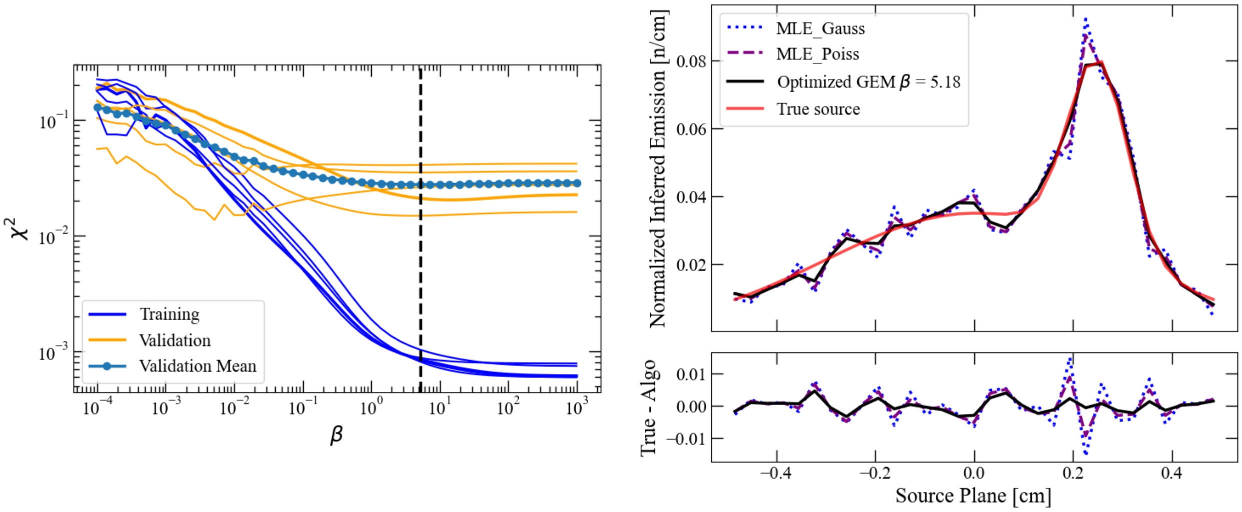

(a) (b)

Figure 3.13: Mixed frequency source GEM reconstruction. (a) k-fold cross validation results to determine chi-squared training, validation, and validation mean curves as a function of β. The dashed black vertical line indicates the β corresponding to the lowest validation mean chi-squared. (b) Source reconstruction and residual for MLE_Gauss, MLE_Poiss, and GEM using the optimal regularization parameter ($\beta = 5.18$).

One caveat of the k-fold cross validation is the uncertainty in the β parameter. This method is subject to the discretization of β values, as well as the randomness of the indices. Repeating the k-fold cross validation can produce different optimal β values, resulting in a range of possible solutions. The uncertainty in β is not accounted for in this work, however, a possible method to be investigated in the future is described in Chapter 6.

4. ODIN FORWARD MODEL SENSITIVITY ANALYSIS

During the experimental set up of ODIN there are multiple components which need to be accurately aligned to ensure proper data collection. However, as with any experiment, there is a range of uncertainty in each parameter. This includes configuration measurements used during the experimental set up and alignment of the diagnostic. A sensitivity analysis of the ODIN analytical forward model has been performed to study impact of variations in model parameters. This develops and understanding of what parameters create the largest variations in experimental data, which in turn highlights parameters needed to be precise during the experimental set up. These parameter uncertainties can propagate and create variations in experimental data. Quantifying this uncertainty propagation is challenging, and a synthetic method has been performed to understand the possible reconstruction thresholds of three different source profiles. This can be difficult to perform on experimental data, as well as computationally expensive. An alternative approach is presented, which can be applied to estimate solution uncertainty on experimental datasets.

4.1 Sensitivity Study

ODIN's analytical forward model has four variable parameters which can be easily adjusted. Figure 4.1 shows a 2-D model of ODIN and the main parameters with variability during experimental set up. The variable parameters are as follows:

- D_slit: Distance of the aperture apex from the source plane
- H_slit: Aperture opening distance between tungsten apexes
- Z_offset: Z-axis distance offset of aperture
- Theta: Angle of rotation of aperture housing (based about aperture center)

Each of these values were selected by investigating the experimental setup procedure, including an estimated range of variation for each. Multiple samples were drawn from this parameter range, each creating a unique IRF matrix. These IRF matrices were then forward modeled using a known source. The resulting detector response represent experiments performed with some perturbation

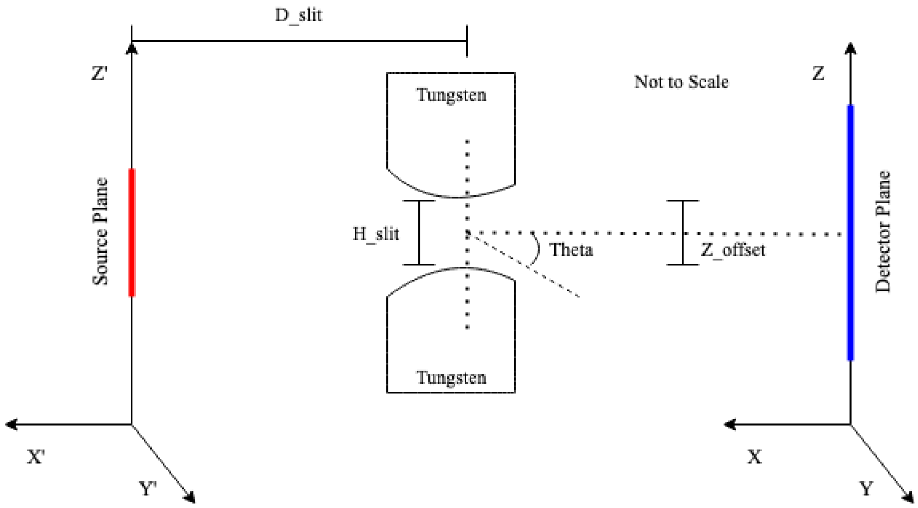

Figure 4.1: 2-D model of variable ODIN parameters (not to scale) including D_slit, H_slit, Z_offset, and Theta.

to the system. Each response was then used for source reconstruction using the nominal IRF matrix. A range of error was then generated for each source type by taking the mean and standard deviation of all reconstructed sources. By comparing the known source profile to the perturbed reconstructed sources, the sensitivity of each parameter was evaluated.

4.1.1 Noise Variation

Poissonian noise is always present in the data acquisition process of CR-39, therefore, it was used when generating synthetic detector responses. The generation of synthetic detector responses (shown in Chapter 2) uses random Poissonian sampling of the nominal detector response. Variations in this sampling itself vary the reconstructed source profile. In experimental data, this variance would be seen in CR-39 data between scans of multiple faces/pieces in the same detector package as described in Section 1.3.2.

To evaluate the sensitivity of noise variation, ten different synthetic detector responses were generated with random Poissonian permutations. Figures 4.2 to 4.4 show the mean reconstructions and standard deviations for a low frequency, high frequency, and mixed frequency source from the ten generated detector responses. Subplots of each figure show (a) the varied detector responses,

(b) LSF and NNLSF reconstructions, (c) MLE_Gauss and MLE_Poiss reconstructions, and (d) GEM reconstructions using an optimized β value for each. It is common for LSF and NNLSF reconstructions to overlap and occasionally match exactly. The true source can be seen as red dotted points in (b) through (d) for comparison. This figure structure is used throughout the rest of this chapter.

It is clear from these figures that there is significant variation when sources contain broad Gaussian signals. However, this is a property of Poissonian statistics, where an increased number of counts increases the SNR. These source profiles have all been propagated with a total yield of 1×10^{13} neutrons, which is comparable to current MagLIF yields. The variation of reconstructions is inversely proportional to the SNR which increases with higher neutron yields.

The GEM reconstructions in each of these sources has a significantly lower standard deviation compared to other methods. Even with one standard deviation the GEM method also under-predicts the peak amplitude of the true source, which is a common issue in reconstruction methods using regularization [36]. In addition, each realization has a single β, and there is no attempt to account for the uncertainty in each realization as stated in Chapter 3.

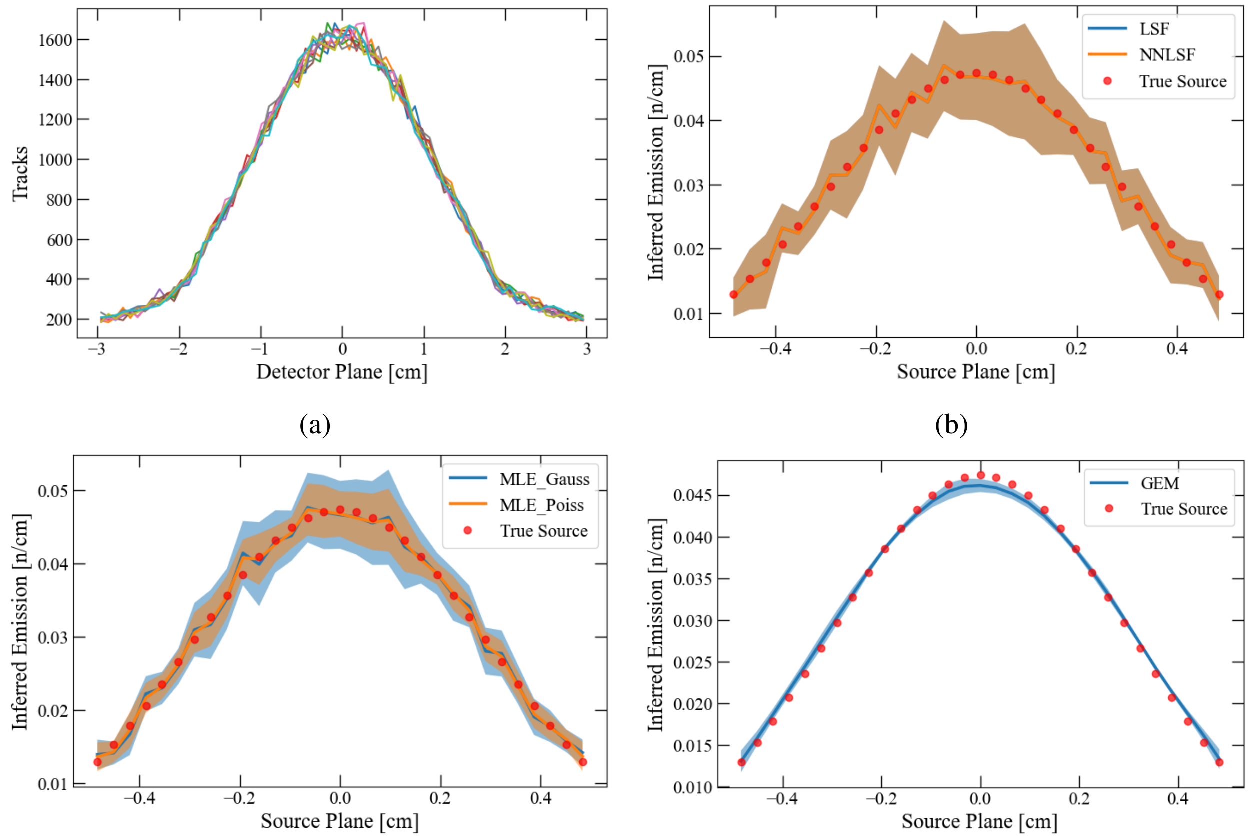

(a) (b)

(c) (d)

Figure 4.2: Low frequency synthetic source reconstruction with ten noise variation samples. (a) Ten Poissonian samples of nominal detector response. (b) LSF and NNLSF reconstructions mean (solid lines) with one standard deviation envelope (opaque region). (c) MLE_Gauss and MLE_Poiss reconstructions mean (solid lines) with one standard deviation envelope (opaque region). (d) GEM reconstructions mean (solid line) with one standard deviation envelope (opaque region).

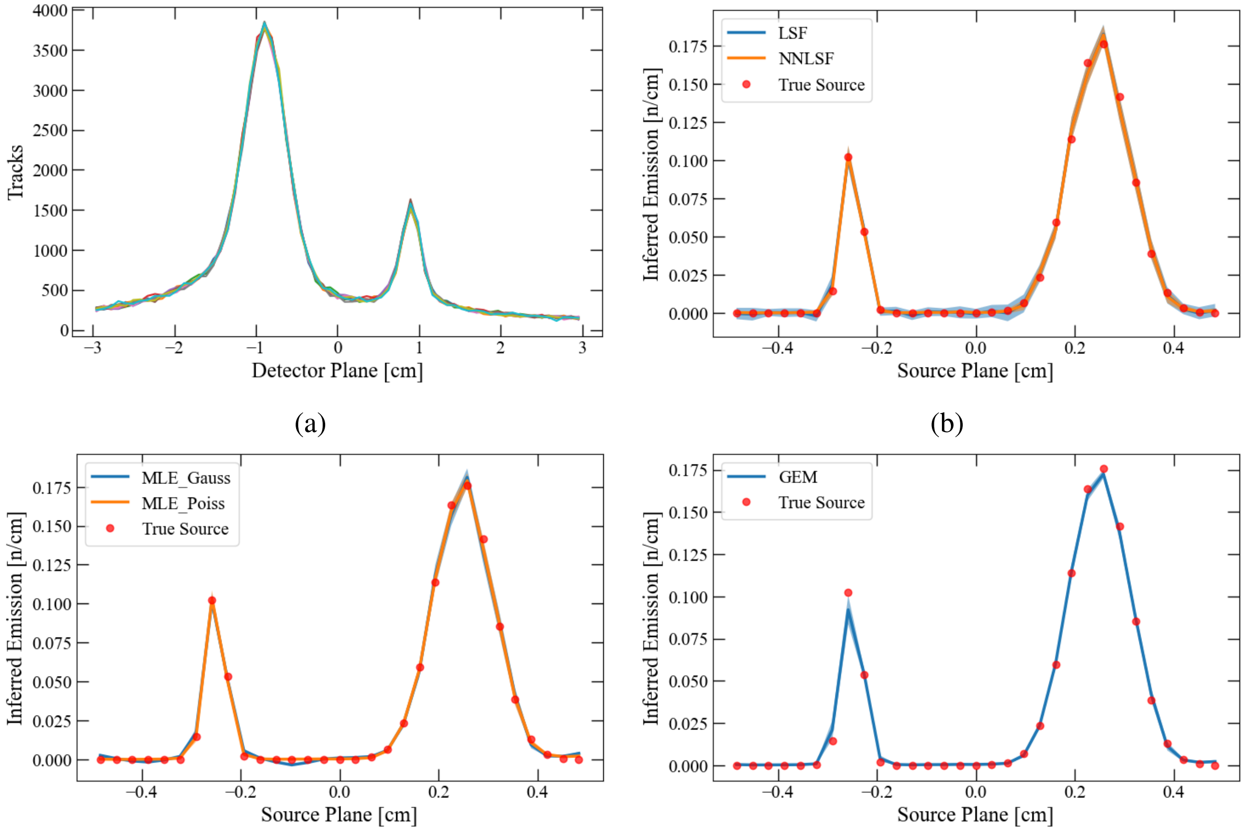

(a)

(b)

(c)

(d)

Figure 4.3: High frequency synthetic source reconstruction with ten noise variation samples. (a) Ten Poissonian samples of nominal detector response. (b) LSF and NNLSF reconstructions mean (solid lines) with one standard deviation envelope (opaque region). (c) MLE_Gauss and MLE_Poiss reconstructions mean (solid lines) with one standard deviation envelope (opaque region). (d) GEM reconstructions mean (solid line) with one standard deviation envelope (opaque region).

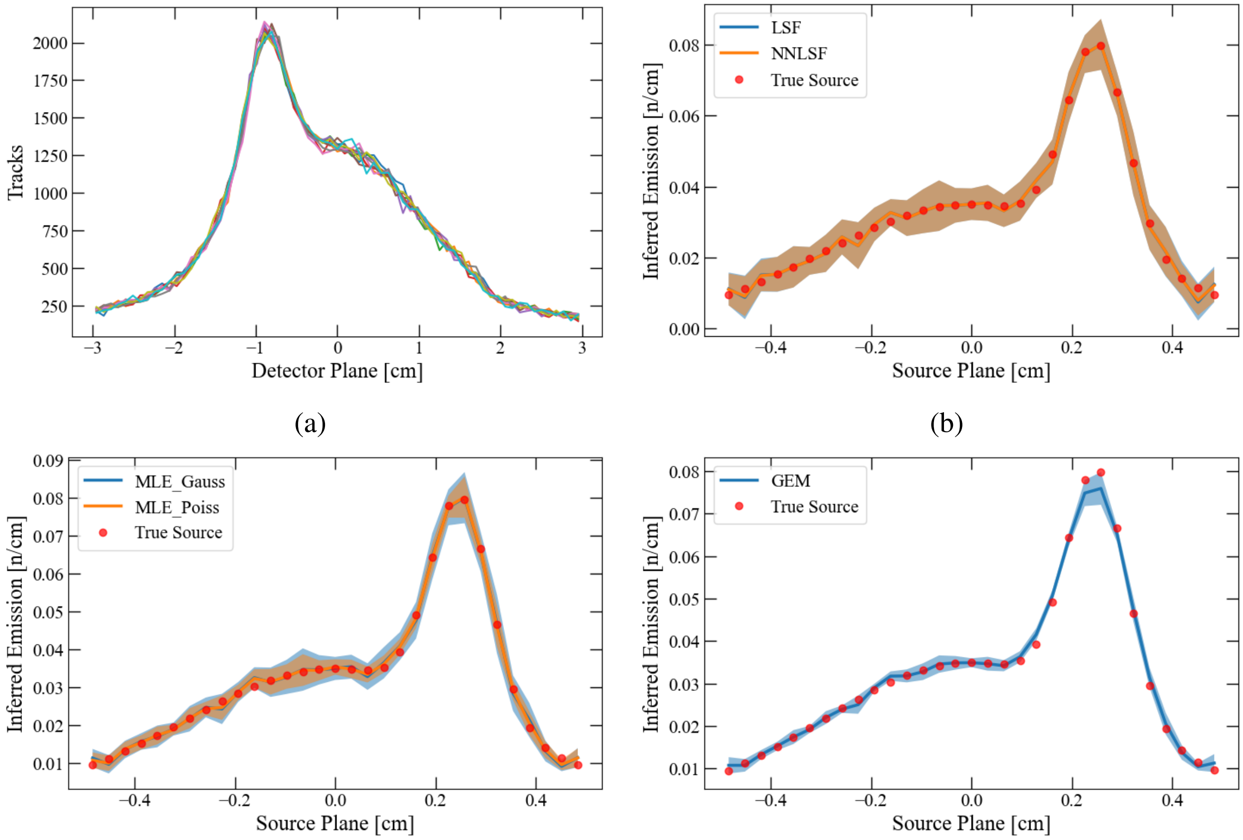

(a) (b) (c) (d)

Figure 4.4: Mixed frequency synthetic source reconstruction with ten noise variation samples. (a) Ten Poissonian samples of nominal detector response. (b) LSF and NNLSF reconstructions mean (solid lines) with one standard deviation envelope (opaque region). (c) MLE_Gauss and MLE_Poiss reconstructions mean (solid lines) with one standard deviation envelope (opaque region). (d) GEM reconstructions mean (solid line) with one standard deviation envelope (opaque region).

4.1.2 D_slit Variation

The D_slit parameter is defined by the distance from the source plane to the aperture's apex of curvature. Changing this parameter alters the magnification of the system defined by

$$M = \frac{L_2}{L_1} \tag{4.1}$$

where L_1 is the distance from source plane to aperture apex, and L_2 is the distance from aperture apex to detector plane. As previously stated in Chapter 2, the apex is placed at either 18 cm or 22 cm from the source depending on the orientation. The 22 cm orientation has the larger opening of the aperture facing the source, and has a magnification of 3.6.

Four perturbed D_slit values were used to generate the perturbed IRF matrices. The values used were 21.365, 21.6825, 22.3175, and 22.635 cm, which corresponds to increments of 1/8" in either direction from the nominal value. When taking measurements in-chamber, few parameters are measured when aligning diagnostics due to changing locations, line of sight interference, or issues with the platform on which diagnostics are mounted. A prescribed measurement is chosen in the pre-shot planning process, and then measured with a tape measure in Imperial units. Every experimental set up differs, and measurements have been taking which were $\sim$1/8" from the prescribed value. The chosen values for the sensitivity analysis are meant to be conservative, which is why they extend to 1/4" in either direction.

To understand the changes caused by alterations of D_slit, or any of the other parameters, the nominal IRF matrix can be compared to the perturbed IRF matrix. Changes to the response functions can provide insight into the sensitivity of each parameter. Figure 4.5 shows five of the 21 nominal IRFs from Figure 2.2 (blue solid) and the same five IRFs generated in the perturbed D_slit model (red solid). While these were not the IRFs used in this model, the simplified point spread functions visually emphasize the changes occurring from a perturbation. When shifting D_slit to 21.365 cm there is an increase in magnification, exemplified by the outermost IRFs shifting outward in Figure 4.5 (a). The opposite is seen in Figure 4.5 (b), where D_slit being increased to 22.635 cm shifts the outermost IRFs inward. Figures 4.6 to 4.8 show the mean reconstructions and standard deviations for a low frequency, high frequency, and mixed frequency source from the four D_slit perturbed detector responses.

The magnification change did not significantly affect the source reconstructions apart from the increased edge variation for broad Gaussian sources. This is caused by the outermost response functions having a different area of influence due to the magnification change. In the Nominal IRF matrix, the outermost response function is incapable of producing increased or decreased signals in this area. These edge spikes are the reconstruction methods amplifying or decreasing the emission in the outermost response function to compensate for the signal.

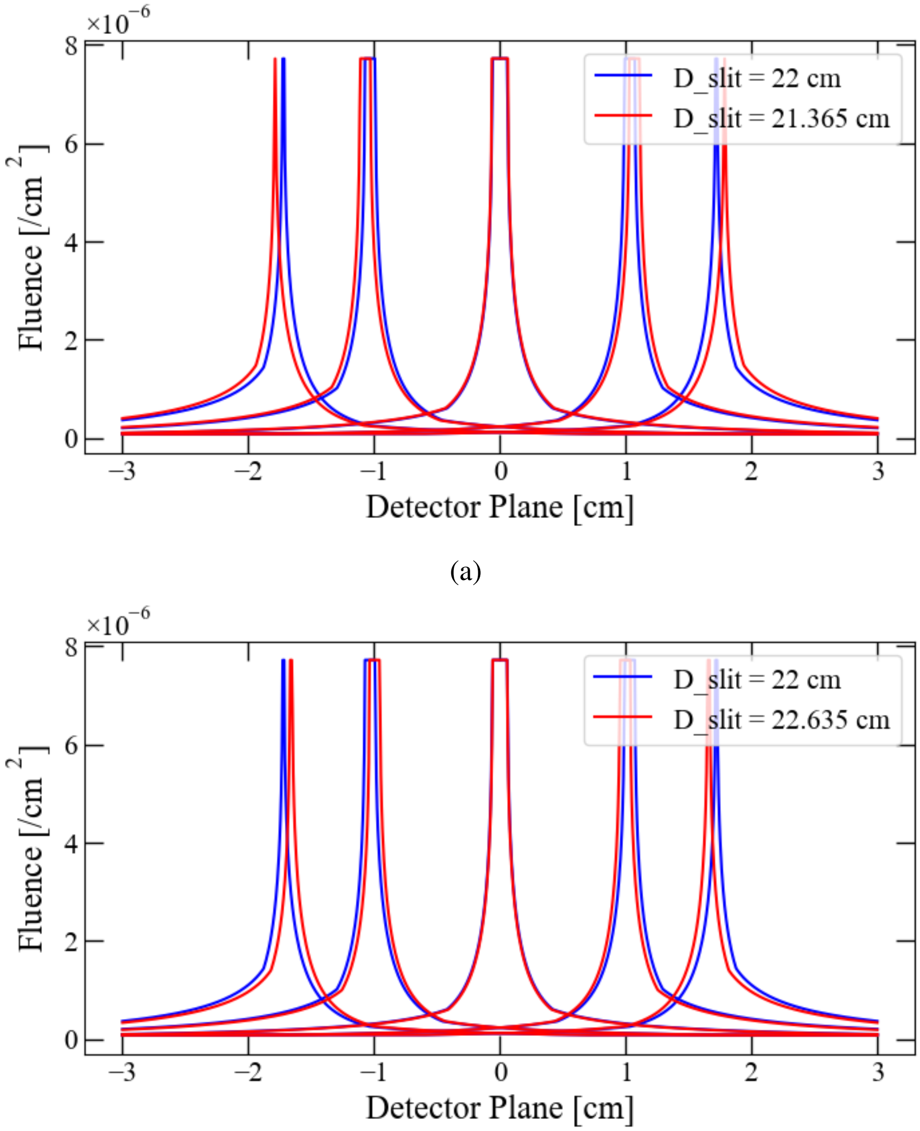

(a)

(b)

Figure 4.5: Comparison of five nominal IRFs and perturbed IRFs for (a) D_slit = 21.365 (magnification increase) and (b) D_slit = 22.635 cm (magnification decrease).

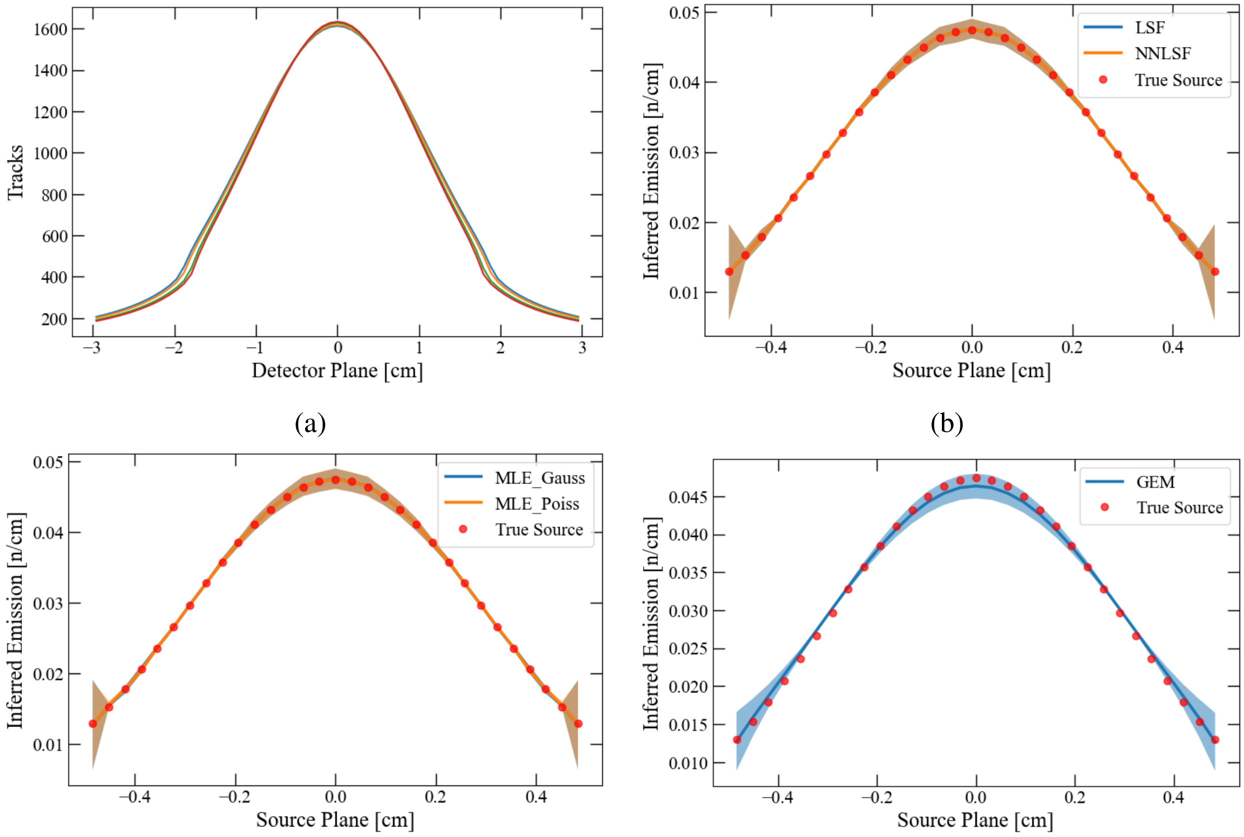

(a) (b)

(c) (d)

Figure 4.6: Low frequency synthetic source reconstruction with four D_slit variation samples. (a) Detector responses generated from four perturbed D_slit IRF matrices. (b) LSF and NNLSF reconstructions mean (solid lines) with one standard deviation envelope (opaque region). (c) MLE_Gauss and MLE_Poiss reconstructions mean (solid lines) with one standard deviation envelope (opaque region). (d) GEM reconstructions mean (solid line) with one standard deviation envelope (opaque region).

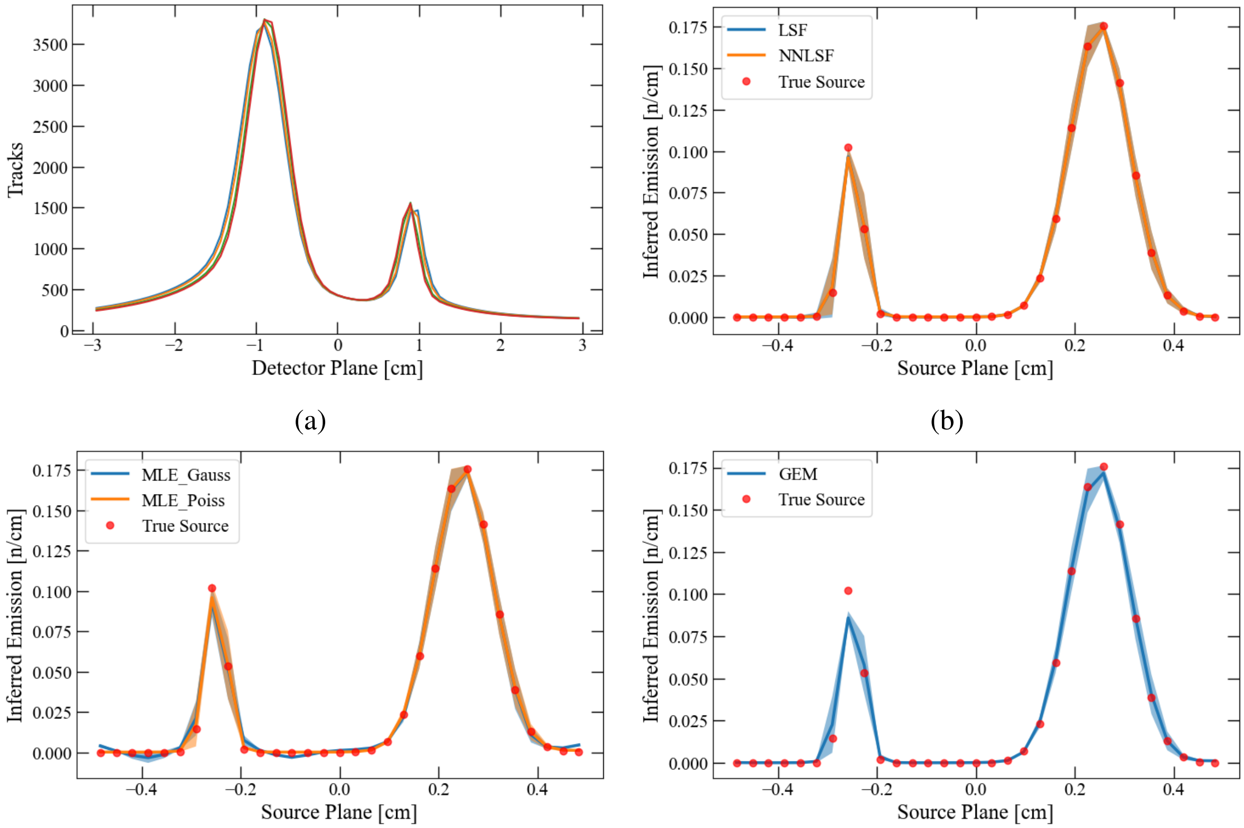

(a) (b)

(c) (d)

Figure 4.7: High frequency synthetic source reconstruction with four D_slit variation samples. (a) Detector responses generated from four perturbed D_slit IRF matrices. (b) LSF and NNLSF reconstructions mean (solid lines) with one standard deviation envelope (opaque region). (c) MLE_Gauss and MLE_Poiss reconstructions mean (solid lines) with one standard deviation envelope (opaque region). (d) GEM reconstructions mean (solid line) with one standard deviation envelope (opaque region).

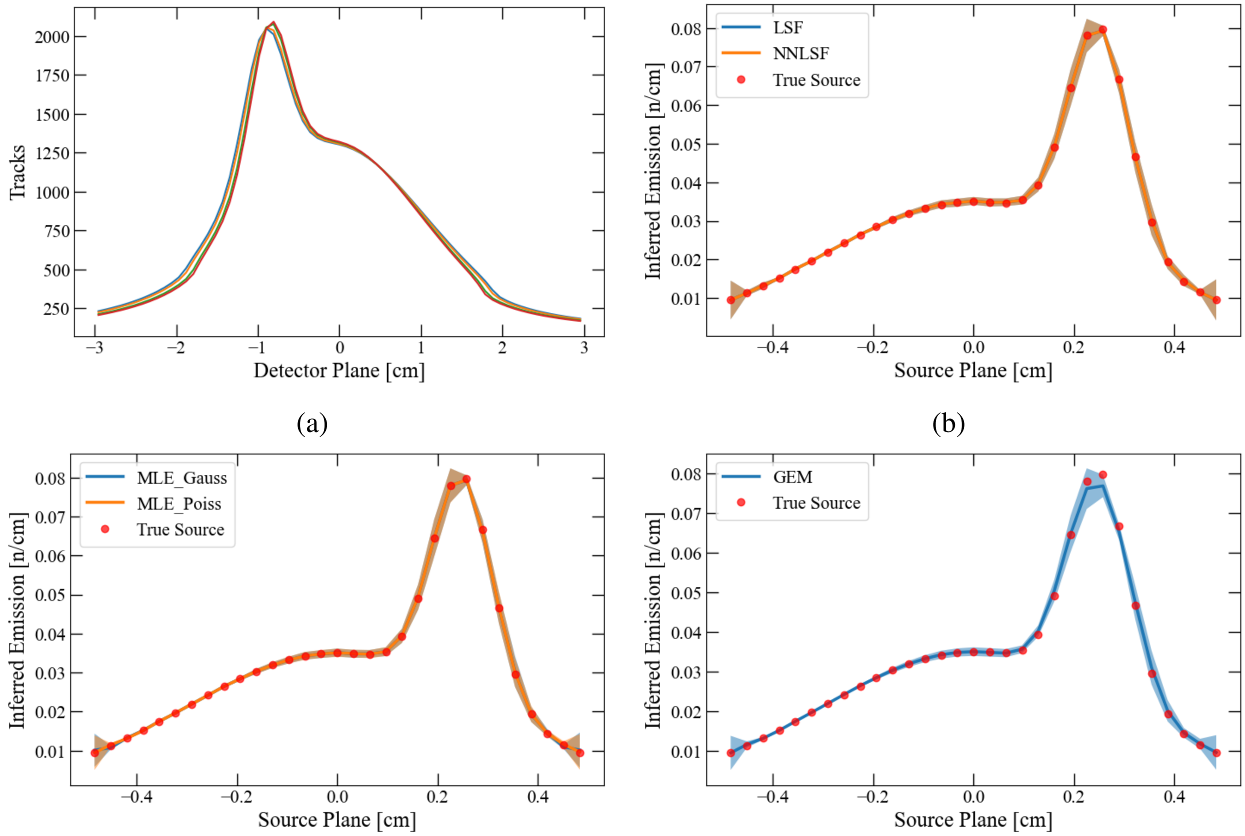

(a) (b)

(c) (d)

Figure 4.8: Mixed frequency synthetic source reconstruction with four D_slit variation samples. (a) Detector responses generated from four perturbed D_slit IRF matrices. (b) LSF and NNLSF reconstructions mean (solid lines) with one standard deviation envelope (opaque region). (c) MLE_Gauss and MLE_Poiss reconstructions mean (solid lines) with one standard deviation envelope (opaque region). (d) GEM reconstructions mean (solid line) with one standard deviation envelope (opaque region).

4.1.3 H_slit Variation

The aperture spacing at the apex of curvature, H_slit, is fixed with two spacers separating the top and bottom tungsten pieces. Spacers manufactured to 250 μm are the most commonly used set. However, a measurement of the aperture spacing was measured with a feeler gauge to be 266 μm. This was used as the nominal parameter, and four perturbed IRF matrices were generated. The values used were 255.4, 260.6, 271.1, and 276.6 μm (uniform samples from -4% to 4%).

By changing the aperture spacing, the IRFs change the width of their flat peaks. Figure 4.9 show that there is minimal change to the IRFs when increasing or decreasing H_slit. Figures 4.10 to 4.12 show the mean reconstructions and standard deviations for a low frequency, high frequency, and mixed frequency source from the four H_slit perturbed detector responses. The effects of altering the aperture spacing did not significantly affect any of the source reconstructions, indicating that H_slit is an insensitive parameter.

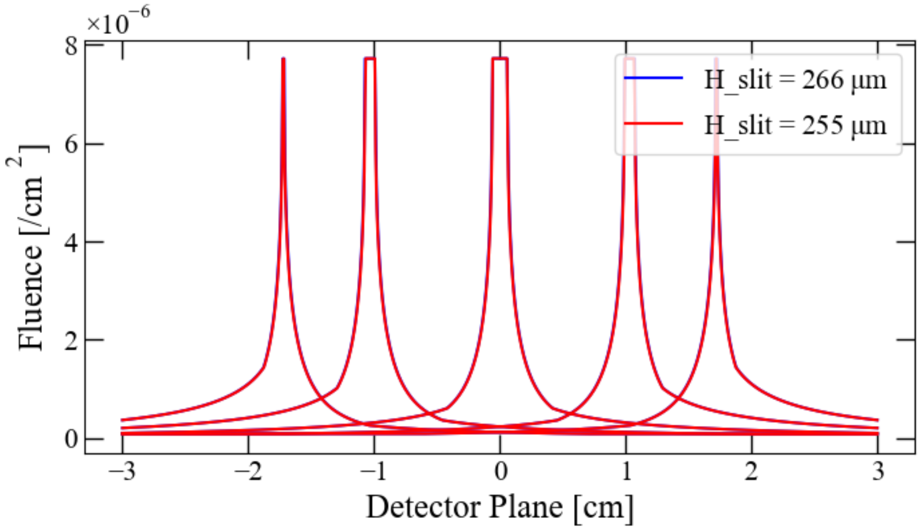

(a)

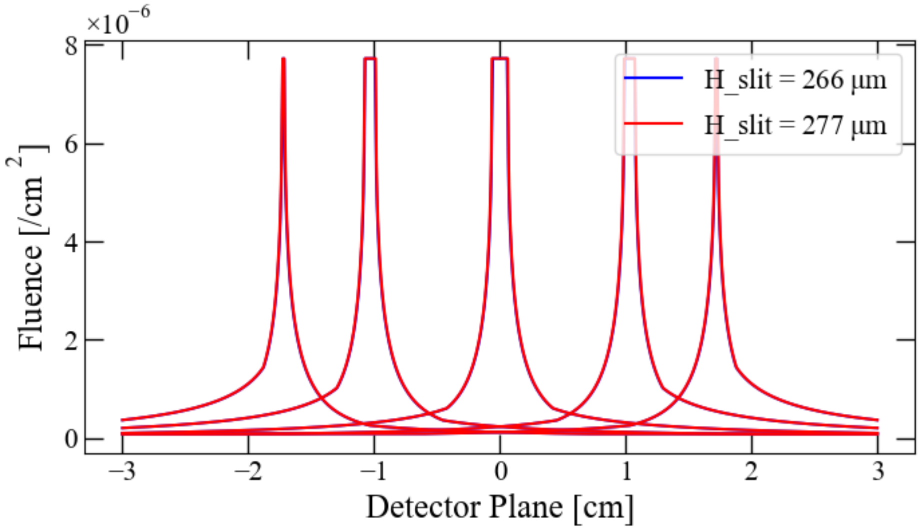

(b)

Figure 4.9: Comparison of five nominal IRFs and perturbed IRFs for (a) H_slit = 255 μm and (b) H_slit = 277 μm.

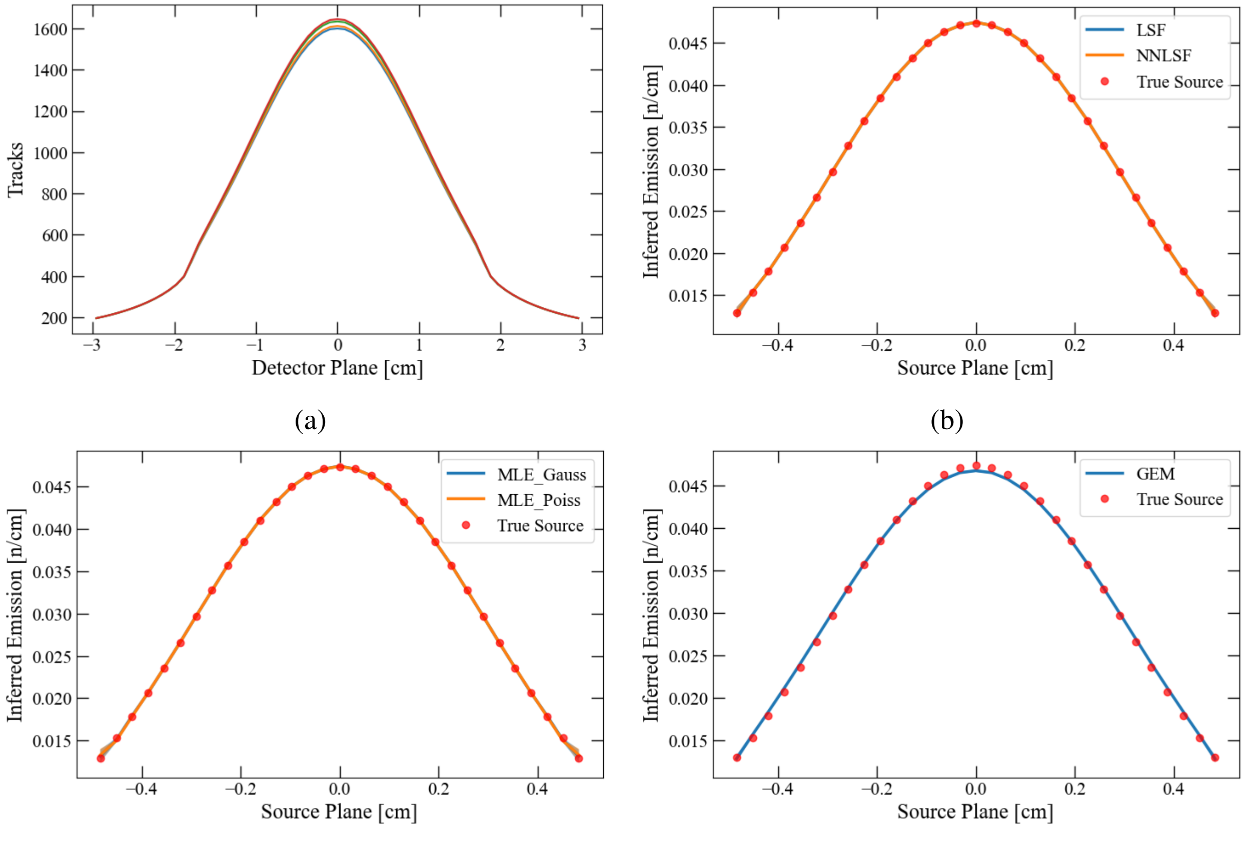

(a)

(b)

(c)

(d)

Figure 4.10: Low frequency synthetic source reconstruction with four H_slit variation samples. (a) Detector responses generated from four perturbed H_slit IRF matrices. (b) LSF and NNLSF reconstructions mean (solid lines) with one standard deviation envelope (opaque region). (c) MLE_Gauss and MLE_Poiss reconstructions mean (solid lines) with one standard deviation envelope (opaque region). (d) GEM reconstructions mean (solid line) with one standard deviation envelope (opaque region).

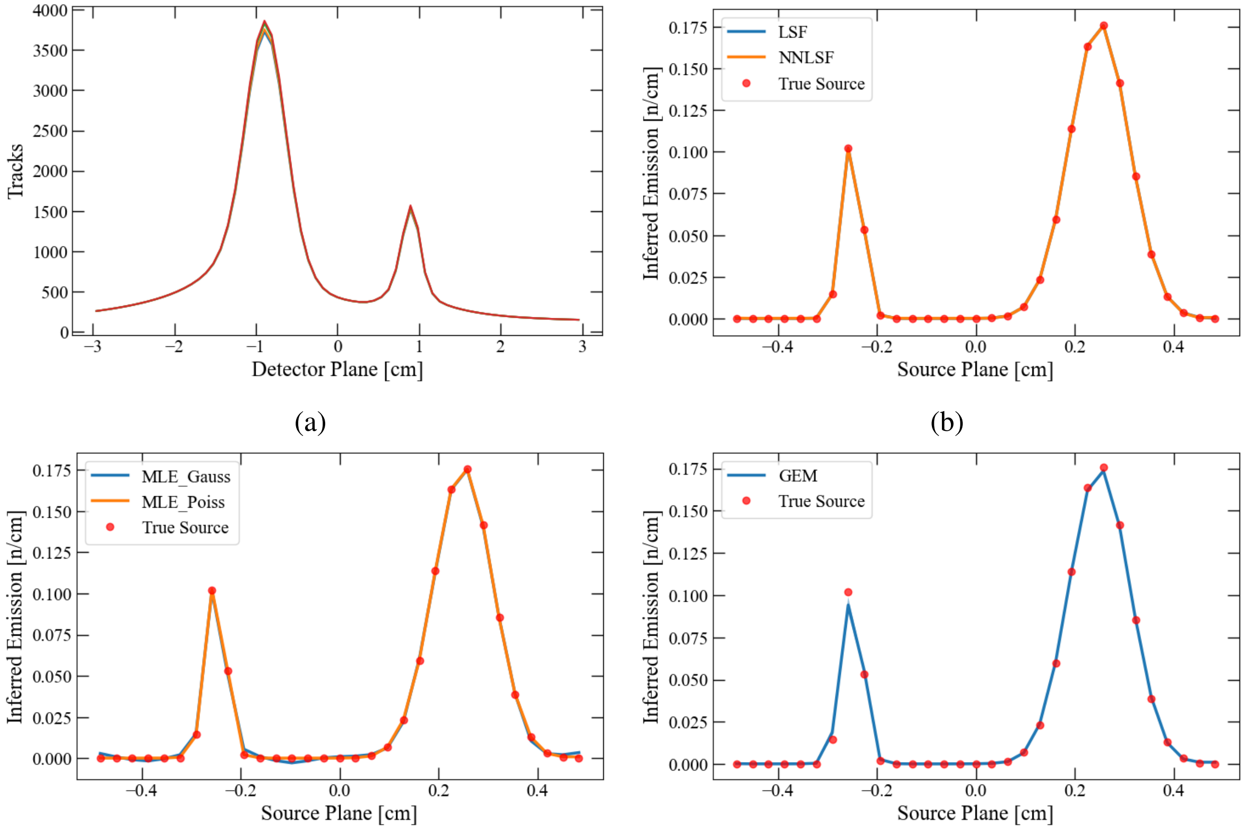

(a) (b)

(c) (d)

Figure 4.11: High frequency synthetic source reconstruction with four H_slit variation samples. (a) Detector responses generated from four perturbed H_slit IRF matrices. (b) LSF and NNLSF reconstructions mean (solid lines) with one standard deviation envelope (opaque region). (c) MLE_Gauss and MLE_Poiss reconstructions mean (solid lines) with one standard deviation envelope (opaque region). (d) GEM reconstructions mean (solid line) with one standard deviation envelope (opaque region).

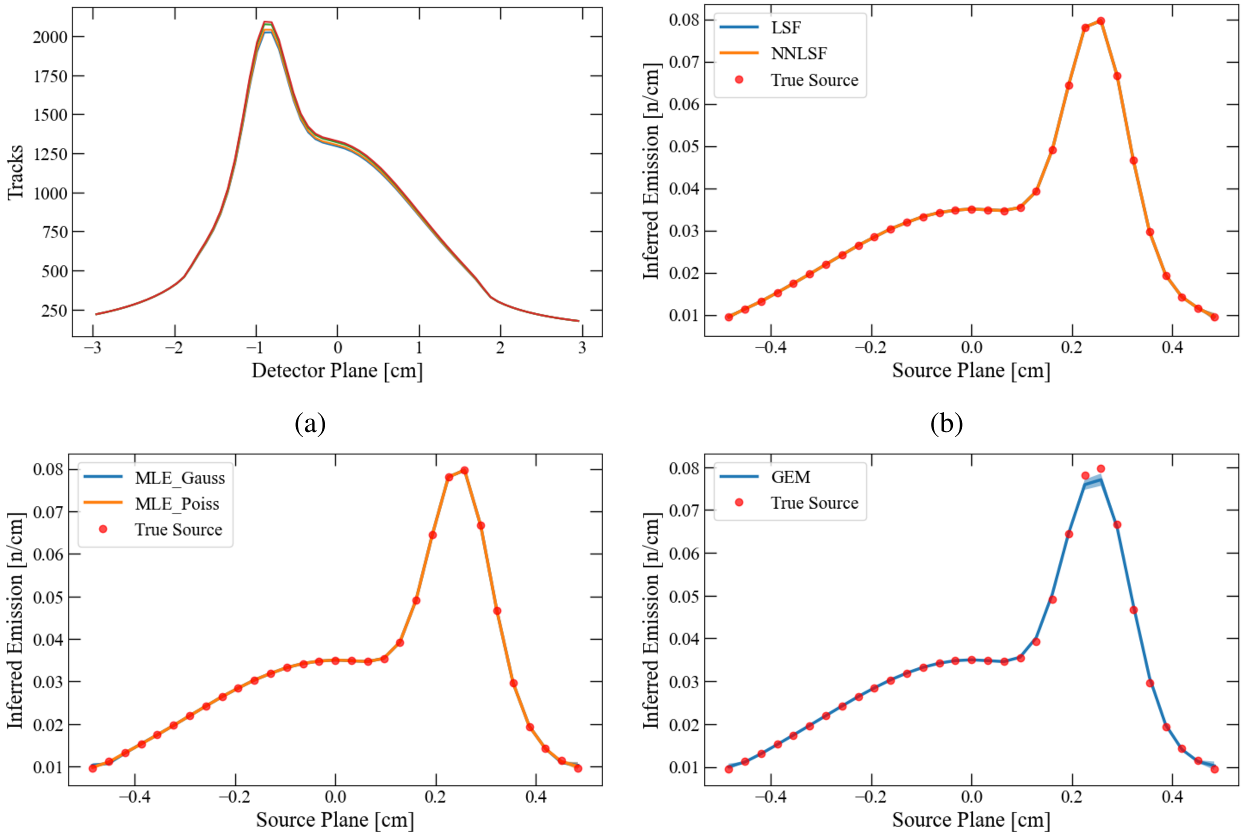

(a) (b)

(c) (d)

Figure 4.12: Mixed frequency synthetic source reconstruction with four H_slit variation samples. (a) Detector responses generated from four perturbed H_slit IRF matrices. (b) LSF and NNLSF reconstructions mean (solid lines) with one standard deviation envelope (opaque region). (c) MLE_Gauss and MLE_Poiss reconstructions mean (solid lines) with one standard deviation envelope (opaque region). (d) GEM reconstructions mean (solid line) with one standard deviation envelope (opaque region).

4.1.4 Z_offset Variation

The aperture housing is mounted independently from the detector housing and the source, allowing for possible misalignment between any of the three. The nominal parameter used was a direct alignment of the source, aperture spacing, and detector midpoints. There are relatively few modifications that can be made to improve alignment in-chamber. Adjusting the source upward with 0.005" (0.0127 cm) shims is the common method used in-chamber, and measurements within ± 0.0025” (0.00635 cm) are acceptable. This adjustment is intended to correctly align the target, however, if shims are or aren’t used by mistake the measurement could be off by 0.0127 ± 0.00635 cm. To estimate this range, perturbations were z-axis shifts of the entire aperture in increments of 0.005 cm. The values used ranged from -0.015 to 0.015, with six total perturbations.

Figure 4.13 shows that Z_offset variations have two major effects when compared to the nominal IRFs. First, each of the IRFs have shifted their peak location in the same direction as the offset. Second, the widths of each IRF begin to change due to increases or decreases in the unattenuated line of sight path through the aperture. When shifting upward (+z-axis) neutron emission near the top of the source will see an increase in the aperture spacing, leading to wider IRFs at the negative portion of the detector plane (the image is naturally inverted). The opposite effect happens when shifting the aperture down.

Figures 4.14 to 4.16 show the mean reconstructions and standard deviations for a low frequency, high frequency, and mixed frequency source from the eight Z_offset perturbed detector responses. It can be seen that the detector response is shifted in all three sources. In addition, edge effects similar to those seen in D_slit begin to appear in the low and mix frequency sources. The same effect is happening where the outermost nominal IRFs cannot account for signal beyond a certain point and are trying to compensate.

It should be noted that shifting the aperture is not entirely correct with the previously described assumptions. A shift in target location, is no different than shifting both the aperture and detector in the opposite direction. However, when shifting the aperture by a small amount, the change can be significant due to the solid angle being more influential the closer to the source an object is. Shifts of 0.015 cm at the detector plane do not noticeably influence the detector response or reconstructions.

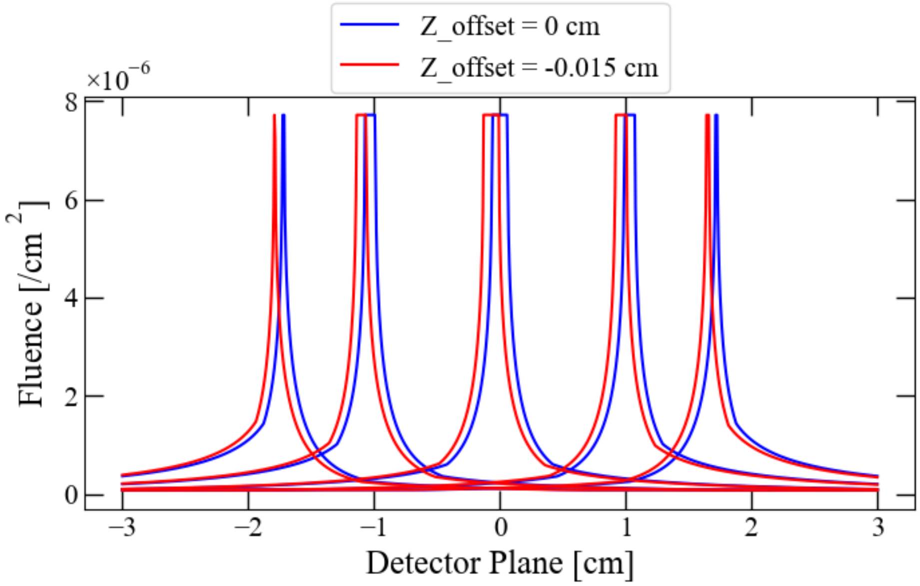

(a)

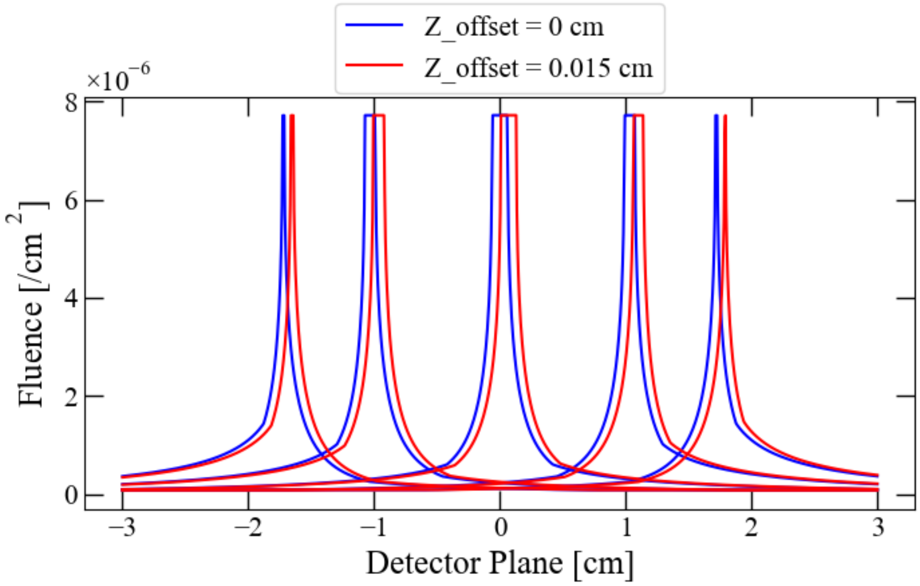

(b)

Figure 4.13: Comparison of five nominal IRFs and perturbed IRFs for (a) Z_offset = -0.015 cm and (b) Z_offset = 0.015 cm.

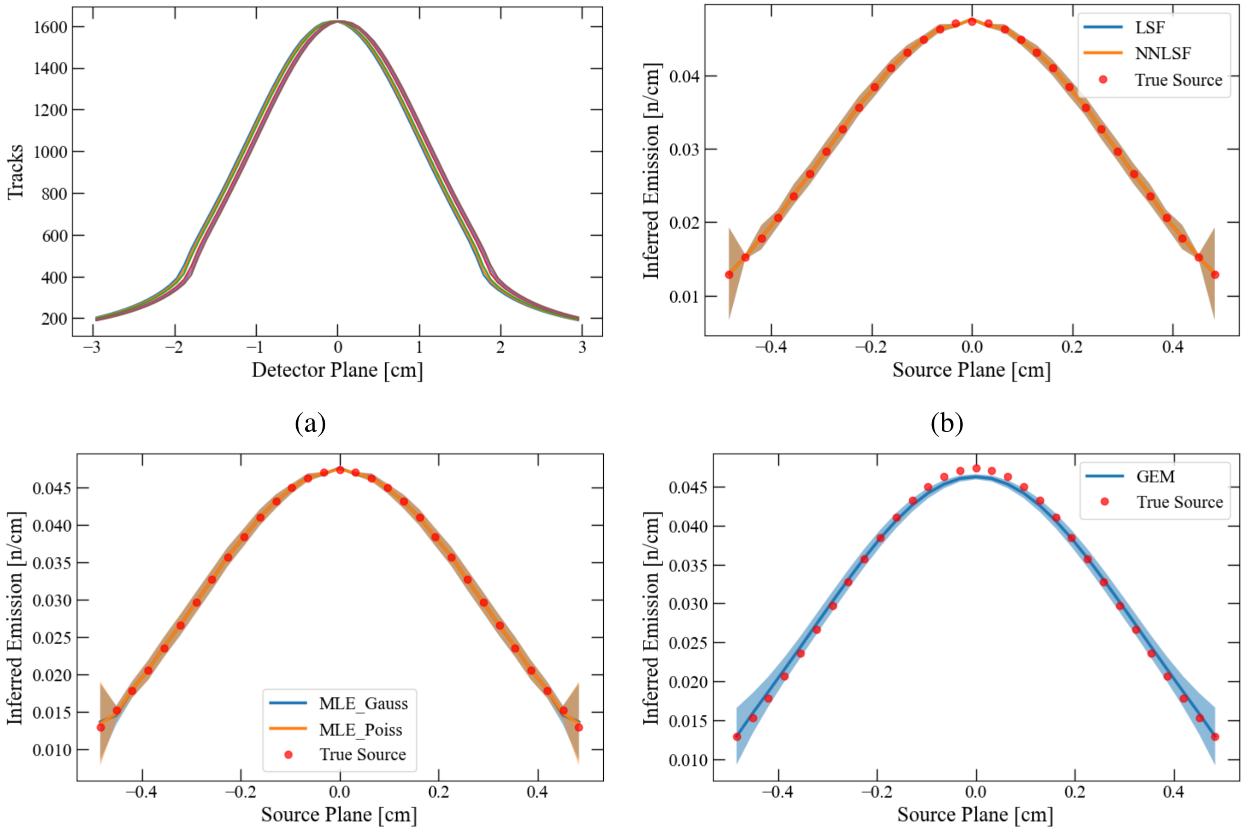

(a) (b)

(c) (d)

Figure 4.14: Low frequency synthetic source reconstruction with six Z_offset variation samples. (a) Detector responses generated from six perturbed Z_offset variation samples. IRF matrices. (b) LSF and NNLSF reconstructions mean (solid lines) with one standard deviation envelope (opaque region). (c) MLE_Gauss and MLE_Poiss reconstructions mean (solid lines) with one standard deviation envelope (opaque region). (d) GEM reconstructions mean (solid line) with one standard deviation envelope (opaque region).

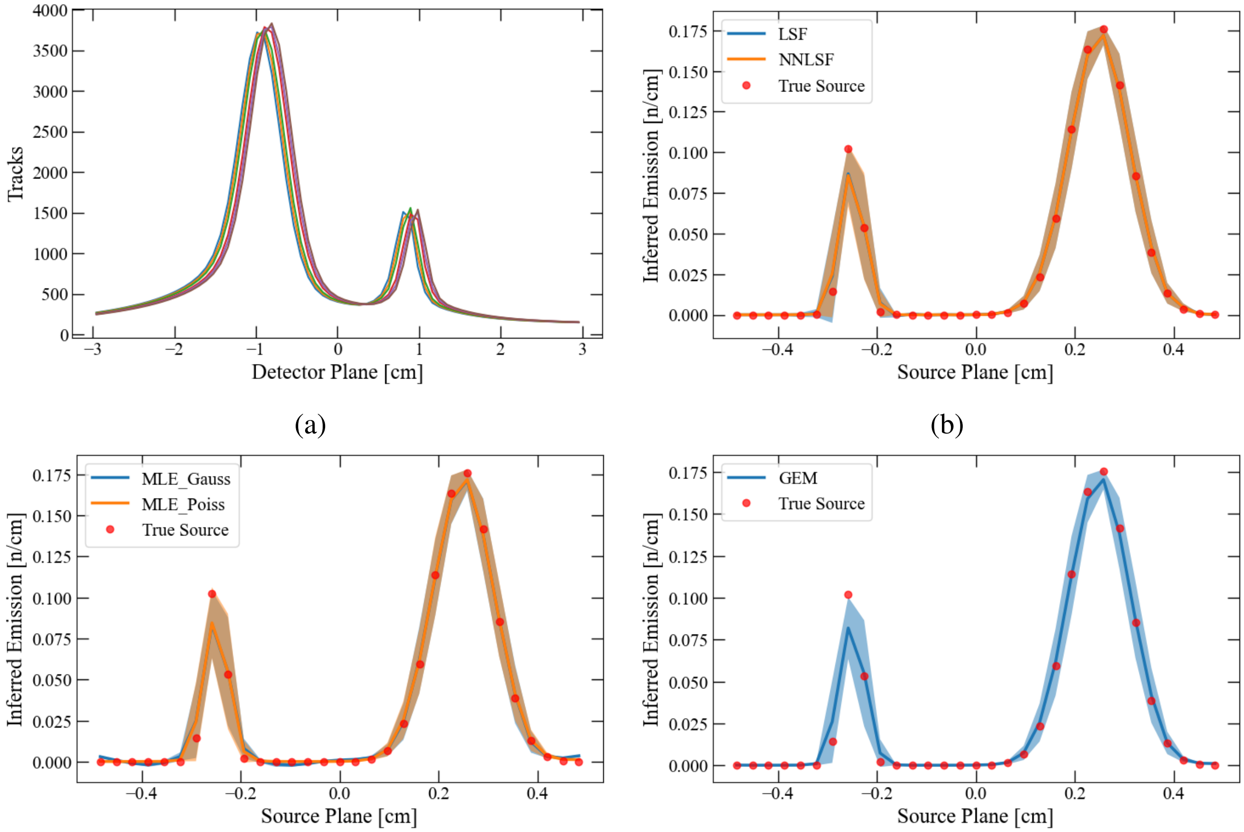

(a)

(b)

(c)

(d)

Figure 4.15: High frequency synthetic source reconstruction with six Z_offset variation samples. (a) Detector responses generated from six perturbed Z_offset variation samples. IRF matrices. (b) LSF and NNLSF reconstructions mean (solid lines) with one standard deviation envelope (opaque region). (c) MLE_Gauss and MLE_Poiss reconstructions mean (solid lines) with one standard deviation envelope (opaque region). (d) GEM reconstructions mean (solid line) with one standard deviation envelope (opaque region).

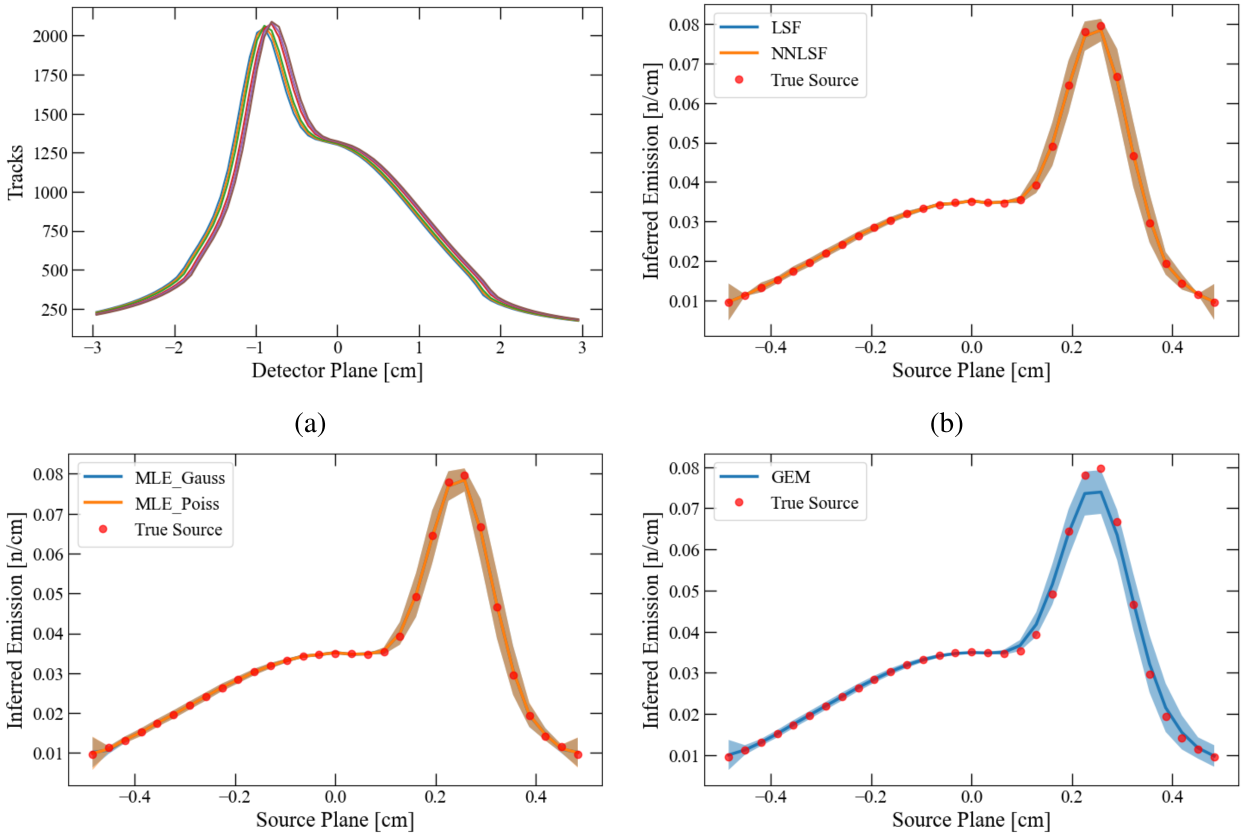

(a)

(b)

(c)

(d)

Figure 4.16: Mixed frequency synthetic source reconstruction with six Z_offset variation samples. (a) Detector responses generated from six perturbed Z_offset variation samples. IRF matrices. (b) LSF and NNLSF reconstructions mean (solid lines) with one standard deviation envelope (opaque region). (c) MLE_Gauss and MLE_Poiss reconstructions mean (solid lines) with one standard deviation envelope (opaque region). (d) GEM reconstructions mean (solid line) with one standard deviation envelope (opaque region).

4.1.5 Theta Variation

Previously shown in Figure 1.4 (b), the aperture housing is mounted to the aperture ring by a mounting plate at one end. Between experiments, the aperture housing is occasionally refurbished and reused in a future experiment. From the force exerted on the housing, the mounting plate or housing can be bent in such a way that angles the aperture housing. If reused in future experiments, the bending can slightly angle the aperture downward, shown as the angle Theta in Figure 4.1.

Accurate Theta parameter ranges were challenging to estimate. Measurements in a laboratory setting were taken with a digital level accurate only to the first decimal. Three individual aperture housings had their angles measured on two different mounting plates of different heights. Each angle was measured with the housing alone, then with the aperture placed inside. This was repeated in two mounting positions on a test aperture ring, 180° from one another. Results indicated that the tolerance of the machined parts commonly created a -0.1° angle, occasionally reaching -0.2°. To estimate this variation, sensitivity study perturbations chosen were at angles up to -0.25°, in increments of 0.05°. The values used were -0.25°, -0.2°, -0.15°, -0.1°, and -0.05°.

Figure 4.17 shows the nominal and perturbed IRFs with angles -0.05° and -0.25° Similar to Z_offset, the IRFs peak widths will change width when rotating the aperture, but instead do not shift location. However, the perturbation to Theta is likely to occur in only one direction, causing the IRF changes to be asymmetric. This causes source contribution in the +z direction to increase, leading to increased detection in the negative half of the detector. The changes to the IRFs are not only decreasing the peak widths along the negative half of the detector. With the angle of the aperture changing, source points near the negative extent of the source area lose the direct line of sight to the detector plane. Instead, neutrons can only pass through the top tungsten piece or through both tungsten pieces of the aperture. Due to the rotation of the aperture, the tails of the spread functions change as the distance traveled through the aperture differs.

Figures 4.18 to 4.20 show the mean reconstructions and standard deviations for a low frequency, high frequency, and mixed frequency source from the four Theta perturbed detector responses. These figures indicate the reconstructions are affected near the edges in an asymmetric fashion. This is caused once again by the perturbations influence on the outermost IRFs.

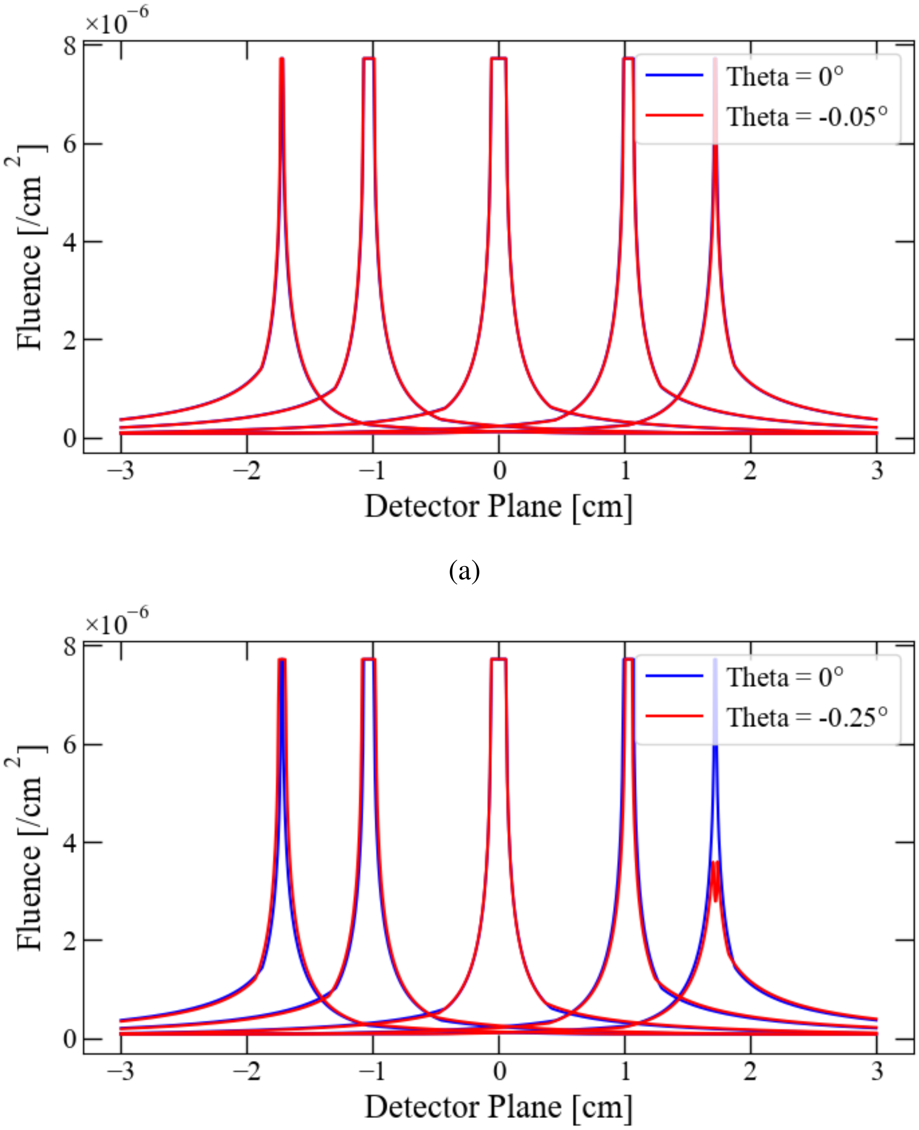

(a)

(b)

Figure 4.17: Comparison of five nominal IRFs and perturbed IRFs for (a) Theta = $-0.05°$ and (b) Theta = $-0.25°$.

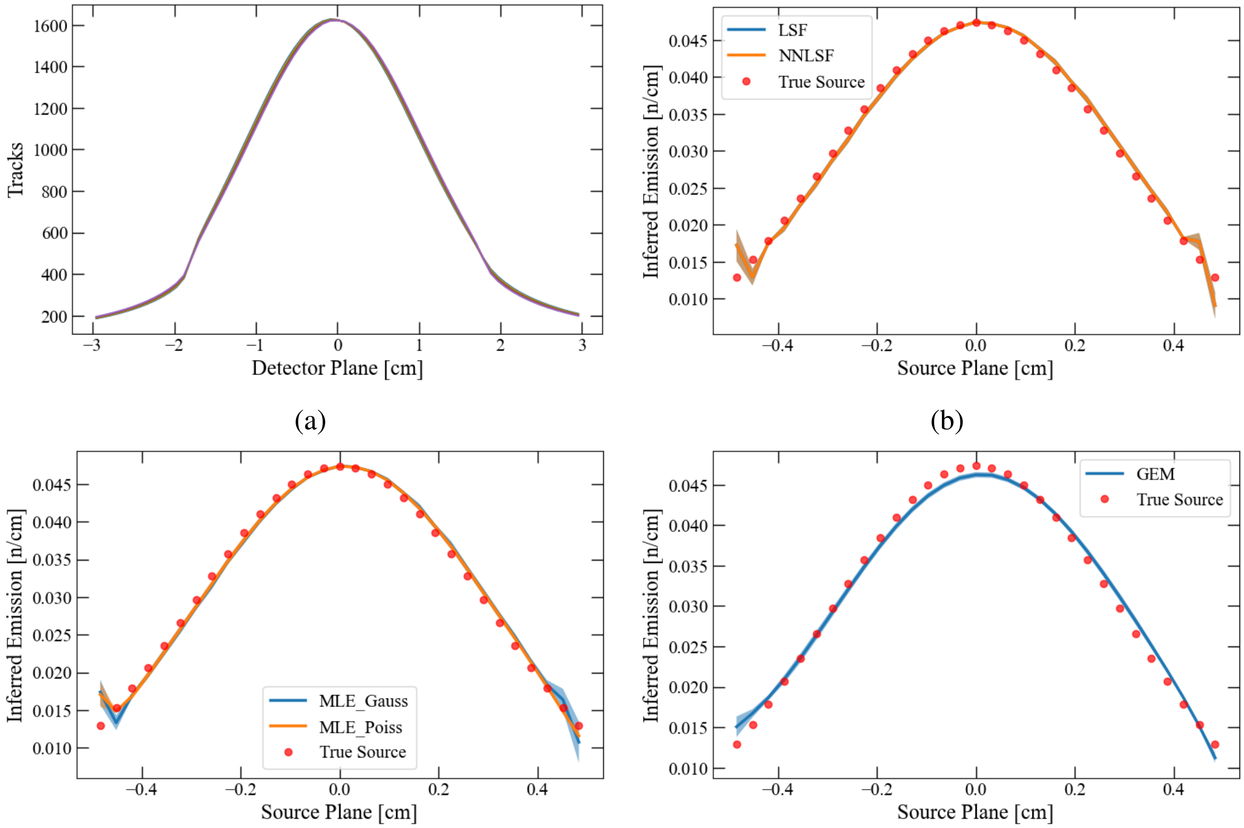

(a) (b)

(c) (d)

Figure 4.18: Low frequency synthetic source reconstruction with five Theta variation samples. (a) Detector responses generated from five Theta variation samples. IRF matrices. (b) LSF and NNLSF reconstructions mean (solid lines) with one standard deviation envelope (opaque region). (c) MLE_Gauss and MLE_Poiss reconstructions mean (solid lines) with one standard deviation envelope (opaque region). (d) GEM reconstructions mean (solid line) with one standard deviation envelope (opaque region).

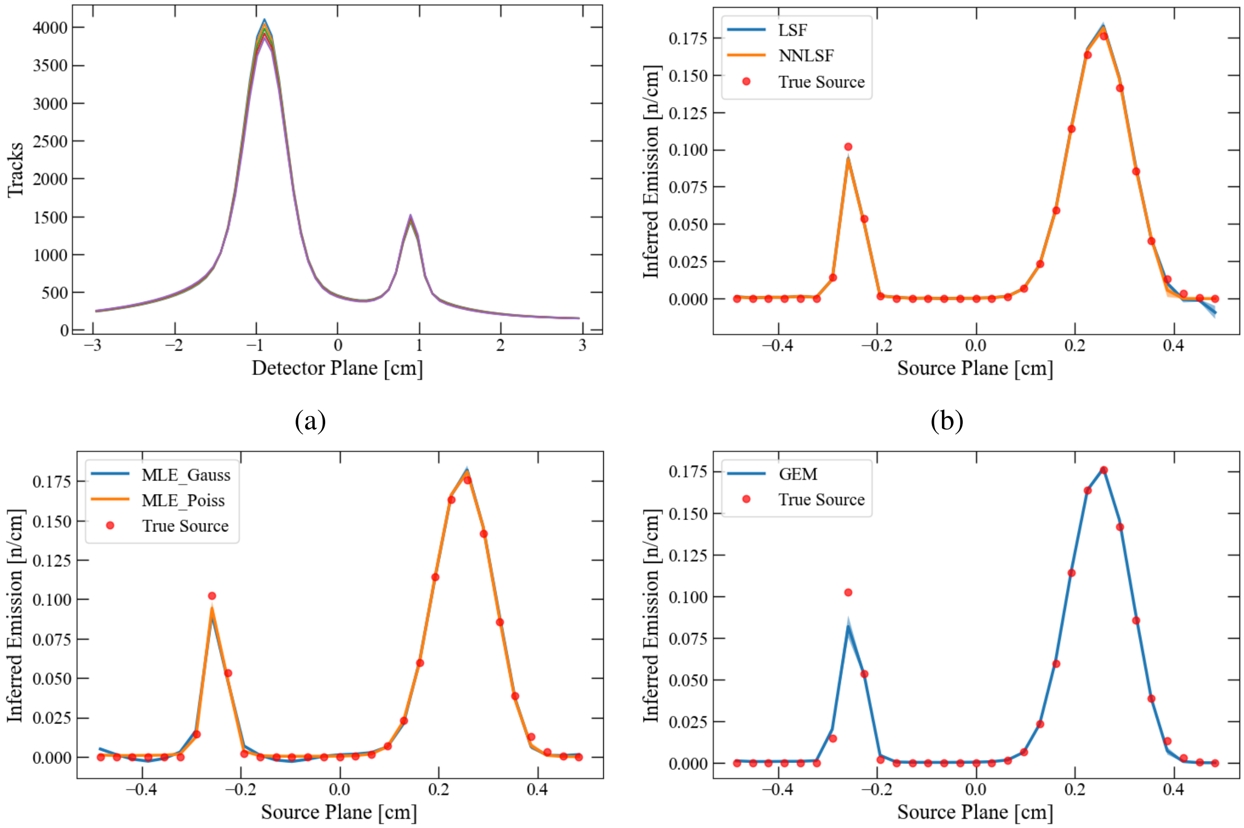

(a) (b)

(c) (d)

Figure 4.19: High frequency synthetic source reconstruction with five Theta variation samples. (a) Detector responses generated from five Theta variation samples. IRF matrices. (b) LSF and NNLSF reconstructions mean (solid lines) with one standard deviation envelope (opaque region). (c) MLE_Gauss and MLE_Poiss reconstructions mean (solid lines) with one standard deviation envelope (opaque region). (d) GEM reconstructions mean (solid line) with one standard deviation envelope (opaque region).

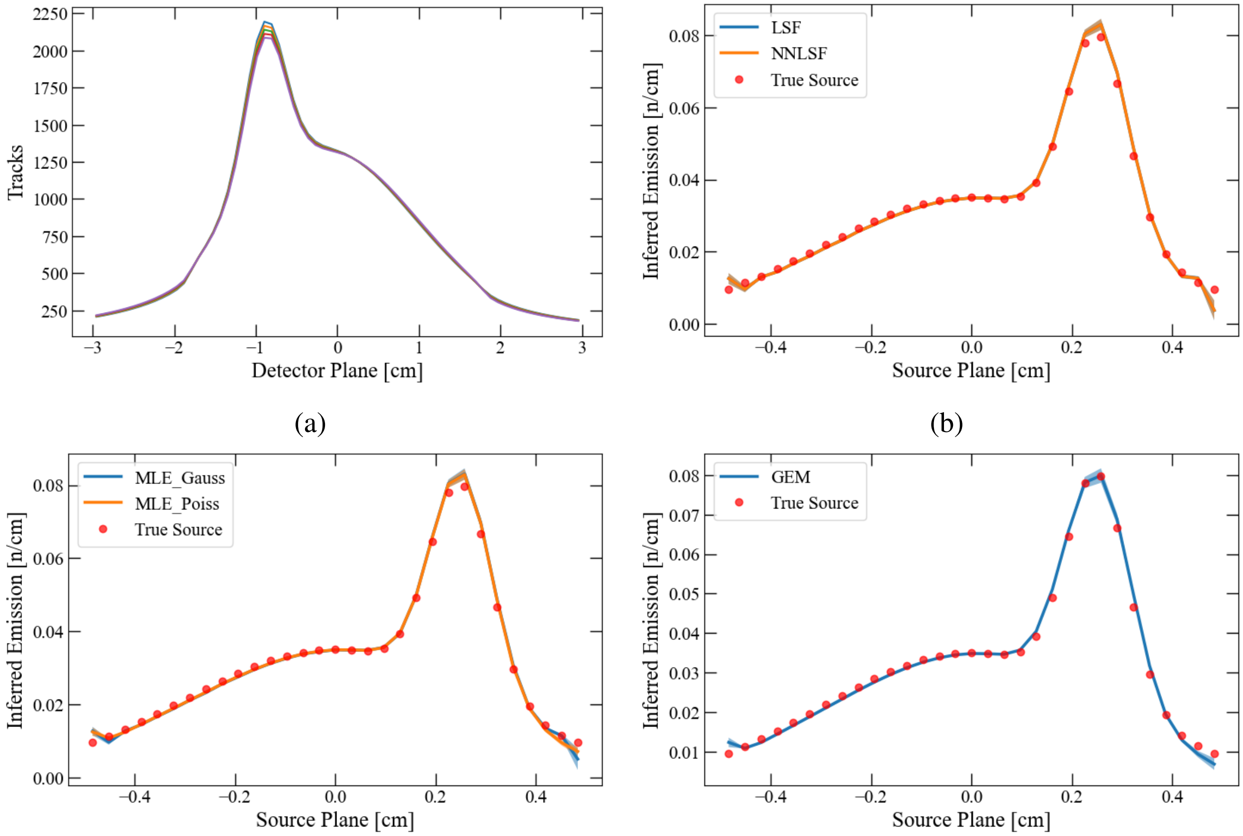

(a) (b)

(c) (d)

Figure 4.20: Mixed frequency synthetic source reconstruction with five Theta variation samples. (a) Detector responses generated from five Theta variation samples. IRF matrices. (b) LSF and NNLSF reconstructions mean (solid lines) with one standard deviation envelope (opaque region). (c) MLE_Gauss and MLE_Poiss reconstructions mean (solid lines) with one standard deviation envelope (opaque region). (d) GEM reconstructions mean (solid line) with one standard deviation envelope (opaque region).

4.2 Error Estimation

4.2.1 Latin Hypercube Sampling

Now that each individual parameter has been evaluated, the error propagation from all parameters can be estimated by accumulating perturbations. A useful way to generate IRF matrices with perturbations in every parameter is by randomly sampling each perturbed value from the entire possible domain. However, biasing can become an issue if the samples from one or more of the parameters do not adequately represent the possible range. Latin hypercube sampling (LHS) is an approach that does not allow redundant parameter values between each sample [38]. This creates more uniform sampling throughout the parameter space.

Each generated LHS array contain parameters D_slit Z_offset, and Theta. Values from H_slit were not included because of its low sensitivity compared to the other three parameters. For this example ten IRF matrices were created from the randomly sampled domain of each parameter. As before, the perturbed matrices generated synthetic detector responses which were used for source reconstructions.

This section also introduces the effects of noise, as a way to determine if the LHS error propagation is overwhelmed by statistical noise. The following subsections are divided into the type of synthetic source being reconstructed, low frequency, high frequency, and mixed frequency. For each synthetic source, the LHS reconstructions were performed on the nominal detector response with no added noise. This solution space provides an estimated range of error propagation given our parameter uncertainties. Next, Poissonian noise was introduced as described in Section 4.1.1 for each of the ten LHS synthetic responses. This was performed three separate times, with varying total neutron yields of 2×10^{12}, 1×10^{13}, and 5×10^{13}. Each of these have a different SNR, proportional to the yield, and elucidate whether the model's estimated error or noise is a dominant factor.

4.2.1.1 Low Frequency LHS Reconstructions

Low frequency synthetic reconstructions of the ten noiseless LHS responses can be seen in Figure 4.21. Asymmetric Edge effects are clearly seen in the reconstructions, but less sharp in the GEM reconstruction. This is a property of regularization smoothing out large discontinuities. Figures 4.22 to 4.24 show the mean reconstructions and standard deviations of a low frequency source with neutron yields of 2×10^{12}, 1×10^{13}, and 5×10^{13}. Increasing the SNR of synthetic data clearly decreases the overall variance of the reconstructions and begins to approach the range of uncertainty seen in Figure 4.21, with the exclusion of the GEM method. In each of the reconstructions, the GEM method appears to have similar variance with all neutron yields. GEM also appears to dampen the edge effects marginally better than the other reconstruction methods.

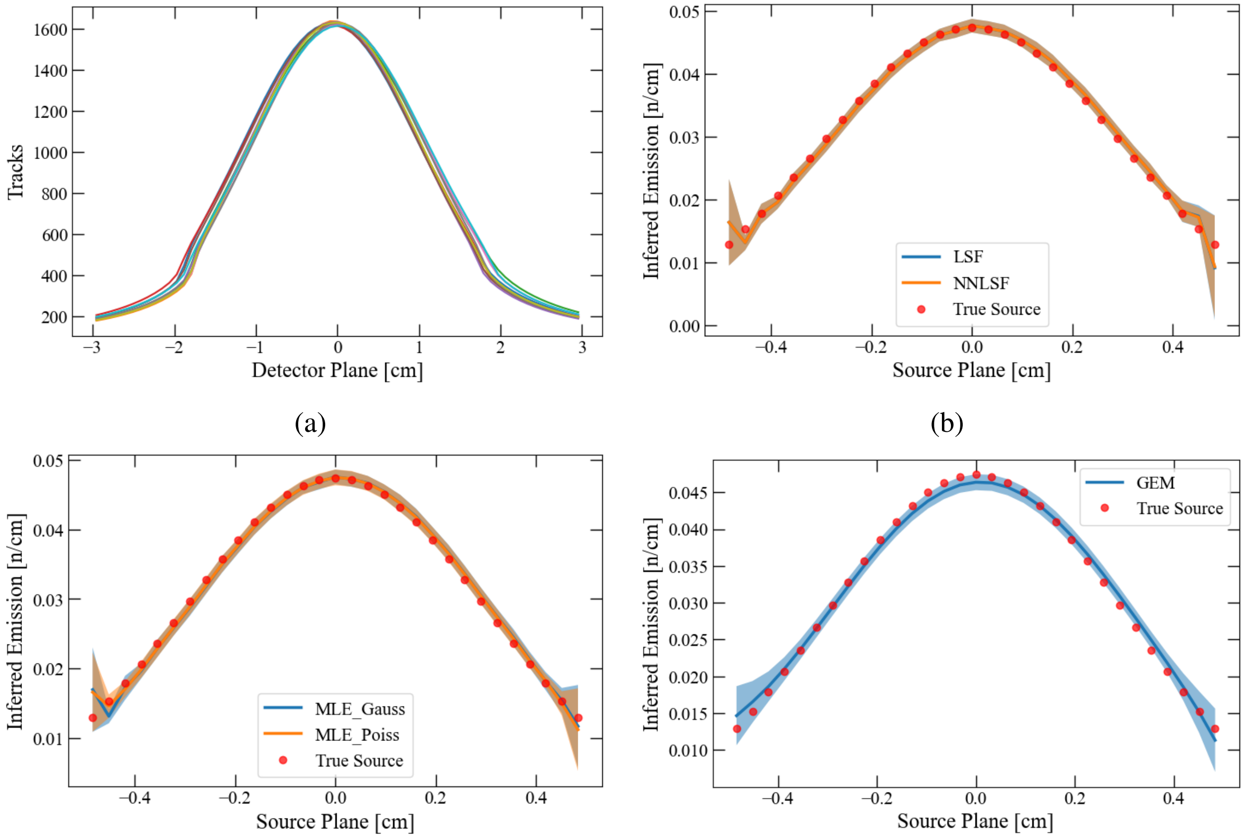

(a)

(b)

(c)

(d)

Figure 4.21: Low frequency synthetic source reconstruction with ten LHS responses. (a) Detector responses generated from ten LHS noiseless IRF matrices. (b) LSF and NNLSF reconstructions mean (solid lines) with one standard deviation envelope (opaque region). (c) MLE_Gauss and MLE_Poiss reconstructions mean (solid lines) with one standard deviation envelope (opaque region). (d) GEM reconstructions mean (solid line) with one standard deviation envelope (opaque region).

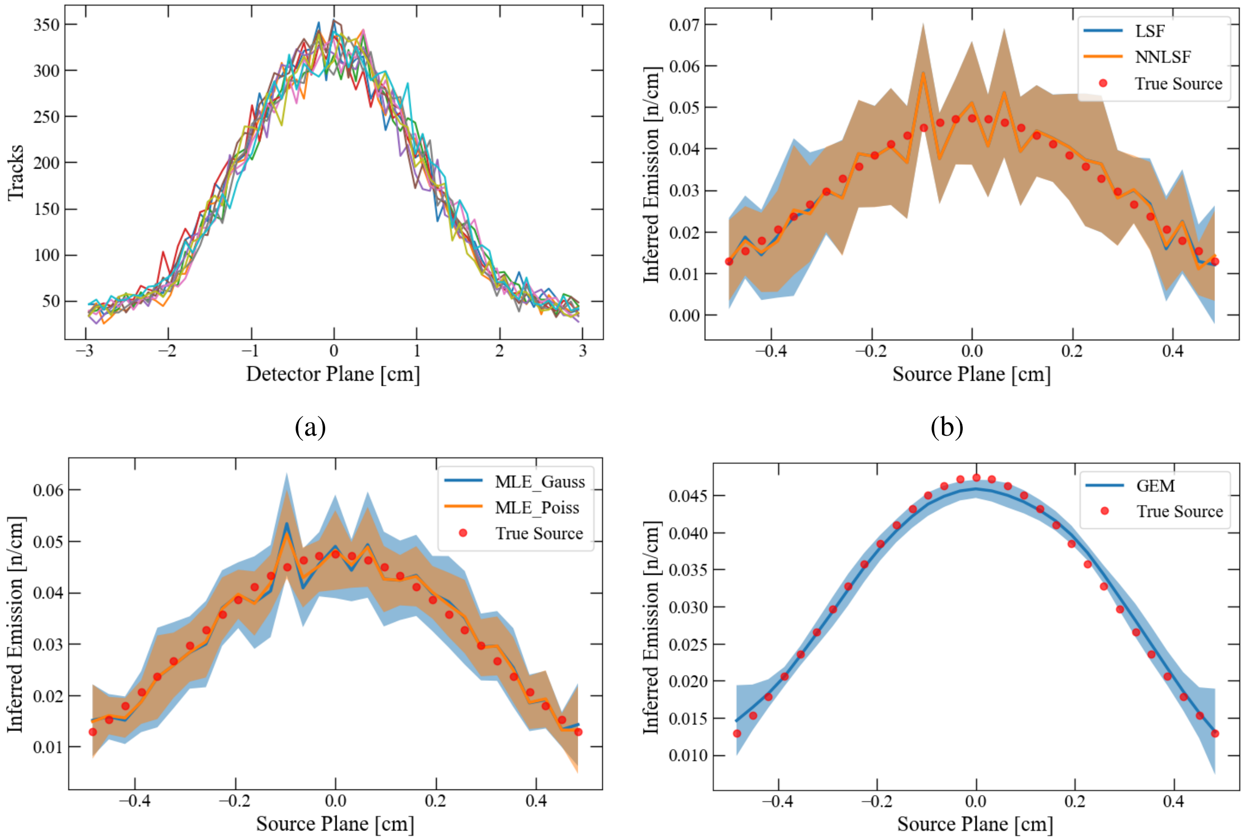

(a) (b)

(c) (d)

Figure 4.22: Low frequency synthetic source reconstruction with ten LHS responses, including added noise from 2×10^{12} neutron yield. (a) Detector responses generated from ten LHS IRF matrices, including added noise from 2×10^{12} neutron yield. (b) LSF and NNLSF reconstructions mean (solid lines) with one standard deviation envelope (opaque region). (c) MLE_Gauss and MLE_Poiss reconstructions mean (solid lines) with one standard deviation envelope (opaque region). (d) GEM reconstructions mean (solid line) with one standard deviation envelope (opaque region).

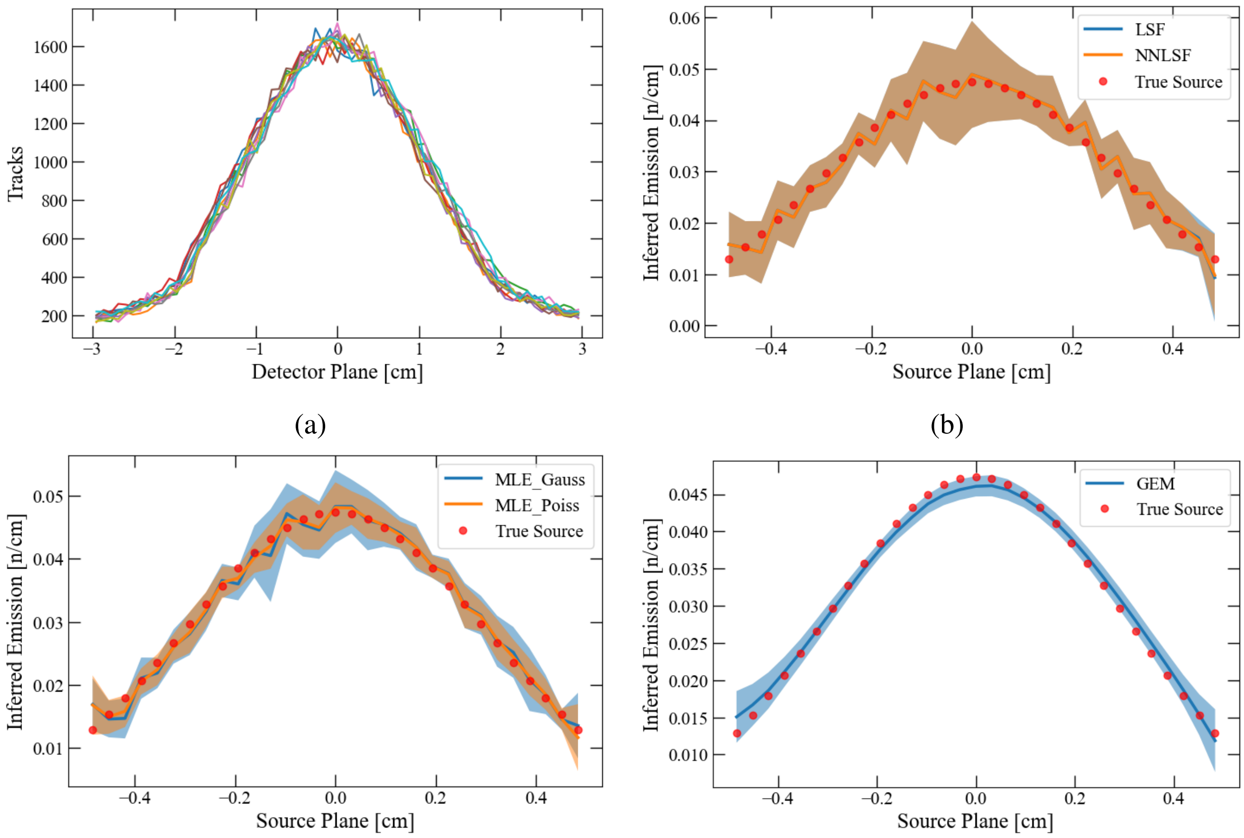

(a) (b) (c) (d)

Figure 4.23: Low frequency synthetic source reconstruction with ten LHS responses, including added noise from 1×10^{13} neutron yield. (a) Detector responses generated from ten LHS IRF matrices, including added noise from 1×10^{13} neutron yield. (b) LSF and NNLSF reconstructions mean (solid lines) with one standard deviation envelope (opaque region). (c) MLE_Gauss and MLE_Poiss reconstructions mean (solid lines) with one standard deviation envelope (opaque region). (d) GEM reconstructions mean (solid line) with one standard deviation envelope (opaque region).

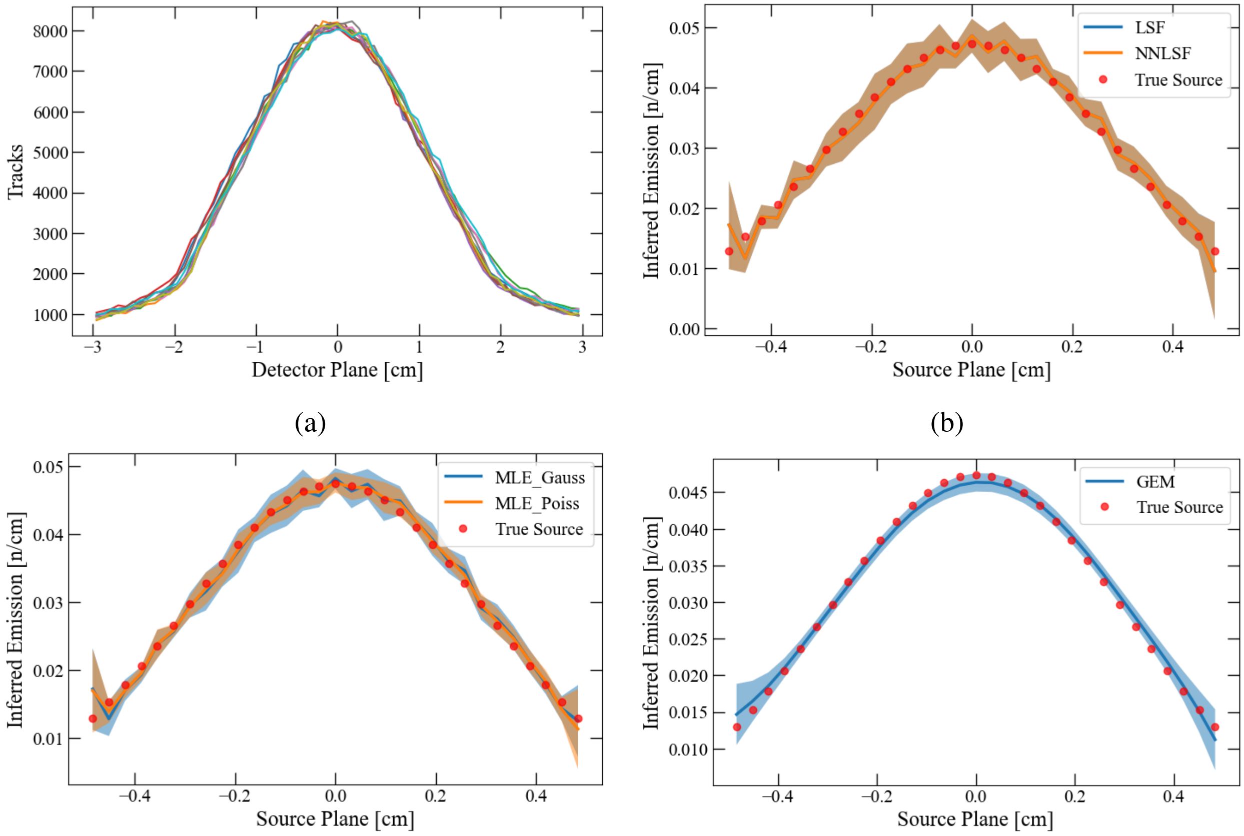

(a) (b)

(c) (d)

Figure 4.24: Low frequency synthetic source reconstruction with ten LHS responses, including added noise from 5×10^{13} neutron yield. (a) Detector responses generated from ten LHS IRF matrices, including added noise from 5×10^{13} neutron yield. (b) LSF and NNLSF reconstructions mean (solid lines) with one standard deviation envelope (opaque region). (c) MLE_Gauss and MLE_Poiss reconstructions mean (solid lines) with one standard deviation envelope (opaque region). (d) GEM reconstructions mean (solid line) with one standard deviation envelope (opaque region).

4.2.1.2 High Frequency LHS Reconstructions

High frequency synthetic reconstructions of the ten noiseless LHS responses (Figure 4.25) and noise induced reconstructions (Figures 4.26 to 4.28) appear to have minimal change between them. The lower amplitude peak is under-predicted, a feature previously seen in each of the individually perturbed reconstructions. Interestingly, the change in overall neutron yield had little effect compared to the low frequency solutions. However, GEM appears once again to have the least change in variance across the different neutron yields, though less significant than in the low frequency source.

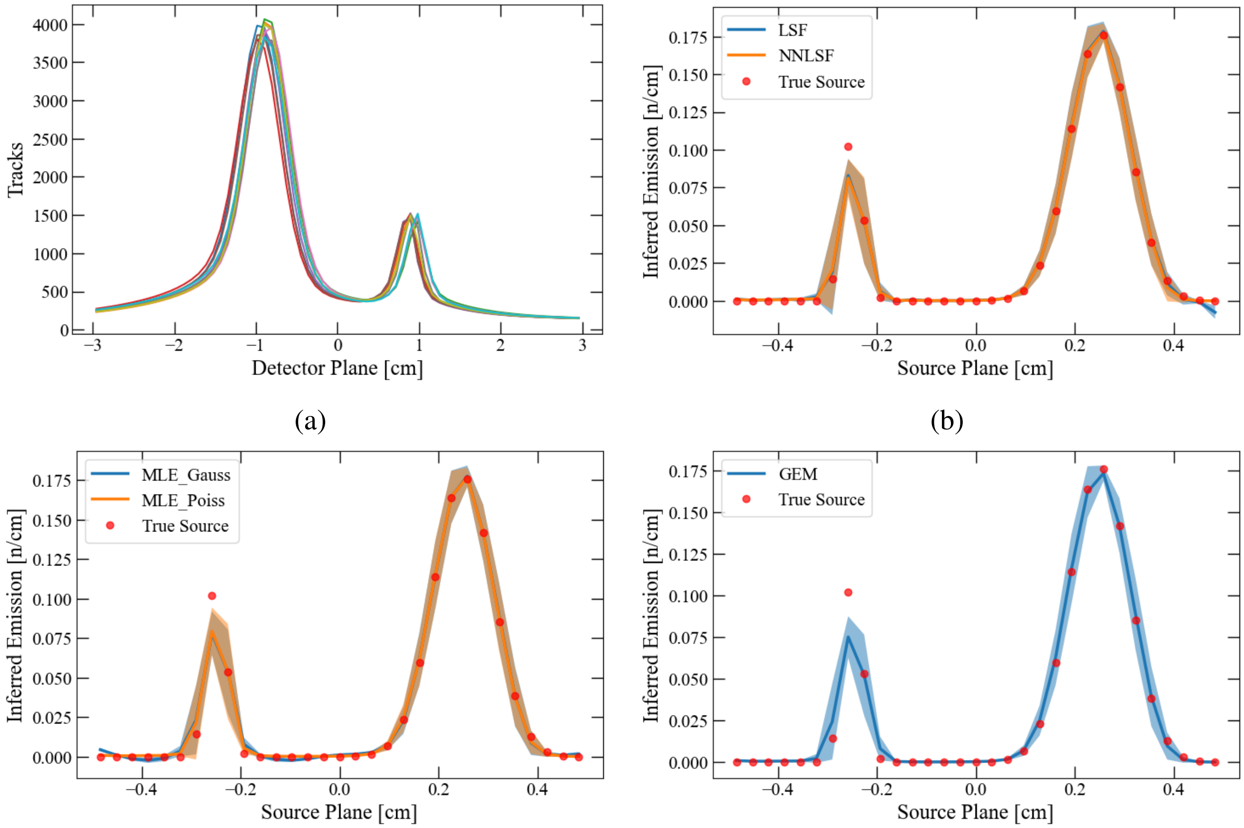

(a) (b)

(c) (d)

Figure 4.25: High frequency synthetic source reconstruction with ten LHS responses. (a) Detector responses generated from ten LHS noiseless IRF matrices. (b) LSF and NNLSF reconstructions mean (solid lines) with one standard deviation envelope (opaque region). (c) MLE_Gauss and MLE_Poiss reconstructions mean (solid lines) with one standard deviation envelope (opaque region). (d) GEM reconstructions mean (solid line) with one standard deviation envelope (opaque region).

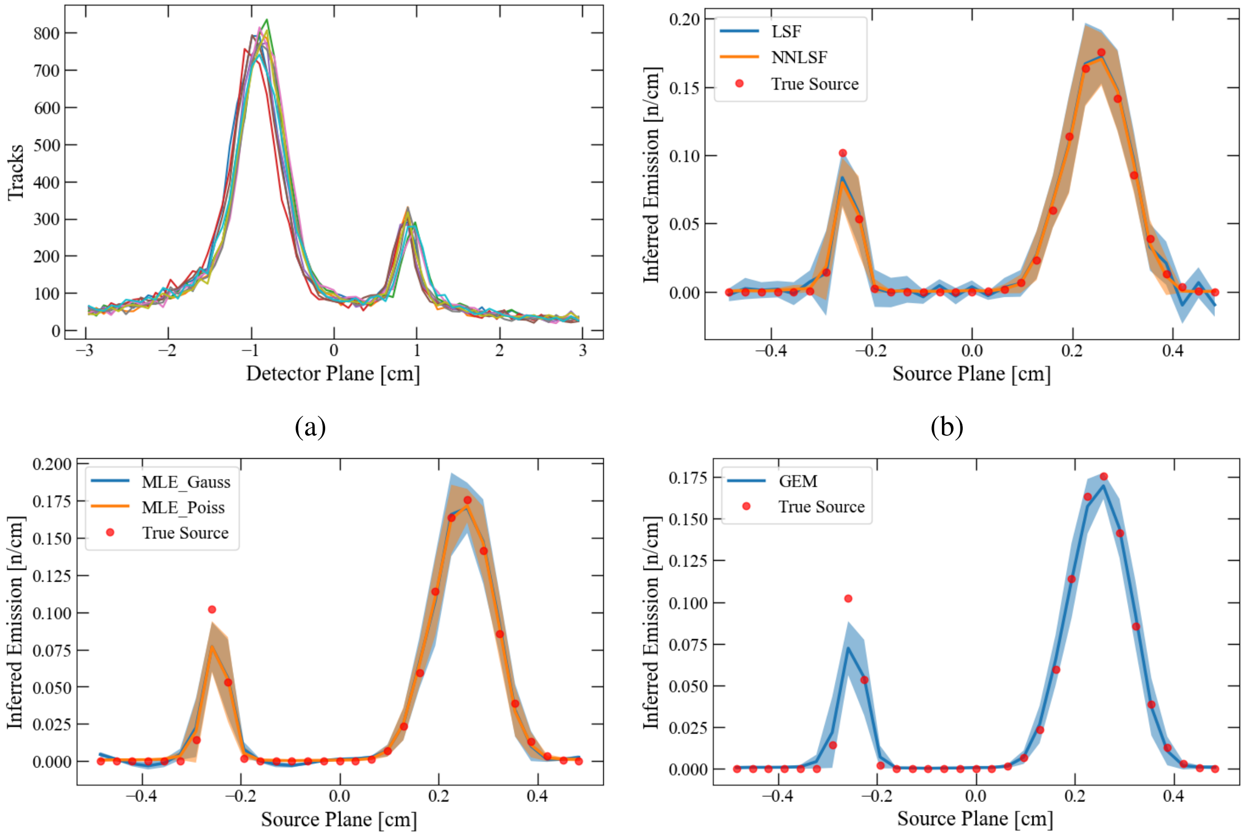

(a) (b)

(c) (d)

Figure 4.26: High frequency synthetic source reconstruction with ten LHS responses, including added noise from 2×10^{12} neutron yield. (a) Detector responses generated from ten LHS IRF matrices, including added noise from 2×10^{12} neutron yield. (b) LSF and NNLSF reconstructions mean (solid lines) with one standard deviation envelope (opaque region). (c) MLE_Gauss and MLE_Poiss reconstructions mean (solid lines) with one standard deviation envelope (opaque region). (d) GEM reconstructions mean (solid line) with one standard deviation envelope (opaque region).

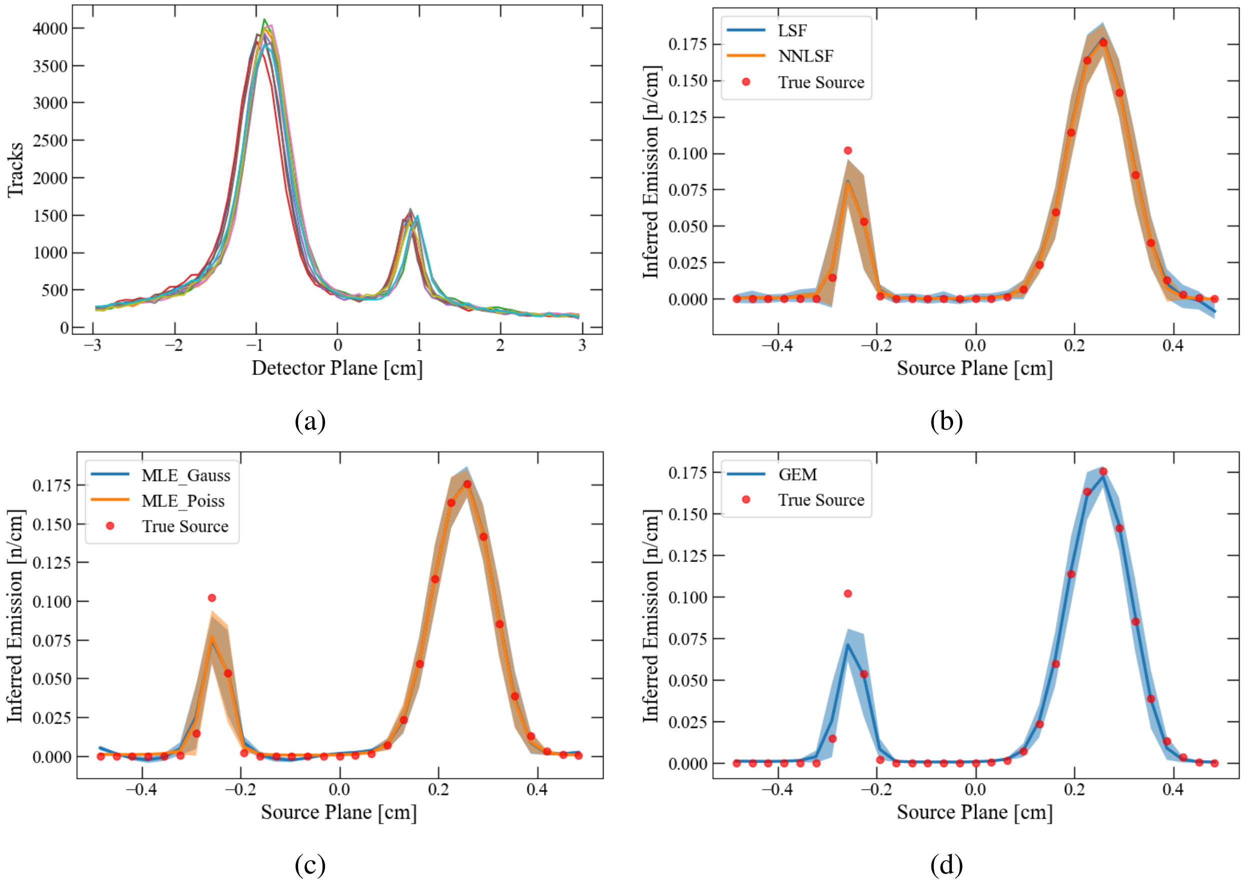

(a) (b) (c) (d)

Figure 4.27: High frequency synthetic source reconstruction with ten LHS responses, including added noise from 1×10^{13} neutron yield. (a) Detector responses generated from ten LHS IRF matrices, including added noise from 1×10^{13} neutron yield. (b) LSF and NNLSF reconstructions mean (solid lines) with one standard deviation envelope (opaque region). (c) MLE_Gauss and MLE_Poiss reconstructions mean (solid lines) with one standard deviation envelope (opaque region). (d) GEM reconstructions mean (solid line) with one standard deviation envelope (opaque region).

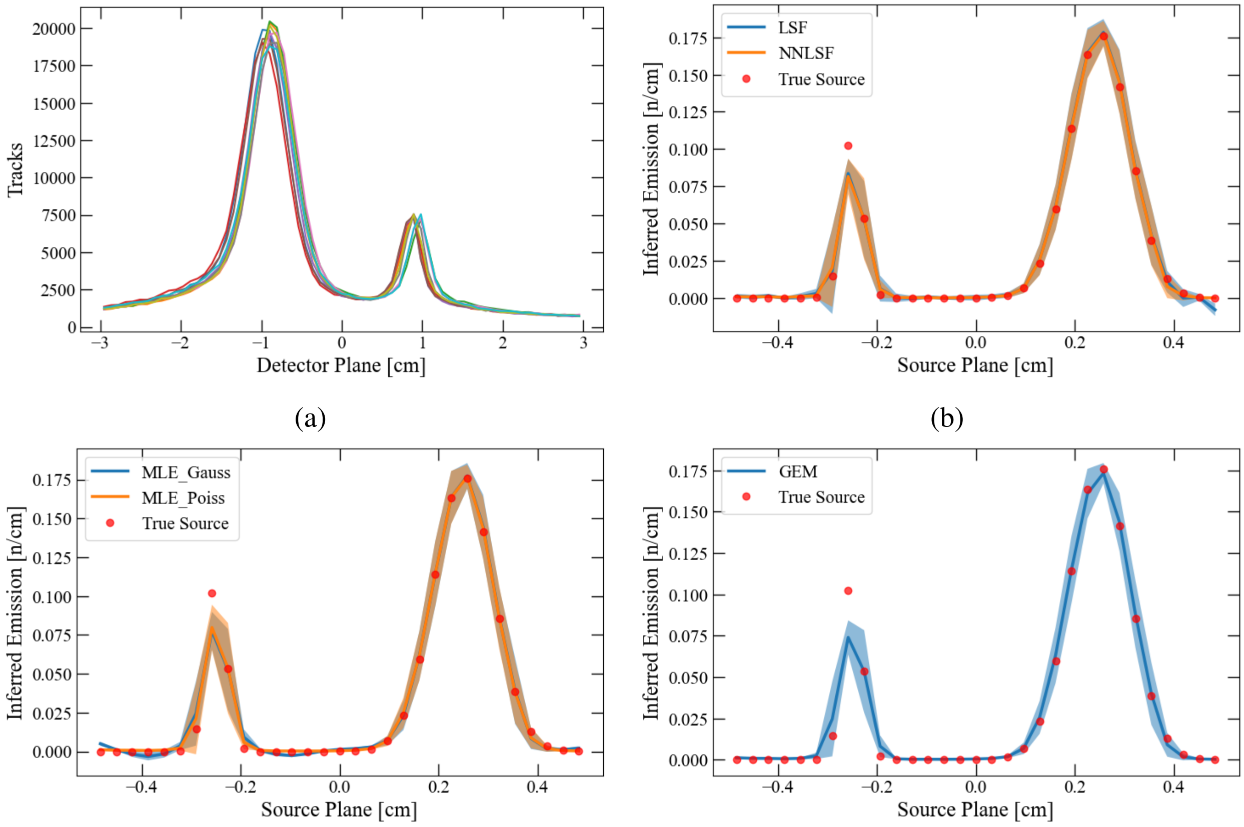

(a) (b)

(c) (d)

Figure 4.28: High frequency synthetic source reconstruction with ten LHS responses, including added noise from 5×10^{13} neutron yield. (a) Detector responses generated from ten LHS IRF matrices, including added noise from 5×10^{13} neutron yield. (b) LSF and NNLSF reconstructions mean (solid lines) with one standard deviation envelope (opaque region). (c) MLE_Gauss and MLE_Poiss reconstructions mean (solid lines) with one standard deviation envelope (opaque region). (d) GEM reconstructions mean (solid line) with one standard deviation envelope (opaque region).

4.2.1.3 Mixed Frequency LHS Reconstructions

Mixed frequency synthetic reconstructions (Figure 4.29, like low frequency reconstructions, have visual asymmetric edge effects due to the signal contribution near the edges of the detector. When noise from increasing neutron yields are introduced (Figures 4.30 to 4.32), variance in reconstructions decrease. This decrease is more discernible in the low frequency portion than that of the high frequency peak, which is in agreement with the previously shown reconstructions.

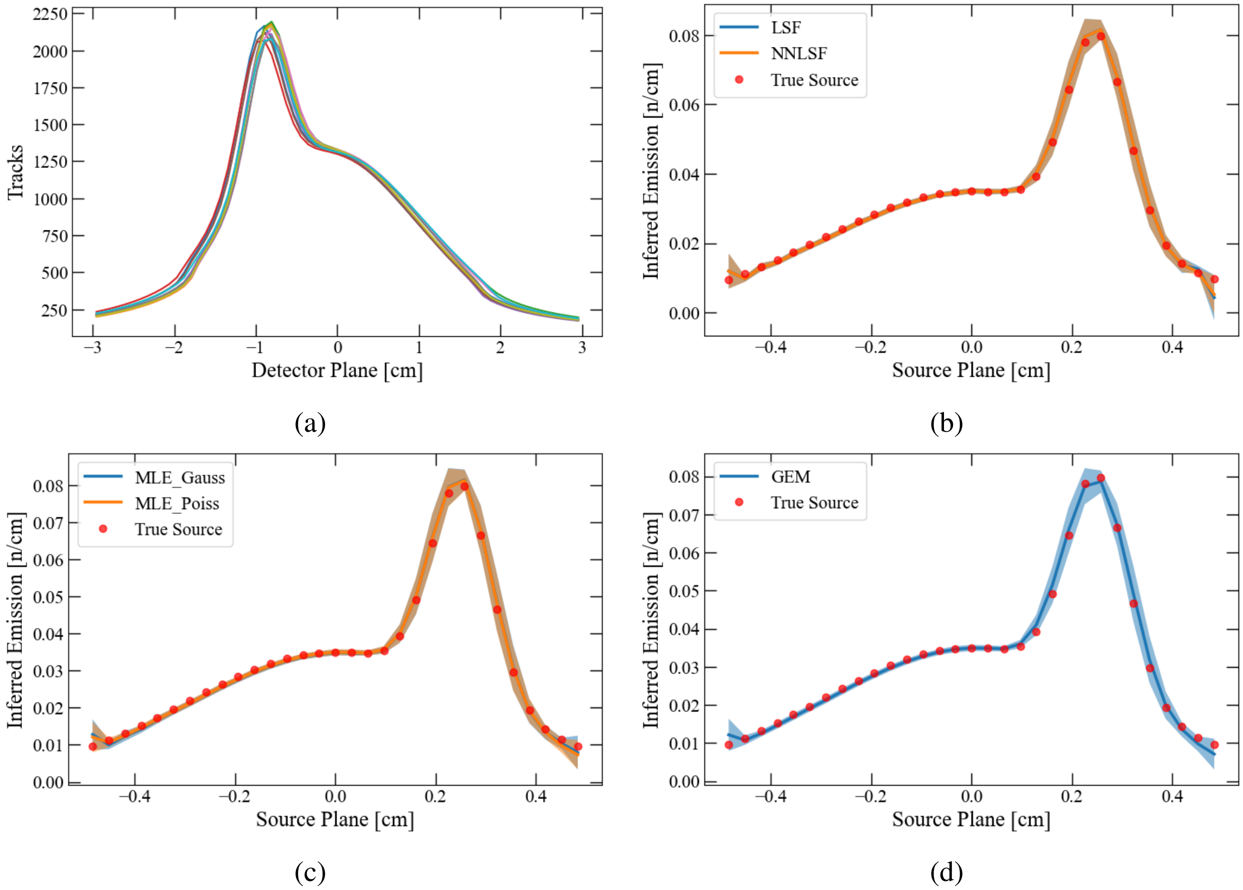

Figure 4.29: Mixed frequency synthetic source reconstruction with ten LHS responses. (a) Detector responses generated from ten LHS noiseless IRF matrices. (b) LSF and NNLSF reconstructions mean (solid lines) with one standard deviation envelope (opaque region). (c) MLE_Gauss and MLE_Poiss reconstructions mean (solid lines) with one standard deviation envelope (opaque region). (d) GEM reconstructions mean (solid line) with one standard deviation envelope (opaque region).

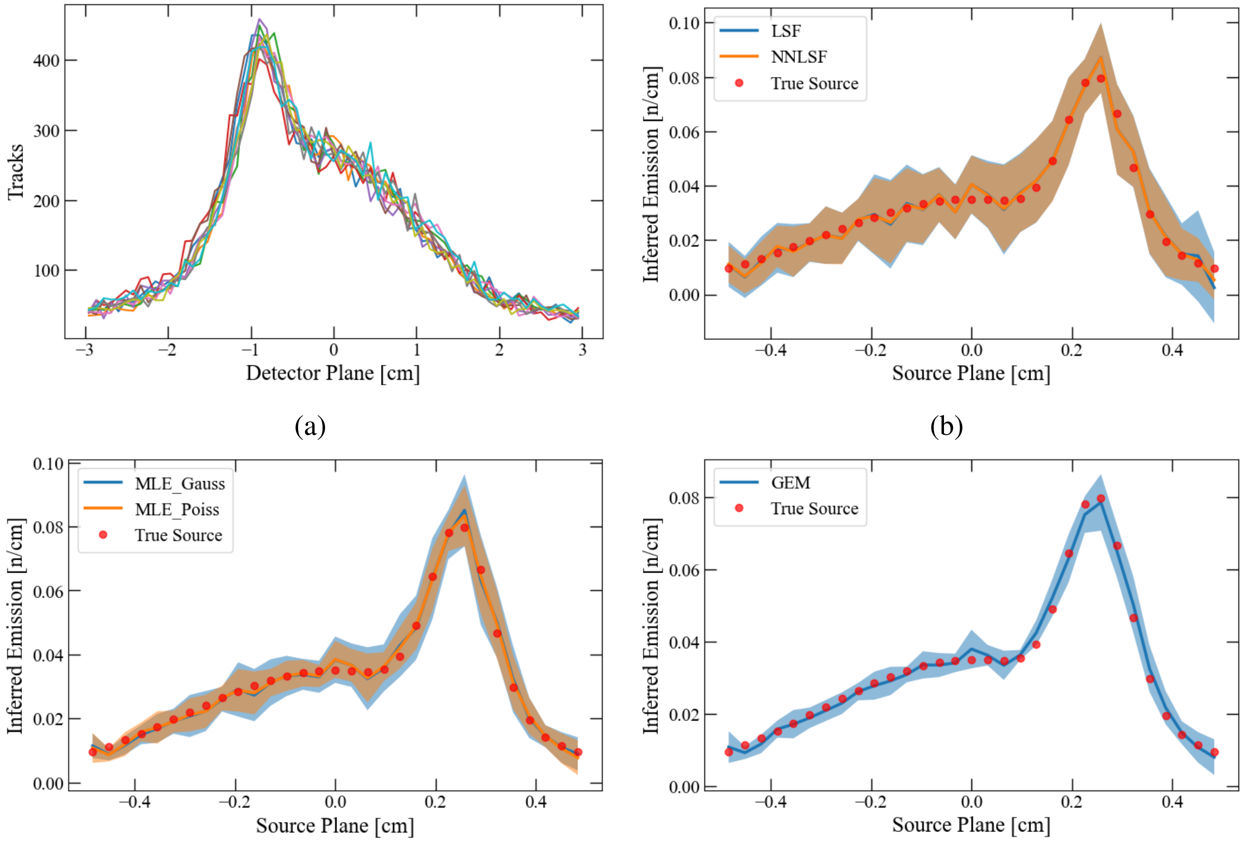

(a) (b)

(c) (d)

Figure 4.30: Mixed frequency synthetic source reconstruction with ten LHS responses, including added noise from 2×10^{12} neutron yield. (a) Detector responses generated from ten LHS IRF matrices, including added noise from 2×10^{12} neutron yield. (b) LSF and NNLSF reconstructions mean (solid lines) with one standard deviation envelope (opaque region). (c) MLE_Gauss and MLE_Poiss reconstructions mean (solid lines) with one standard deviation envelope (opaque region). (d) GEM reconstructions mean (solid line) with one standard deviation envelope (opaque region).

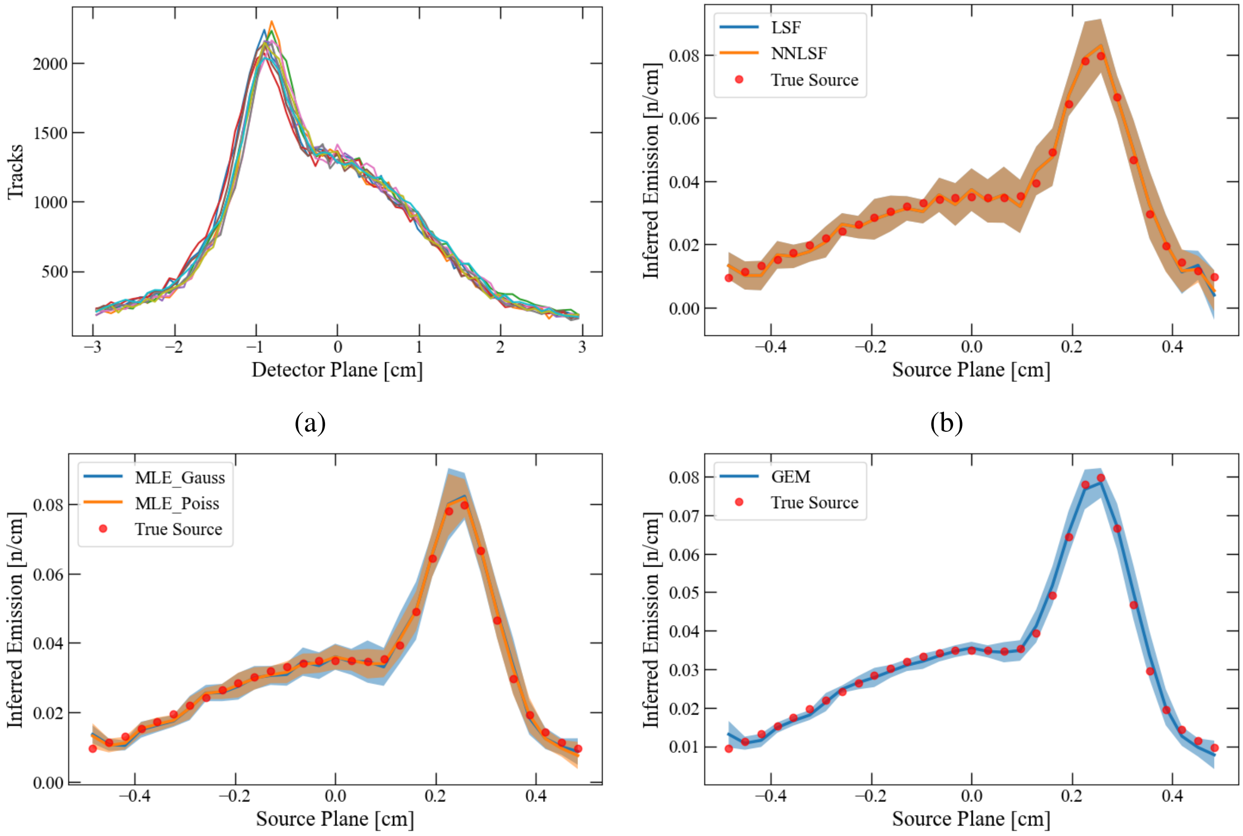

(a) (b)

(c) (d)

Figure 4.31: Mixed frequency synthetic source reconstruction with ten LHS responses, including added noise from 1×10^{13} neutron yield. (a) Detector responses generated from ten LHS IRF matrices, including added noise from 1×10^{13} neutron yield. (b) LSF and NNLSF reconstructions mean (solid lines) with one standard deviation envelope (opaque region). (c) MLE_Gauss and MLE_Poiss reconstructions mean (solid lines) with one standard deviation envelope (opaque region). (d) GEM reconstructions mean (solid line) with one standard deviation envelope (opaque region).

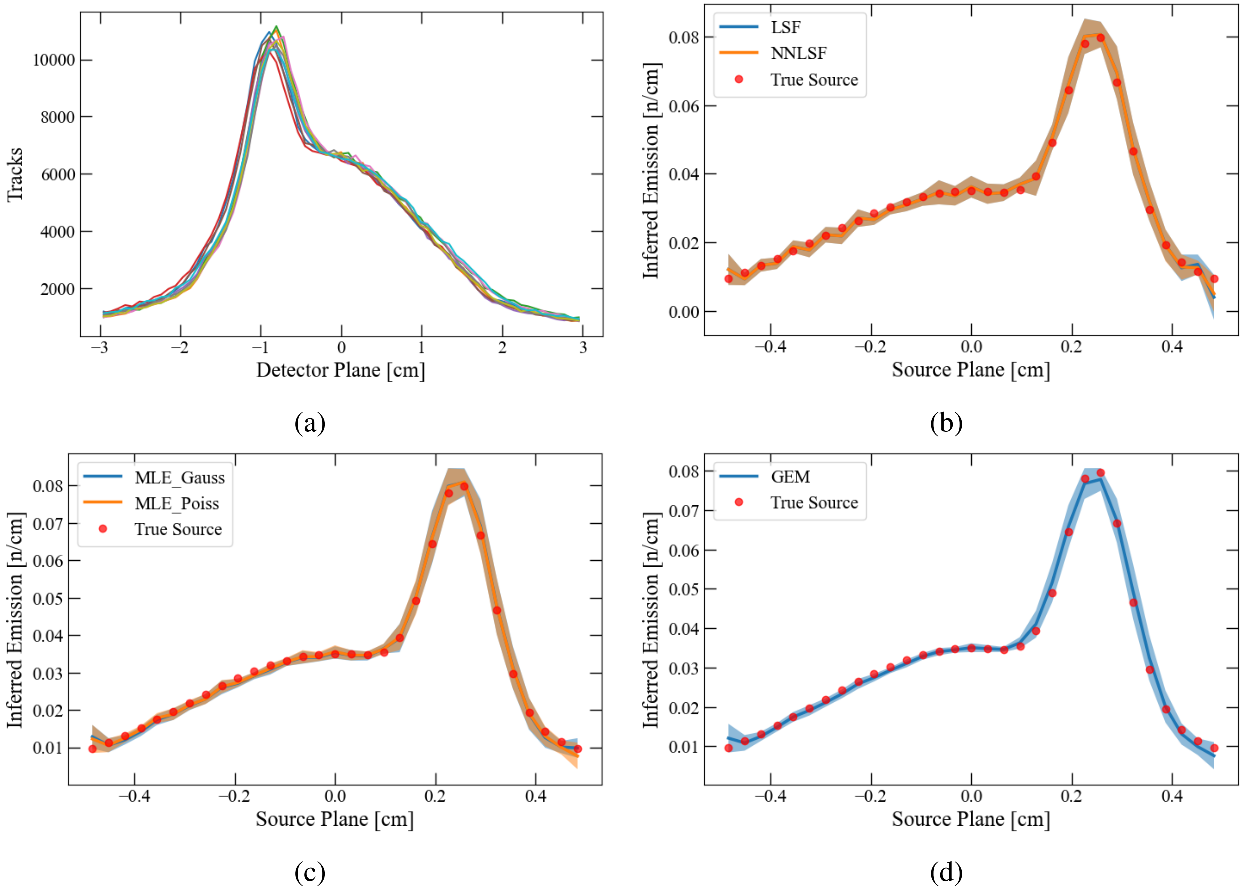

Figure 4.32: Mixed frequency synthetic source reconstruction with ten LHS responses, including added noise from 5×10^{13} neutron yield. (a) Detector responses generated from ten LHS IRF matrices, including added noise from 5×10^{13} neutron yield. (b) LSF and NNLSF reconstructions mean (solid lines) with one standard deviation envelope (opaque region). (c) MLE_Gauss and MLE_Poiss reconstructions mean (solid lines) with one standard deviation envelope (opaque region). (d) GEM reconstructions mean (solid line) with one standard deviation envelope (opaque region).

4.2.2 Data Bootstrapping

While the LHS method propagates the uncertainty of each parameter, the parameter space is not accurately measured, and it is a slow an computationally expensive process. An alternative approach to estimate the uncertainty in reconstructions is bootstrapping [37, 39, 40]. This method can use a single CR-39 dataset's statistics and generate new "bootstrapped" data.

As shown in the previous section, noise has a dominant effect on reconstructions, especially in data with lower counts. The central limit theorem states that the sampling distribution of a mean is normal, so long as the sample size is large enough [41]. Our CR-39 track generation is believed to be a dominantly Poissonian process, and Poissonian distributions approach a normal distribution as count rates increase [42]. These two statements allow us to approximate noise variations by sampling from the row mean and standard deviation of a 2-D dataset. This sampling space can be used similarly to the generation of 2-D synthetic data, where each sample makes up a column in a bootstrapped 2-D dataset. From a single experimental dataset, the calculated row mean and standard deviation may not be the true distribution. However, accuracy will increase with the increase in neutron yield.

Repeating this process n times allow for n source reconstructions to generate a solution mean and standard deviation. Bootstrapping was performed for a single low frequency, high frequency and mixed frequency detector response. The original detector was generated with Poissonian sampling with a neutron yield of 1×10^{13}, as described in Section 4.1.1. Reconstructions from n = 100 bootstrapped samples are shown in Figures 4.33 to 4.35.

It can be seen across the low frequency source, and mixed frequency source, that the error estimation is subject to the original Poissonian noise distribution. With the exclusion of high frequency solutions, LSF, NNLSF, MLE_Gauss and MLE_Gauss have noisy reconstructions which do not capture every point within one standard deviation. GEM solutions across each source has the smoothest solution and lowest standard deviation. The issue of under-predicting peaks continues to be an issue, but the structure of GEM solutions appear to be the most promising of all the reconstruction methods.

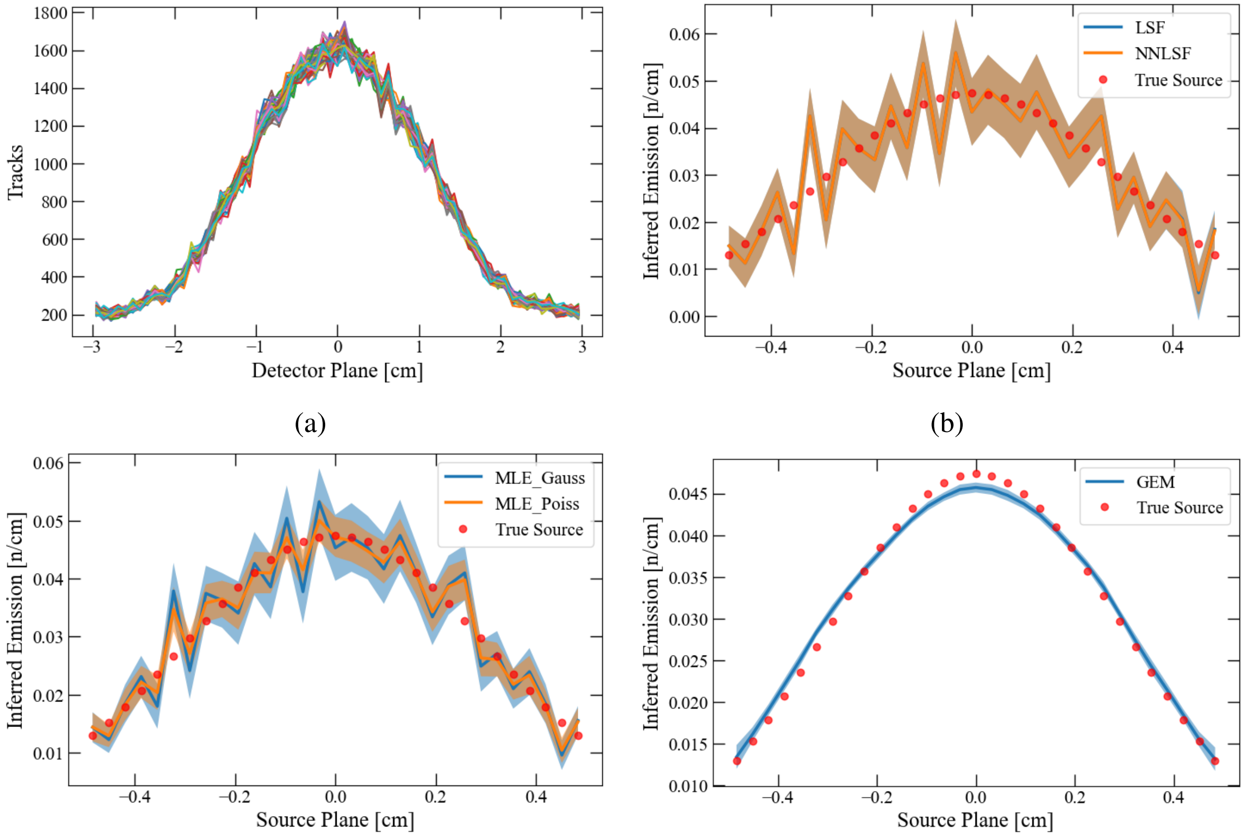

(a) (b)

(c) (d)

Figure 4.33: Low frequency synthetic source reconstruction from n = 100 bootstrapped samples. (a) Bootstrapped detector responses generated from a single Poissonian detector response. (b) LSF and NNLSF reconstructions mean (solid lines) with one standard deviation envelope (opaque region). (c) MLE_Gauss and MLE_Poiss reconstructions mean (solid lines) with one standard deviation envelope (opaque region). (d) GEM reconstructions mean (solid line) with one standard deviation envelope (opaque region).

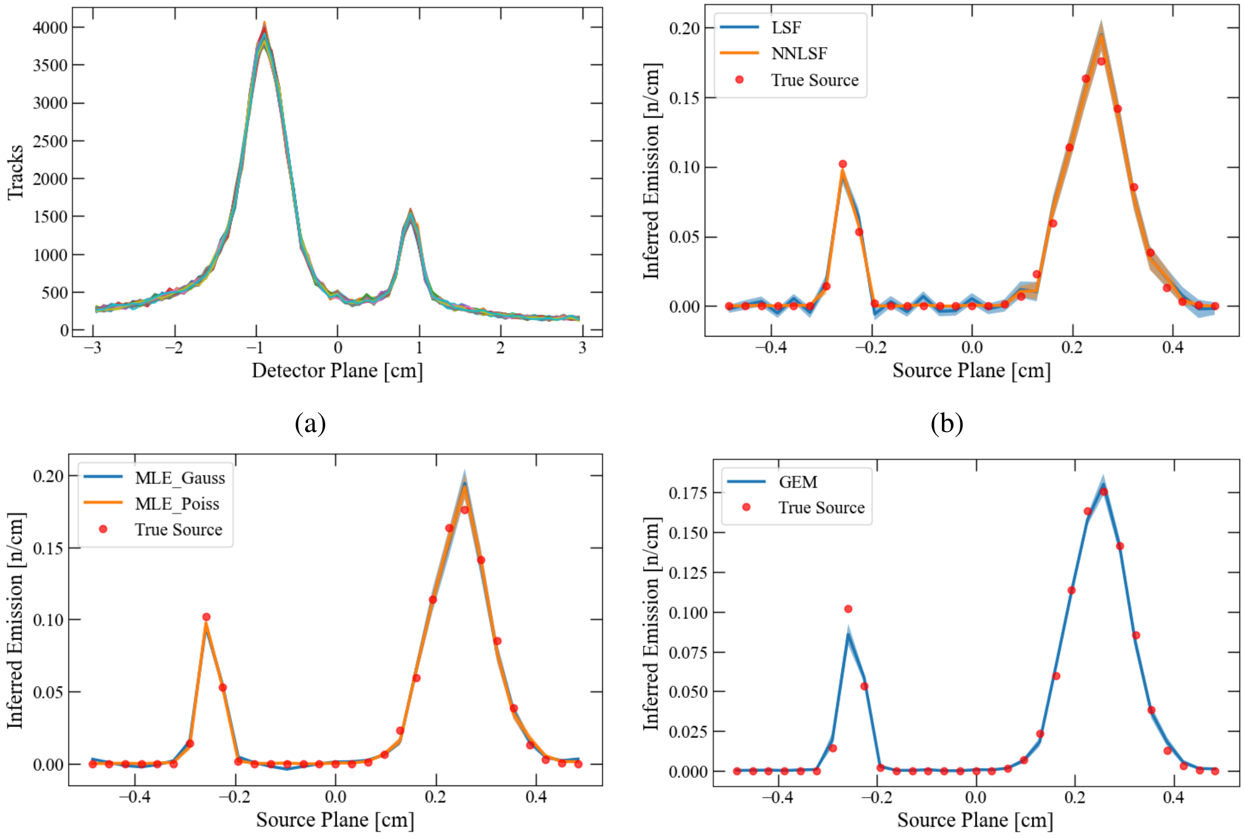

(a) (b)

(c) (d)

Figure 4.34: High frequency synthetic source reconstruction from n = 100 bootstrapped samples. (a) Bootstrapped detector responses generated from a single Poissonian detector response. (b) LSF and NNLSF reconstructions mean (solid lines) with one standard deviation envelope (opaque region). (c) MLE_Gauss and MLE_Poiss reconstructions mean (solid lines) with one standard deviation envelope (opaque region). (d) GEM reconstructions mean (solid line) with one standard deviation envelope (opaque region).

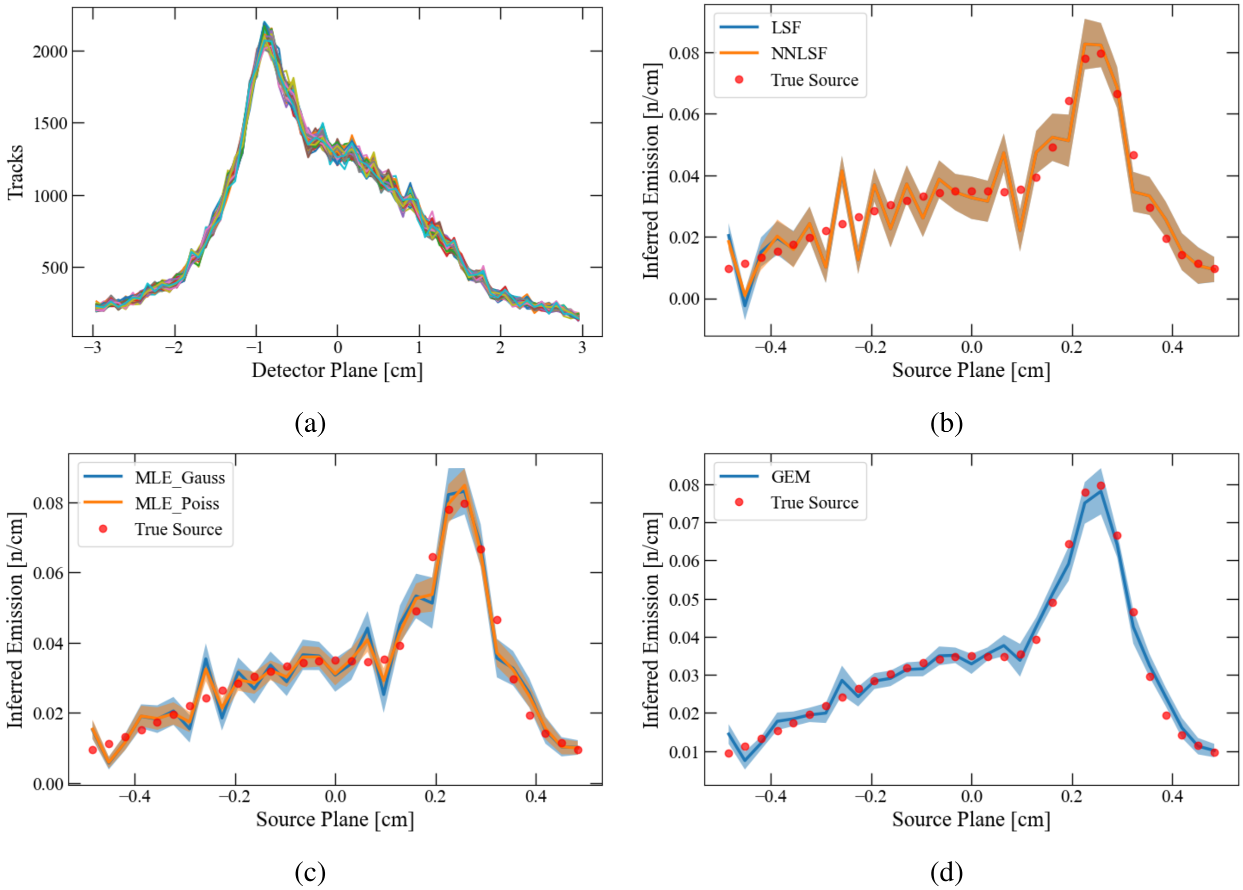

(a) (b)

(c) (d)

Figure 4.35: Mixed frequency synthetic source reconstruction from n = 100 bootstrapped samples. (a) Bootstrapped detector responses generated from a single Poissonian detector response. (b) LSF and NNLSF reconstructions mean (solid lines) with one standard deviation envelope (opaque region). (c) MLE_Gauss and MLE_Poiss reconstructions mean (solid lines) with one standard deviation envelope (opaque region). (d) GEM reconstructions mean (solid line) with one standard deviation envelope (opaque region).

5. SOURCE RECONSTRUCTION FROM ODIN DATA

Source reconstruction was performed on two of the highest performing MagLIF experiments to date, z3289[1] and z3926. At the start of this research, z3289 had the highest primary DD yield of 1.1×10^{13}. At the time of writing, z3926 had the highest yield recorded to date at 1.9×10^{13}. These experiments provided a SNR adequate for reconstructions with a single CR-39 scan. By first performing reconstructions on a single dataset, algorithm performance and results provide intuition on how to approach using data from multiple scans of CR-39 from the same experiment. As previously stated in Chapter 4, statistical noise is likely to be the largest source of uncertainty. Therefore, the The MLE_Gauss, MLE_Poiss, and GEM methods would be used for experimental reconstructions.

This chapter introduces the experimental data and source reconstructions using each algorithm. Initial results produced solutions believed to be non-physical due to an unknown background, and a modified GEM algorithm was implemented to produce more accurate results. Reconstructions were validated by comparing the neutron emission profile to an x-ray emission profile provided by a time-integrated pinhole camera (TIPC) [44,45]. Next, a 2-D k-fold method was implemented for determining the optimal β parameter in order to produce more consistent reconstructions. Finally, bootstrapping was performed to estimate a range of uncertainty in the reconstructions.

5.1 CR-39 Data

For the following reconstructions, data from the back face of the first piece of CR-39 in the detector package was used. The tracks on the back face are dominantly generated by protons produced within the CR-39 itself. Along the front face, protons are primarily generated by recoil protons induced by the HDPE converter foil, but also from protons in the CR-39. Discrimination settings for the back face are better constrained due to the single process generating tracks. The front face discrimination settings are more challenging to determine, and often produce a fewer

---

[1] Preliminary methodology and results shown here were previously published in [43].

number of tracks than the back face.

The discrimination settings used for the following datasets were: track diameter upper limit of 100 μm, eccentricity upper limit of 10, and contrast upper limit of 10. Here, the contrast is calculated by the average pixel brightness within the darkened track area, divided by the median pixel brightness of the surrounding area, then multiplied by 100. This means the lowest contrast values correspond to the darkest tracks. As previously shown in section 1.3.3, the CR-39 scans need to be trimmed to eliminate the drop in signal near the alignment pinholes. Scans from more recent experiments use an alignment tray which use pins to align each piece. This removes the possibility of scans to be slightly rotated from one another, with the sacrifice of a larger area needing to be removed when cutting the 2-D data.

Figure 5.1 shows the binned 2-D data, and the cut 2-D data for z3289 and z3926. Each of these scans are the back face of the CR-39 piece closet to the source, with a resolution of 900 μm. Dimensions of each cut 2-D data differ, with z3289 being 58x57 pixels and z3926 being 50x56 pixels. The detection region differs between the two, and each 1-D axial profile is shown in Figure 5.2. 1-D data from z3289 appears to have a distinct high frequency peak near -0.25 cm, where z3926 has less prominent high frequency features. The distinct peak would indicate there is a possible hot spot in the solution for z3289, whereas z3926 would have a more evenly spread distribution.

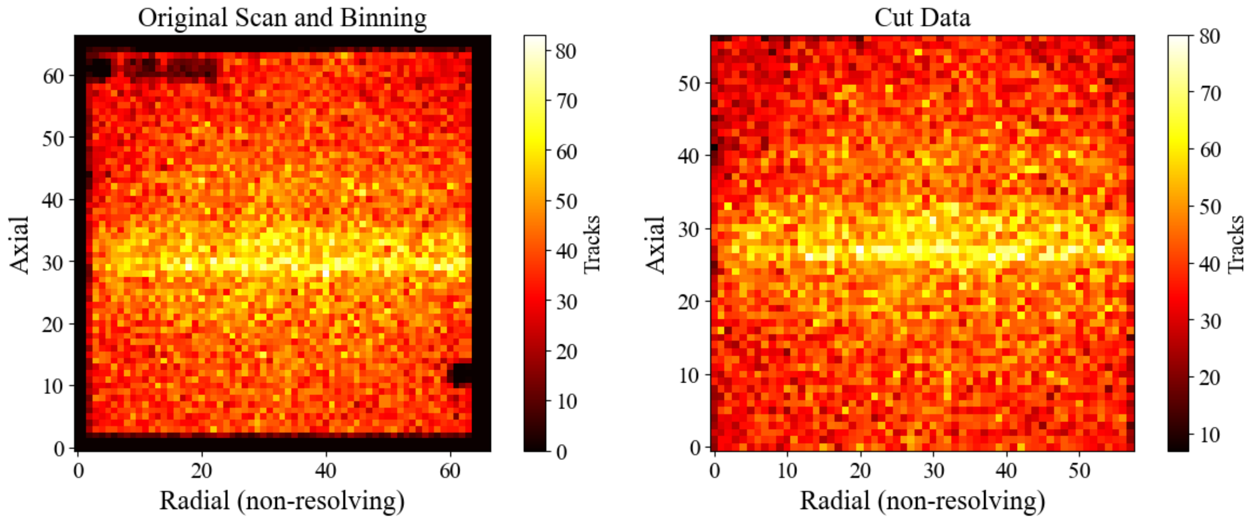

(a) z3289 (b) z3289

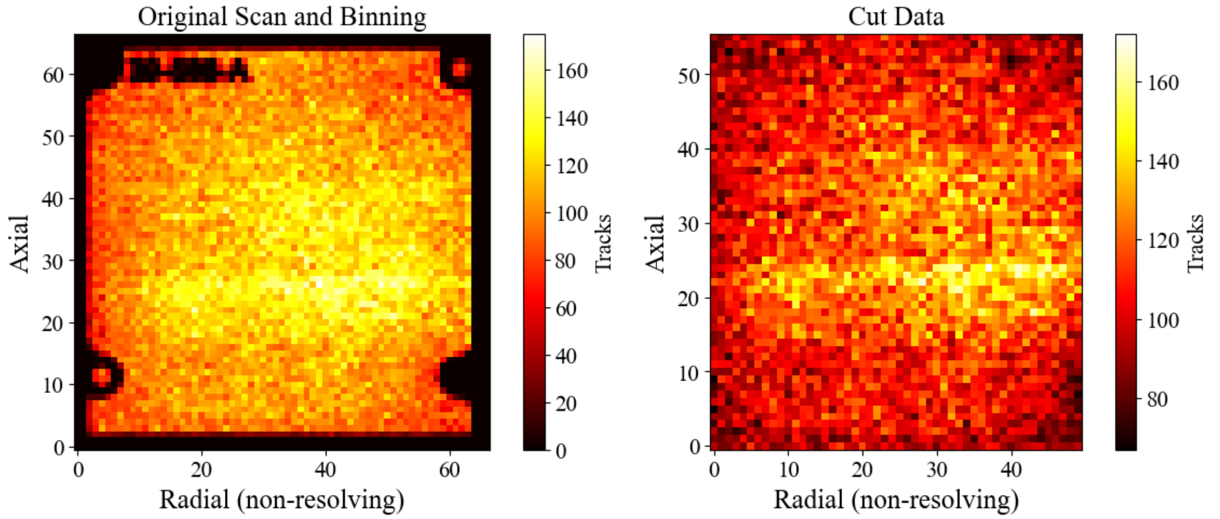

(c) z3926 (d) z3926

Figure 5.1: Discriminated and binned CR-39 track data for (a) z3289 including pinholes and serial number, (b) z3289 subset to remove pinholes and serial number, (c) z3926 including pinholes and serial number, (d) z3926 subset to remove pinholes and serial number.

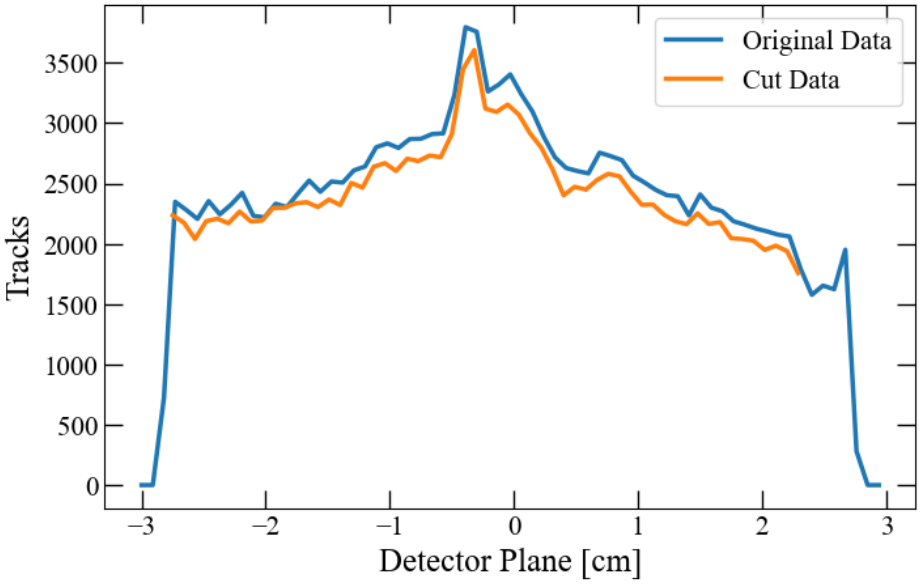

(a) z3289

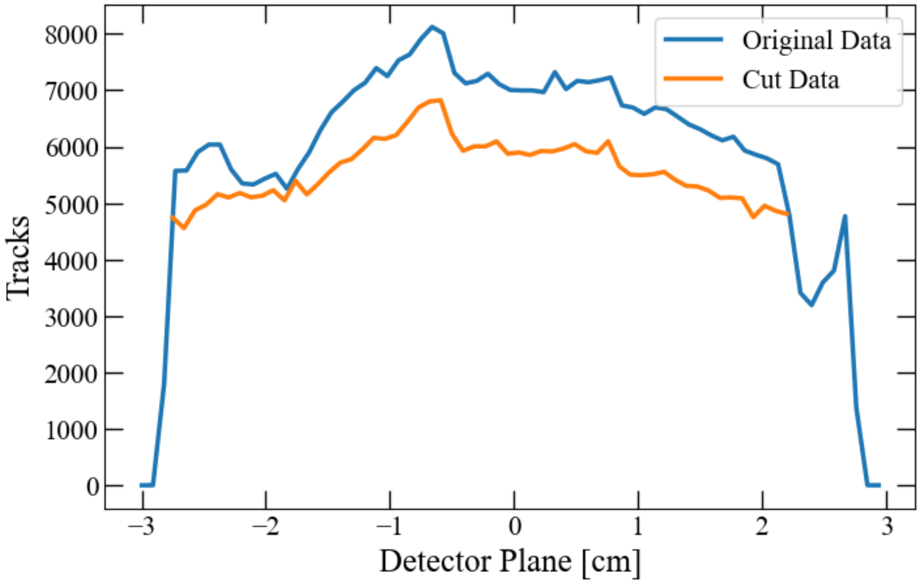

(b) z3926

Figure 5.2: Integrated axial track data for binned original (blue solid) and cut (orange solid) data from (a) z3289 and (b) z3926.

5.2 Issues of Background

The MLE_Gauss, MLE_Poiss, and GEM methods were used for source reconstruction on 1-D axial detector data from experiment z3289 shown in Figure 5.3. A 57 x 31 IRF matrix was used for reconstructions, this corresponds to a source resolution of $\sim$322 μm. Results from the k-fold cross validation in Figure 5.3 (a) determined $\beta = 1000$ was optimal, though the training and validation curves appear to be inconsistent. The recovered source profiles for each method are shown in Figure 5.3 (c). Profiles for MLE_Gauss and MLE_Poiss each contain only positive values with MLE_Gauss having more prominent features in the interior of the source. The GEM algorithm with β = 1000 forms a solution that matches the MLE_Poiss reconstruction. These observations are consistent with the trends present in synthetic reconstructions from Chapters 3 and 4. However, each reconstruction has large edge effects present in the solutions.

As previously shown in Chapter 4, edge effects in solutions are produced by IRFs being unable to produce an accurate fit to data near the edges of the detection region. This is confirmed to be the case as seen in Figure 5.3 (b) when forward fits for each algorithm are compared to the experimental data. The edge peaks are much larger in amplitude compared to the central source contributions, indicating that the effects are more significant than those observed in the sensitivity analysis. In addition, the edge effects are seen at both ends of the source profile. This indicates that an alignment issue is likely not the cause, as the most sensitive parameters produce asymmetric effects, leading to only one source extreme to be affected.

From these observations, it is believed that these edge peaks are non-physical artifacts caused by a background on the CR-39 which was not being accounted for in the reconstruction. Figure 5.4 shows the source reconstruction and forward fits of a mixed frequency synthetic source when a constant uniform background was added to the detector response data. This added background reproduced similar edge effects seen in Figure 5.3. In CR-39, there is an inherent background on the plastic itself caused by dust, debris, or defections of any kind which are collected during the microscopic scanning process. Ordinarily, a background subtraction could be performed, however, measuring the background directly for each piece of CR-39 is challenging. Previously shown in

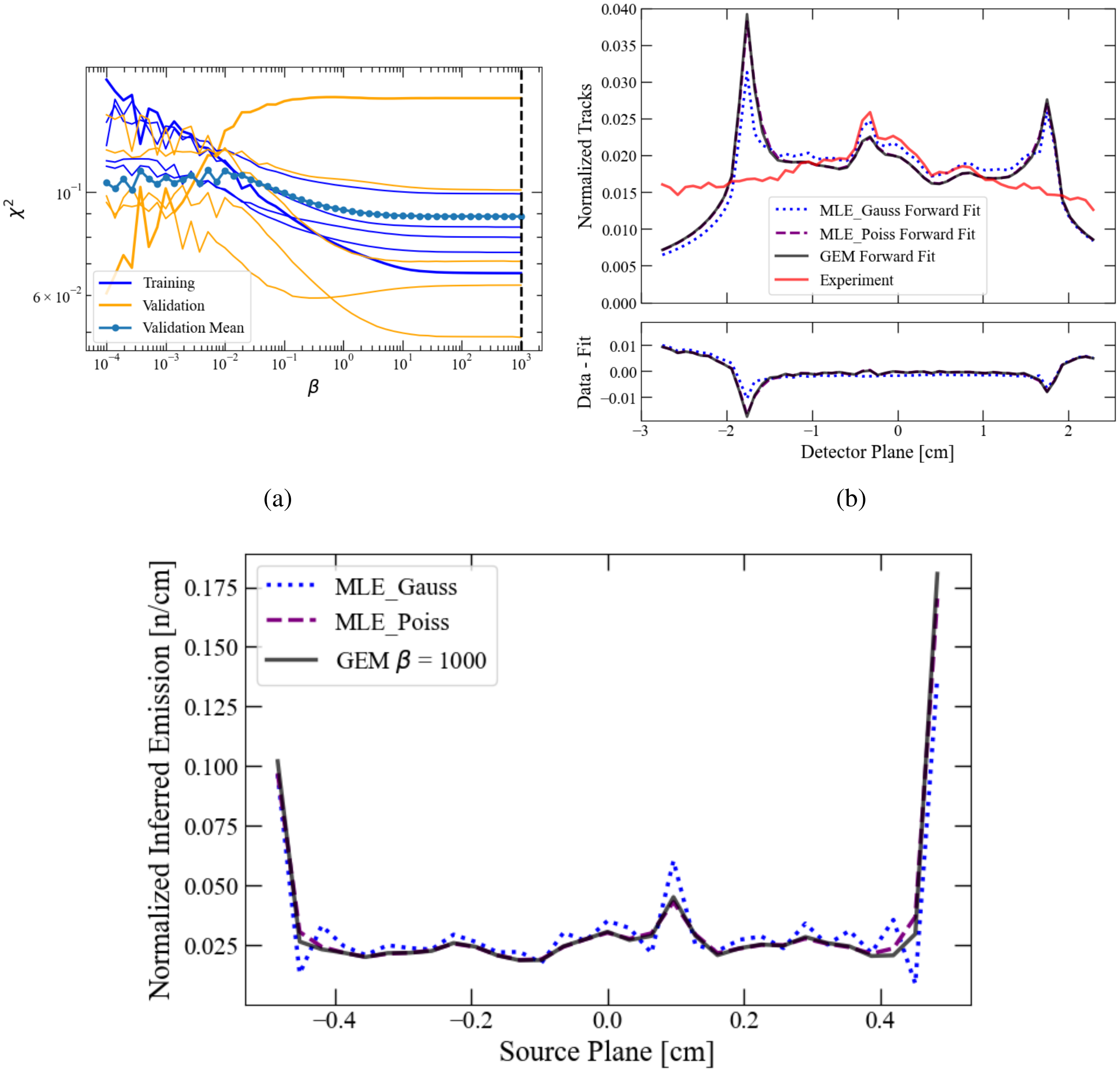

(a)

(b)

(c)

Figure 5.3: Image reconstruction for z3289. (a) k-fold cross validation results indicating optimal $\beta = 1000$. (b) MLE_Gauss, MLE_Poiss, and GEM forward fits compared to experimental data and corresponding residuals. (c) MLE_Gauss, MLE_Poiss, and GEM source reconstructions. The large edge effects seen in the reconstructions are believed the be non-physical artifacts.

Figures 2.1 and 2.2, neutron emission from anywhere along the source reaches the entire CR-39 area. Therefore, tracks generated in the experiment are produced along all regions of the CR-39, leaving no area to be measured exclusively as background.

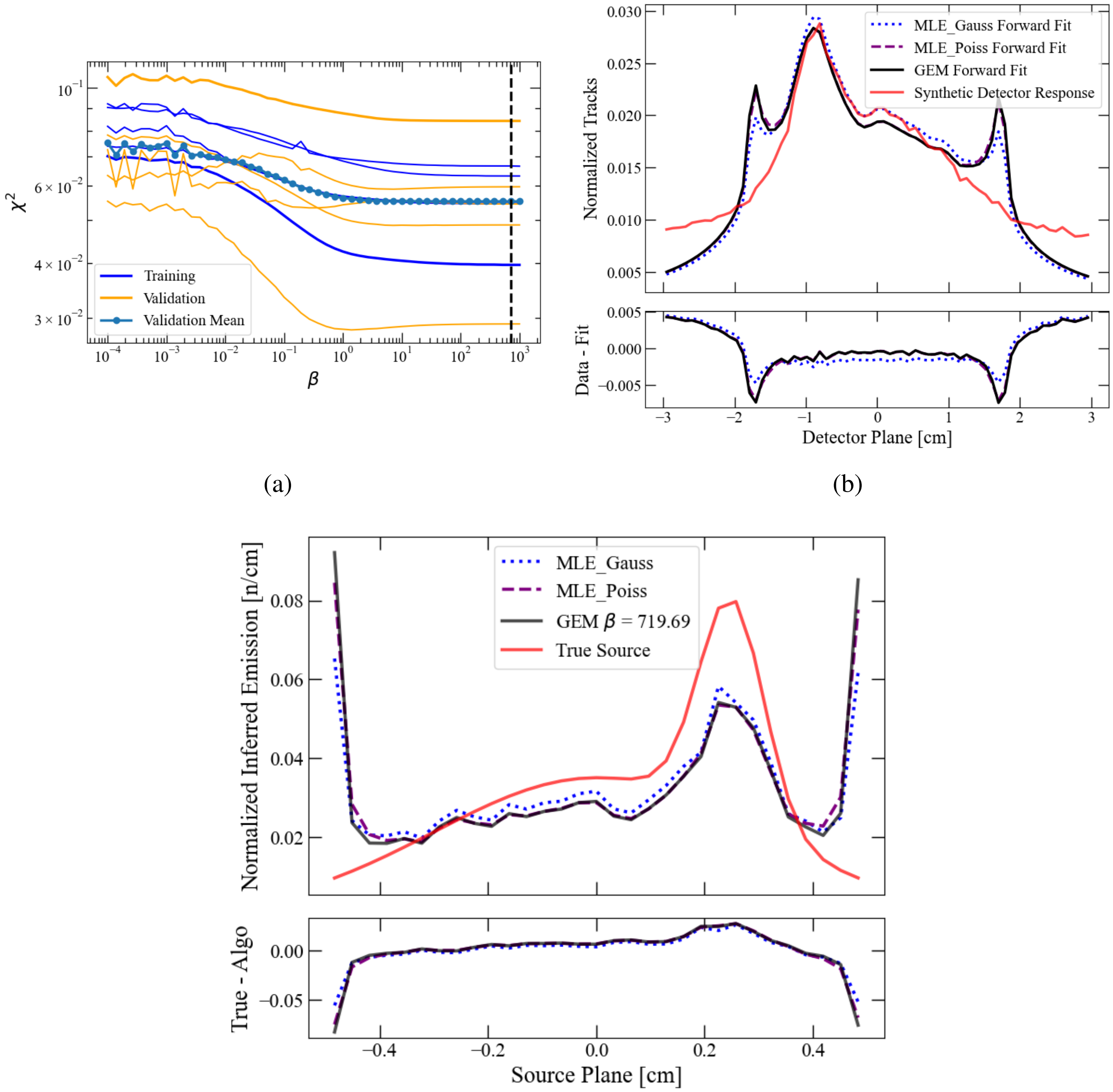

(a) (b)

(c)

Figure 5.4: Image reconstruction of a mixed frequency synthetic detector response with an added uniform background. (a) k-fold cross validation results indicating optimal $\beta = 26.83$. (b) MLE_Gauss, MLE_Poiss, and GEM forward fits compared to experimental data and corresponding residuals. (c) MLE_Gauss, MLE_Poiss, and GEM source reconstructions. The large edge effects seen in Figure 5.3 (c) are reproducible with the added uniform background.

5.3 Modified GEM Method

To account for an unknown background in the CR-39 data, the GEM algorithm was modified to add basis functions which attempt to fit the unknown background. These basis functions, B_{iv}, act as additional response functions corresponding to coefficients, μ_v. All terms are held to positive values in order to be consistent with the EM algorithm. The matrix form of adding the background basis functions and their respective coefficients is represented as

$$[P, B] \begin{bmatrix} G \\ \\ \mu \end{bmatrix} = Y. \tag{5.1}$$

This equation can be solved for the source reconstruction and background coefficients directly by applying a LSF if desired.

To alter the GEM method, Eq. 3.16 has the background basis functions and coefficients added to the denominator:

$$b_j^{(t)} = \sum_i \frac{y_i P_{ij} g_j^{(t)}}{\sum\limits_q P_{iq} g_q^{(t)} + \sum\limits_v B_{iv} \mu_v^{(t)}}. \tag{5.2}$$

The iteration steps to solve for $g_j^{(t+1)}$ remain unchanged, however, μ values must be updated at every step as well with

$$\mu_v^{(t+1)} = \frac{\mu_v^{(t)}}{\sum\limits_i B_{iv}} \frac{y_i}{\sum\limits_q P_{iq} g_q^{(t)} + \sum\limits_v B_{iv} \mu_v^{(t)}}. \tag{5.3}$$

For our data, a flat constant, and two linear backgrounds (ascending and descending) were used as the background basis functions. The initial value set for each background coefficient was 0.01. In order for the background coefficients to reach an equilibrium of source to background contribution, a higher number of iterations were needed. Therefore, a value of 10^{-5} was used as a stopping criterion, with the variation of chi-squared and absolute difference of all background coefficients needing to be below this threshold. The modified algorithm is referred to as GEM_BG, and was successful at accounting for the background in synthetic problems. Figure 5.5 shows the GEM_BG $k-$fold cross validation results, forward fit, and source reconstruction for a mixed frequency synthetic source when a constant uniform background was added to the detector response data. The edge effects previously seen in Figure 5.4 have been removed in the forward fit and source profile. Similar results were produced with the low and high frequency synthetic sources, as well as when adding slanted backgrounds to the detector response data.

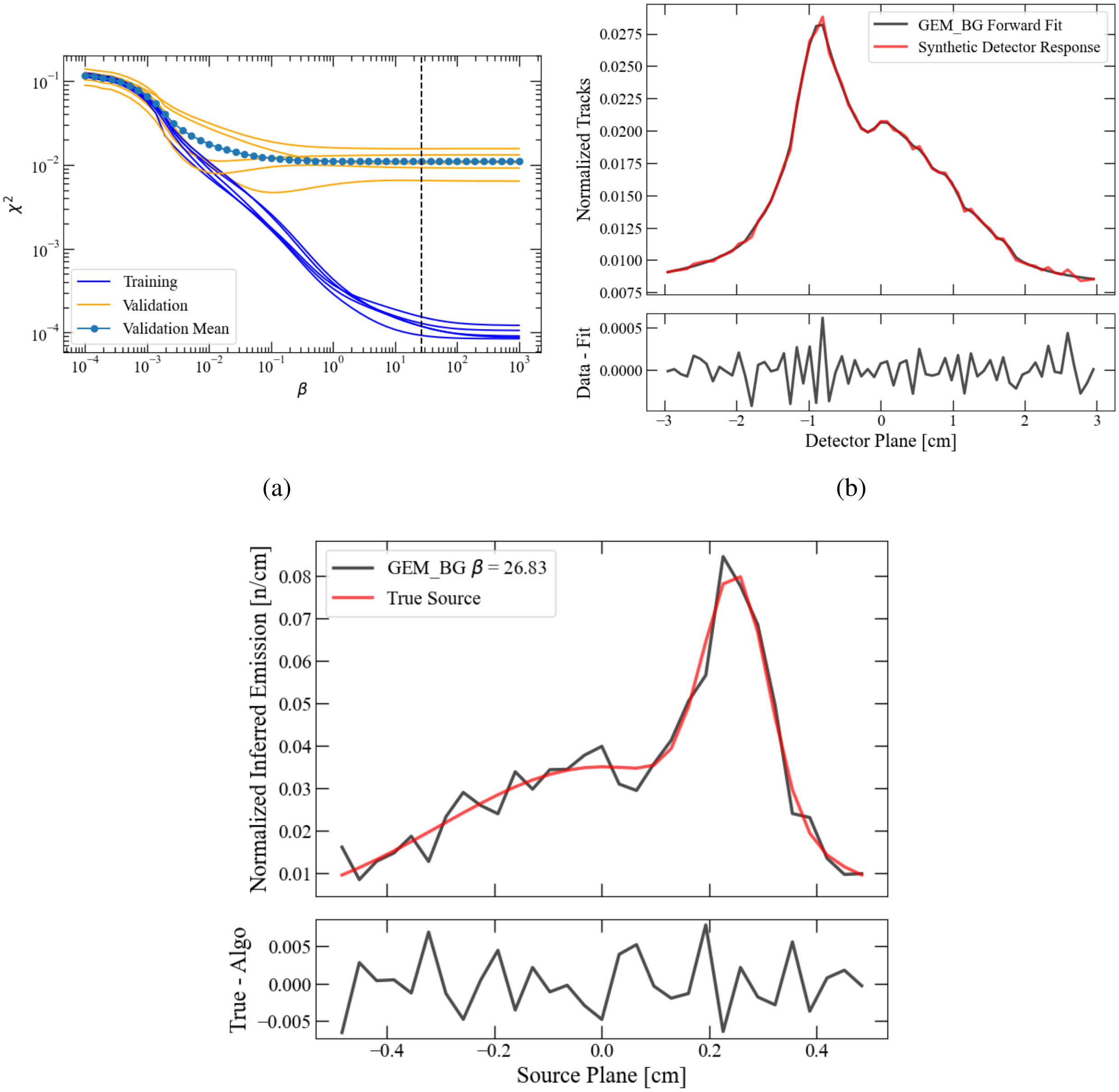

(a)

(b)

(c)

Figure 5.5: GEM_BG image reconstruction of a mixed frequency synthetic detector response with an added uniform background. (a) k-fold cross validation results indicating optimal $\beta = 719.69$. (b) GEM_BG forward fit compared to experimental data and corresponding residual. (c) GEM_BG source reconstruction. The addition of basis response functions has successfully removed the large edge effects from Figure 5.4 caused by an added uniform background.

5.3.1 Modified GEM Experimental Results

The modified GEM method was applied to the data from z3289 and z3926. Figure 5.6 (a) shows the training, validation, and validation mean curves for z3289, resulting in an optimal β value of 1000, indication no smoothing for the solution. The forward fit and residual of the GEM_BG method (black solid) compared to experimental data (red solid) is shown in Figure 5.6 (b) with the same y-axes as Figure 5.3 (b). Figure 5.6 (c) shows the peak normalized GEM_BG solution for $\beta = 1000$ (black solid). Clearly, the forward fit is greatly improved by the modified method, and the large edge effects have been reduced.

Included in Figure 5.6 (c) is a peak normalized x-ray emission profile from a multi-channel time-integrated pinhole camera (TIPC) diagnostic (red dashed) fielded on z3289. TIPC is comprised of five pinholes with a spatial resolution of $<\sim$200 μm all pointed at the same target location, and an image plate to record the five separate images. A spatial resolution of this size is adequate to resolve axial variations in the plasma, but not radial variations as the width of the column is $<$ $\sim$100 μm. Therefore, TIPC can be a useful 1-D imager when integrating the data across the radial axis, as done with ODIN data.

Varying TIPC spectral responses can be acquired by applying different filters to each pinhole. The TIPC data shown in Figure 5.6 (c) was filtered with 1.5 mm of Kapton tape, which has low transmission below $\sim$10 keV x-rays. There may be reasonable surrogacy between this TIPC x-ray image and ODIN source reconstruction because variations in the areal density of the beryllium liner will result in relatively minor variations in the TIPC image, as x-rays of $>\sim$10 keV are less likely to be attenuated. However, TIPC and ODIN are not co-registered in experimental setup, so the max peaks of the ODIN reconstruction and TIPC data have been registered near 0.1 cm. It can be seen that the two profiles show significant quantitative agreement with one another. Possible sources of differences in the features are the liner areal density attenuation and noise in the data.

The GEM_BG method was repeated with data from z3926 and is shown in Figure 5.7. An optimal β value of 0.01 was determined, which significantly smoothed the forward fit and solution shown in Figure 5.7 (b) and 5.7 (c), respectively. Residuals of GEM_BG solutions significantly

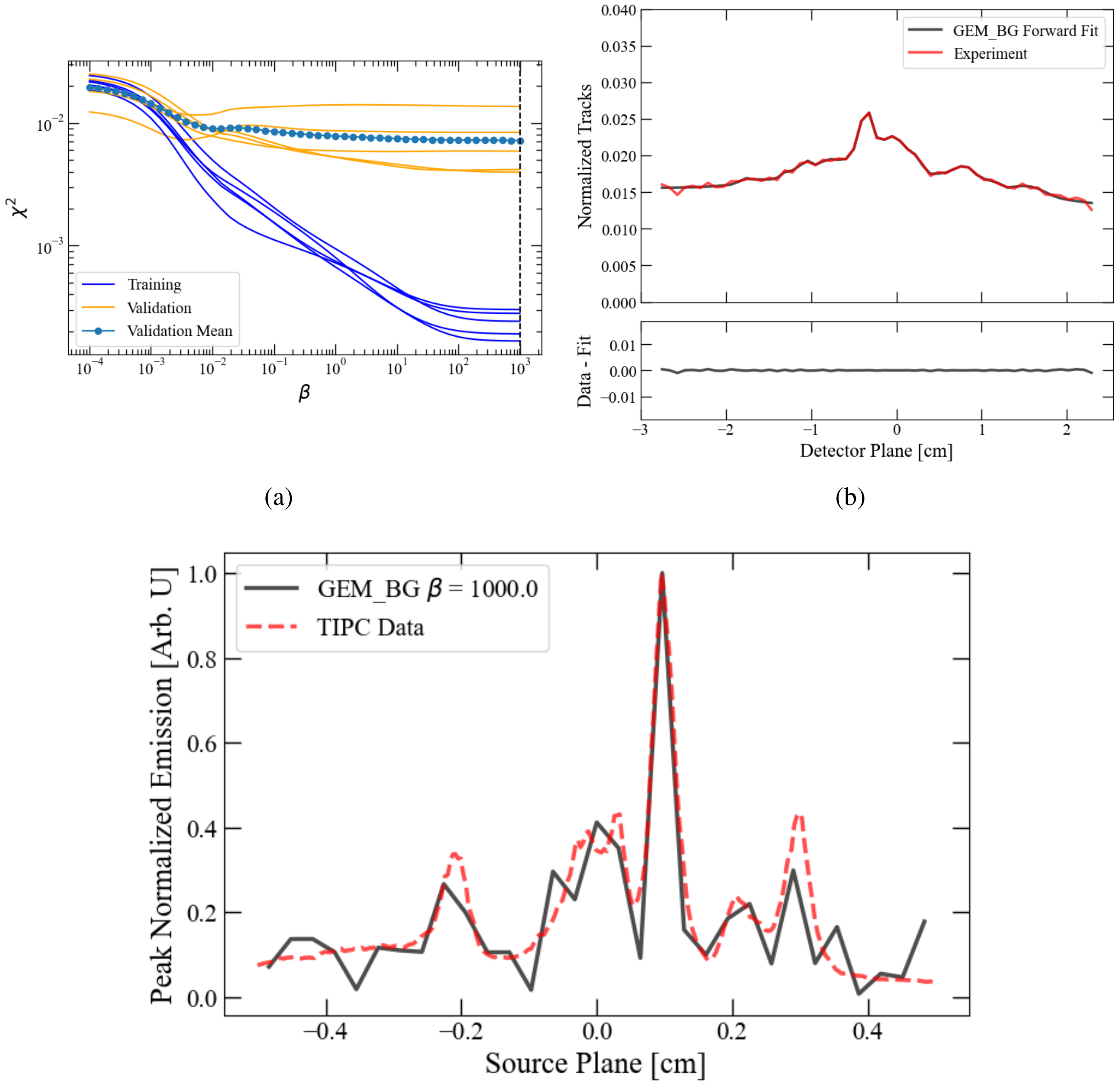

(a)

(b)

(c)

Figure 5.6: GEM_BG image reconstruction of z3289. (a) k-fold cross validation results indicating optimal $\beta = 1000$. (b) GEM_BG forward fit compared to experimental data and corresponding residual. (c) Peak normalized GEM_BG source reconstruction registered with peak normalized TIPC data indicating quantitative agreement.

increased, and appear to peak near -0.75 cm where the experimental data peak is occurring. The TIPC data shows distinct features along the axial extent of the source, but the ODIN reconstruction produced a smooth solution matching the general profile of the entire source extent. When repeating the k-fold cross validation with different permutations of random data points in each fold, β values $<\sim 1$ were determined to be optimal and consistently produced over-smoothed solutions. At this point, it was hypothesized that there is likely an issue in β parameter selection method.

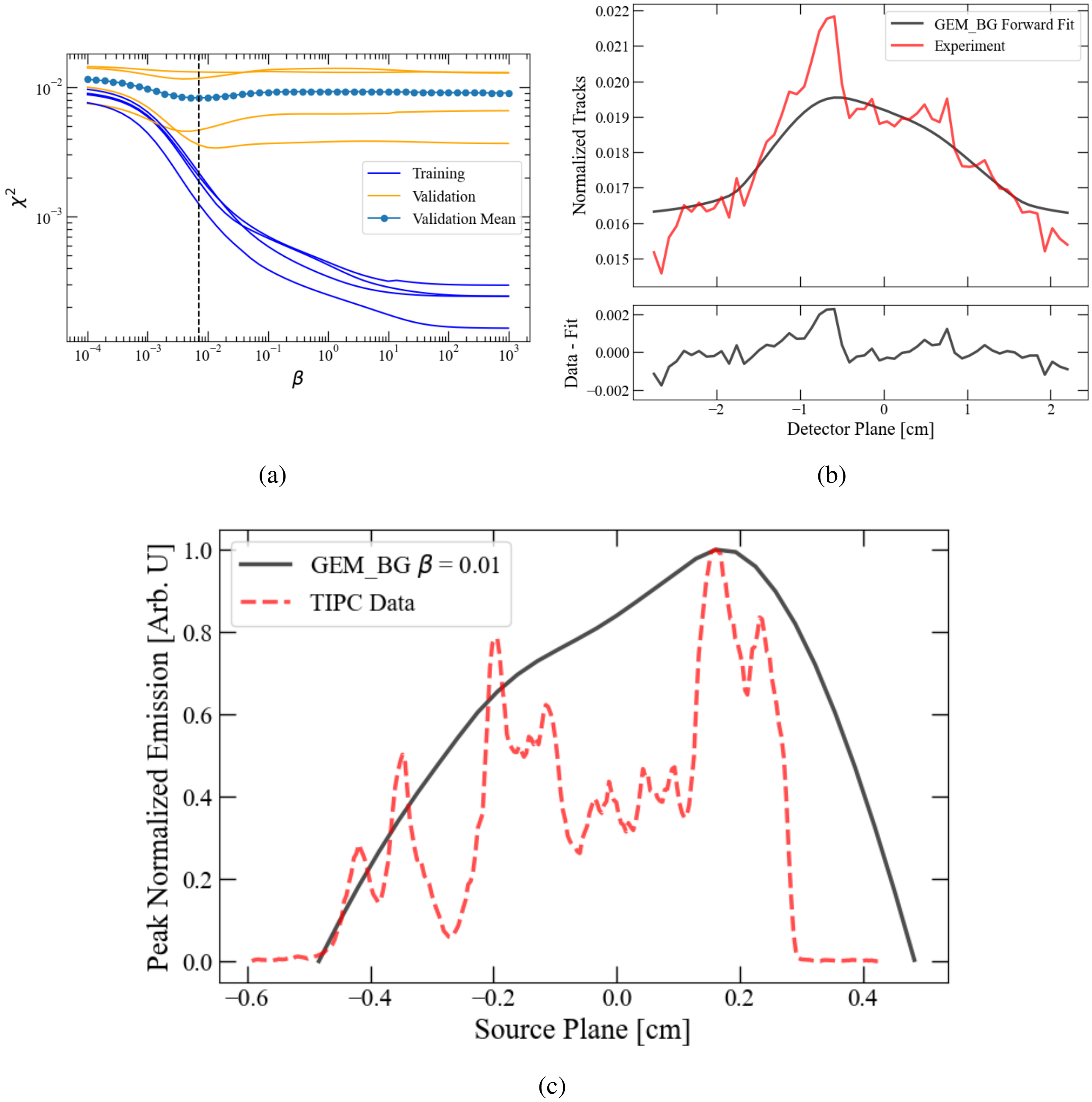

Figure 5.7: GEM_BG image reconstruction of z3926. (a) k-fold cross validation results indicating optimal $\beta = 0.01$. (b) GEM_BG forward fit compared to experimental data and corresponding residual. (c) Peak normalized GEM_BG source reconstruction registered with peak normalized TIPC data indicating the optimal β is over-smoothing the solution.

5.3.2 K-Fold Cross Validation Flaw

Synthetic data was once again used to reproduce the effects seen in z3926 source reconstructions. As previously stated, over-smoothing is a common problem in image reconstruction methods which use regularization. However, this case appears to be an issue of the randomization of indices in the k-fold cross validation procedure, in conjunction with the low resolution of ODIN data. With a lower number of data points, distinct features of the axial data profile may not be included in one of the k training sets. An example of this is shown in Figure 5.8, where the randomized points of $k = 5$ folds are highlighted for a mixed frequency synthetic detector response. In this permutation of random indices, folds $k = 1$ (orange) and $k = 2$ (green) do not have any data points in the highest amplitude peak near -0.75 cm. This results in validation curves which produce a minimum chi-squared value with very smooth solutions, as they do not fit to the high frequency peak near -0.75 cm.

Figure 5.9 (a) highlights the validation curves corresponding to $k = 1$ and $k = 2$, which both have minimums at low β values. These curves then influence the validation mean curve, and can shift the minimum chi-squared to a lower β value. Figure 5.9 (b) shows the GEM solution for the mixed frequency synthetic source under-predicting the peak amplitude of the source. While this example does not significantly affect the solution, it highlights a flaw in the k-fold cross validation method which leads to over-smoothing of solutions.

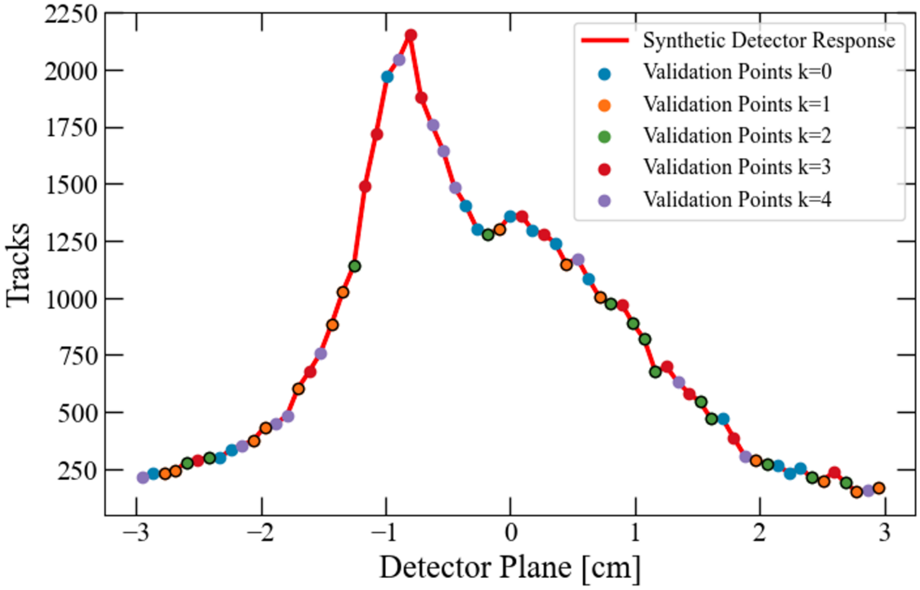

Figure 5.8: Mixed frequency synthetic response data with randomized indices split into k data folds. Datasets $k = 1$ (orange) and $k = 2$ (green) do not contain data points in the high frequency peak near -0.75 cm.

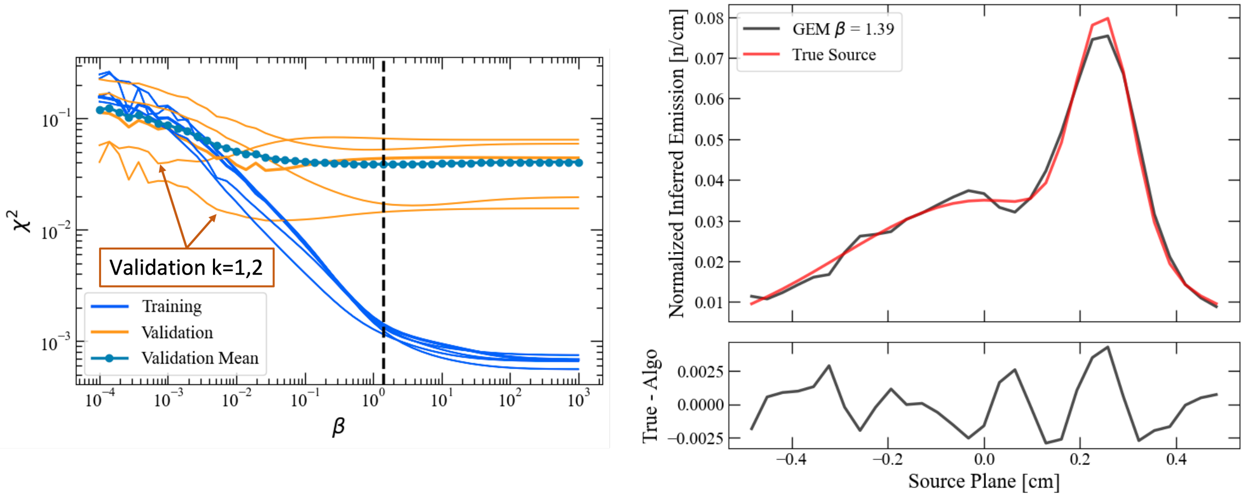

(a) (b)

Figure 5.9: Example of over-smoothing with Figure 5.8 data. (a) k-fold cross validation results indicating that validation sets $k = 1$ and $k = 2$ shift the optimal β to a lower value. (b) Mixed frequency synthetic GEM reconstruction compared to the true source and corresponding residual. The low β value under-predicts the peak due to the randomization of indices in the k-fold cross validation process.

5.4 2-D K-Fold Cross Validation

To eliminate the possibility of high frequency features in the data being excluded from one or more of the validation datasets, the 2-D data can be used for a k-fold cross validation. An example of this method on mixed frequency synthetic 2-D data is shown in Figure 5.10. Synthetic 2-D data was generated using the same method shown in Figure 2.5, with the exclusion of integrating the data across the non-resolving axis shown in Figure 2.5 (d) Instead the 2-D data is split into k folds then each is integrated along its non-resolving axis as shown in Figures 5.10 (b) and 5.10 (c), respectively. These datasets now contain data points along the entire of extent of the detection area, however, this comes at the sacrifice of lower counts and decreases the SNR of each data point. Performing the k-fold cross validation produces much more uniform training and validation curves as shown in Figure 5.10 (d).

A secondary convenience of this method is the repeatability of β selection. By removing the randomization of data point selection, the 2-D k-fold produces the same training curves, validation curves, and optimal β each time the algorithm is run. Since the columns of the 2-D data contain variation of the same axial profile, different permutations can be generated by randomizing the column order of the 2-D data. When introducing this randomness, there is less variance in the optimal β values when compared to the 1-D k-fold method as shown in Figure 5.11 (a) for n = 15 random permutations. This is also observed in mixed frequency synthetic data with an added background as shown in Figure 5.11 (b) for n = 15 random permutations. It is believed that the under-prediction of peaks in the GEM sensitivity study reconstructions is due to the large variance in β. Even with a spread distribution as shown in Figure 5.11, the mean GEM curves will be reduced as the lower β values have a greater influence on solution change than higher β values.

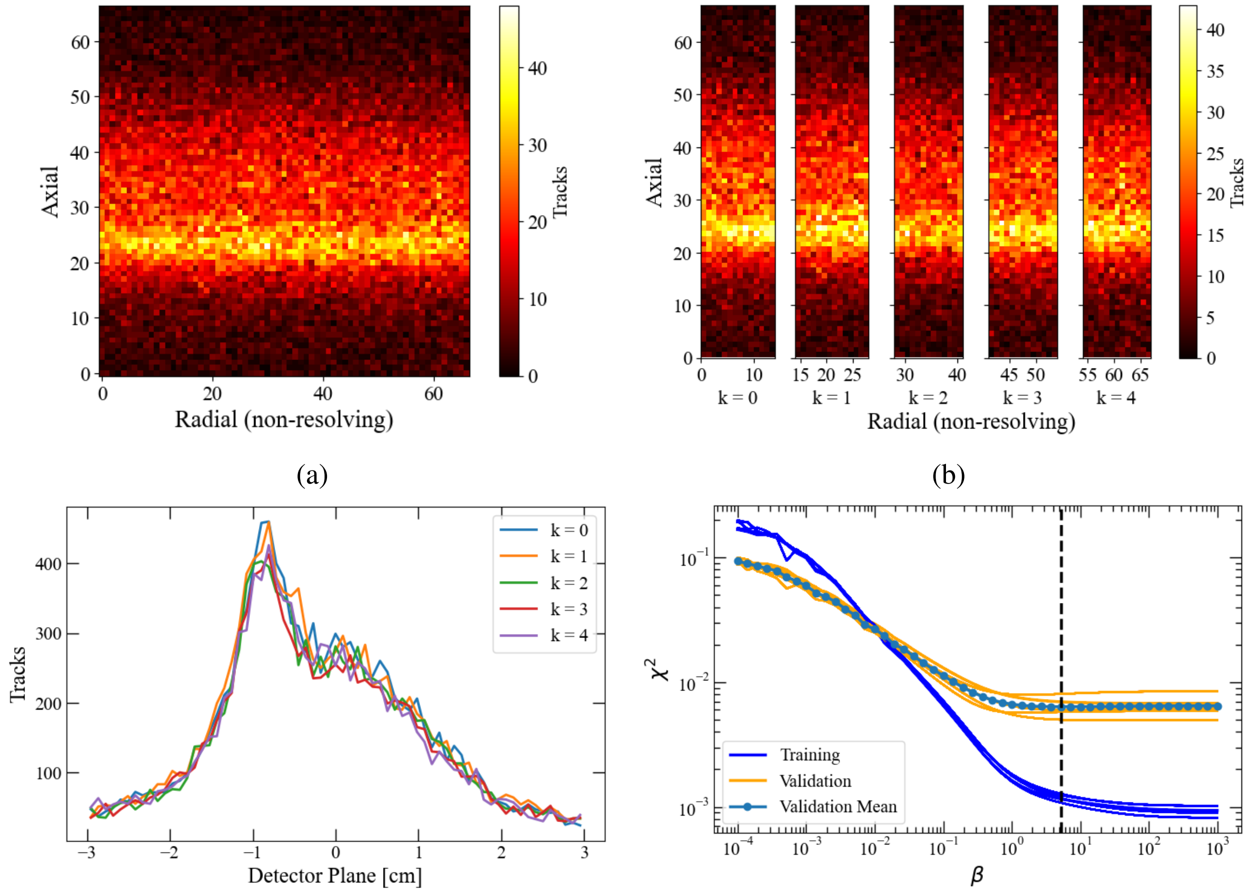

(a)

(b)

(c)

(d)

Figure 5.10: Example of 2-D k-fold cross validation with mixed frequency synthetic detector response data. (a) 2-D generated data from Poissonian sampling of the nominal 1-D detector response. (b) 2-D data split into $k = 5$ folds. (c) k 1-D training/validation sets generated by integrating each 2-D fold along the non-resolving axis. (d) Cross validation results with increased consistency in validation curves compared to 1-D cross validations.

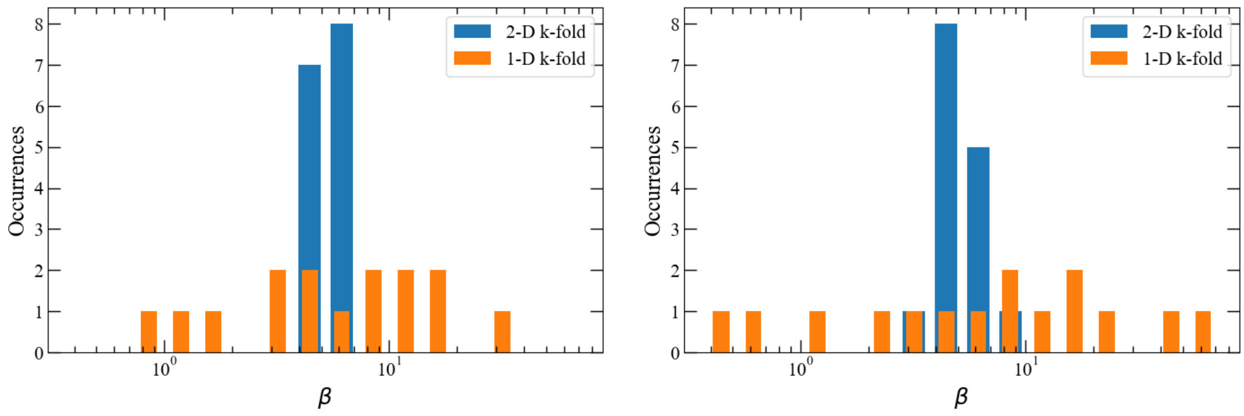

(a) (b)

Figure 5.11: β distribution of n = 15 1-D k-fold cross validations and column randomized 2-D k-fold cross validations for (a) Mixed frequency synthetic data using GEM and (b) Mixed frequency synthetic data with and added background using GEM_BG.

5.4.1 2-D K-Fold Experimental Results

The GEM_BG method was performed the 2-D data from z3289 and z3926 using the 2-D k-fold cross validation β selection. Data from z3289 produced an optimal β of 100, and has much more uniform validation curves shown in Figure 5.12 (a). Figure 5.12 (b) and 5.12 (c) show that there is minimal change in the forward fit and solution when compared to the previous solution with $\beta = 1000$ (Figure 5.6). As previously stated, higher β values have less influence on changes to the solution than lower β values.

There is, however, a stark contrast in the z3926 solution when selecting β with the 2-D k-fold cross validation. Validation curves in Figure 5.13 (a) have been improved as expected, but some still show minimums at very low β values. With $\beta = 7.2$, the forward fit in Figure 5.13 (b) has greatly improved compared to Figure 5.7 (b). The peak normalized solution registered with TIPC data in Figure 5.13 (c) now shows much better quantitative agreement. Past 0.3 cm there is a sharp drop off in the x-ray emission, which contrasts from the neutron emission. Currently, this is believed to be an artifact caused by an object blocking x-rays from this region before reaching the image plate.

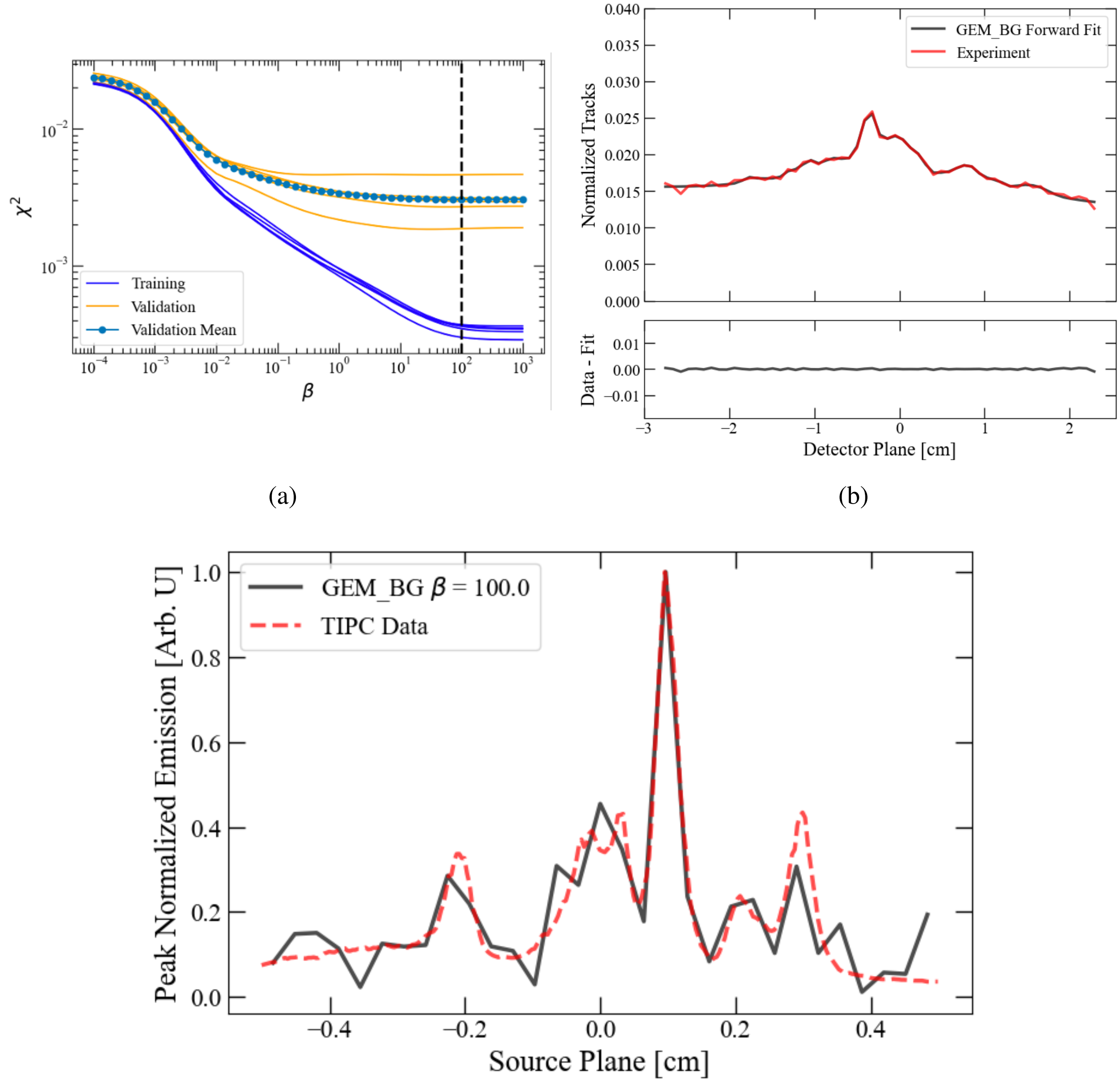

(a)

(b)

(c)

Figure 5.12: GEM_BG image reconstruction of z3289 using a 2-D k-fold cross validation. (a) 2-D k-fold cross validation results indicating optimal $\beta = 100$. (b) GEM_BG forward fit compared to experimental data and corresponding residual. (c) Peak normalized GEM_BG source reconstruction registered with peak normalized TIPC data indicating quantitative agreement. The sharp drop off near 0.3 cm in TIPC data is believed to an artifact caused by an object blocking x-rays.

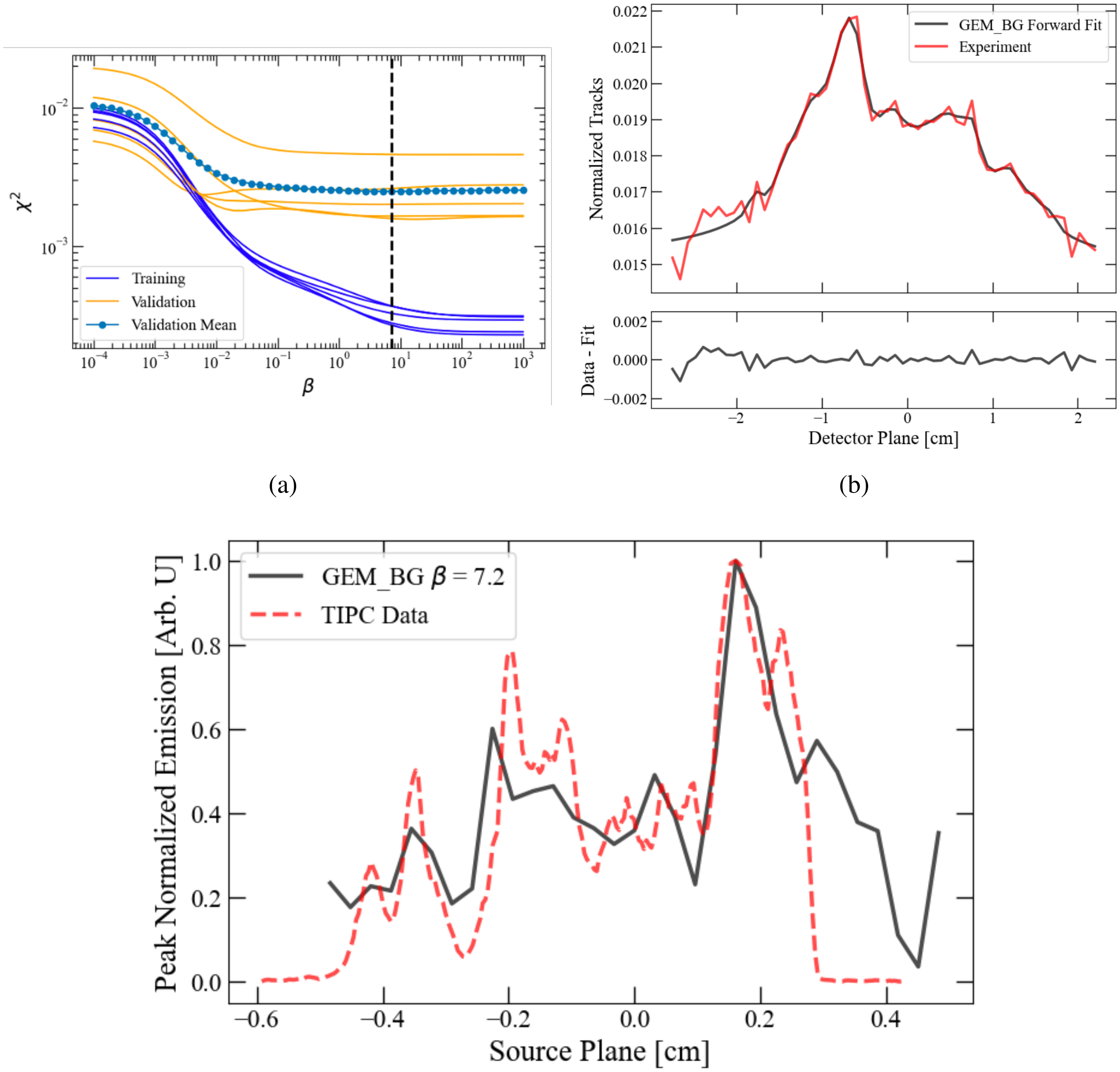

(a)

(b)

(c)

Figure 5.13: GEM_BG image reconstruction of z3926 using a 2-D k-fold cross validation. (a) 2-D k-fold cross validation results indicating optimal $\beta = 7.2$. (b) GEM_BG forward fit compared to experimental data and corresponding residual. (c) Peak normalized GEM_BG source reconstruction registered with peak normalized TIPC data indicating increase the optimal β from the 2-D k-fold cross validation does not over-smooth the solution.

5.5 Error Estimation

Section 4.2.2 described an approach to estimating the uncertainty of experimental data based on the central limit theorem. To implement this approach into the 2-D k-fold results steps remain the same with the exclusion of integrating the entire 2-D data into a 1-D axial profile. The resampling from the distribution based on the mean and standard deviation of each column generated a new 2-D dataset and the process described in the previous section is repeated n number of times. This method has been applied to z3289 and z3926 with $n = 20$ samples, as shown in Figures 5.14 and 5.15. Figure 5.14 (a) and 5.15 (a) show the GEM_BG data and TIPC data from Figures 5.12 (c) and 5.13 (c), in addition to the mean (solid blue line) and standard deviation (shaded blue area) of GEM_BG solutions from the 20 bootstrapped datasets. Both z3289 and z3926 show standard deviations which encapsulate the solution from the single original dataset.

Histograms of the optimal β values of the 20 solutions are shown in Figures 5.14 (b) and 5.15 (b). Looking at the dispersion of values, it is believed that this is the main cause of variance in solutions. As a comparison, error estimation was also tested by randomizing the columns of the original data. This led to different distributions in the k 1-D training and validation datasets, however, results showed no meaningful variation in the solutions. Optimal β values never reached below 50, leading to no significant change in the reconstructed profile.

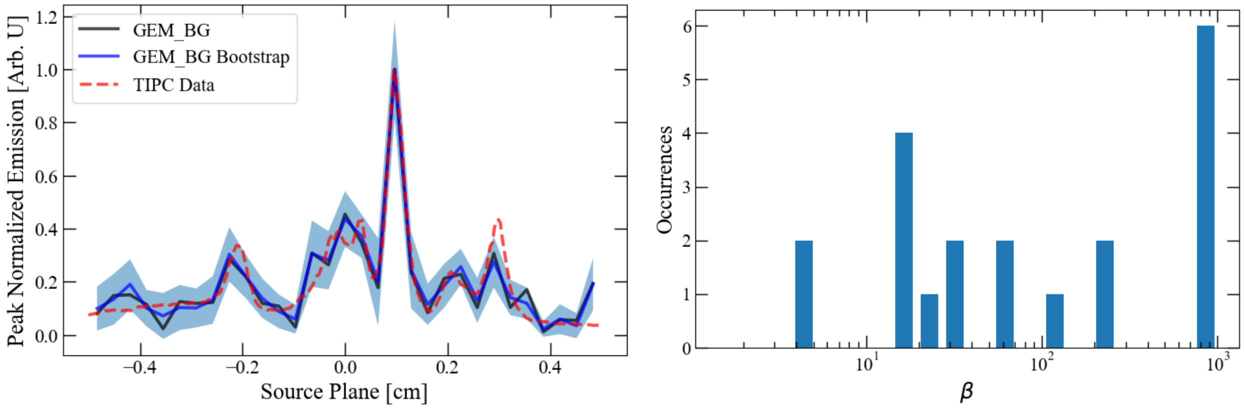

(a) (b)

Figure 5.14: z3289 ODIN reconstruction error estimation using CLT bootstrap method. (a) GEM_BG (black solid), TIPC (red dashed), and GEM_BG mean (blue solid) and standard deviation (blue shaded) of n = 20 bootstrapped datasets. (b) Optimal β distribution of bootstrapped reconstructions.

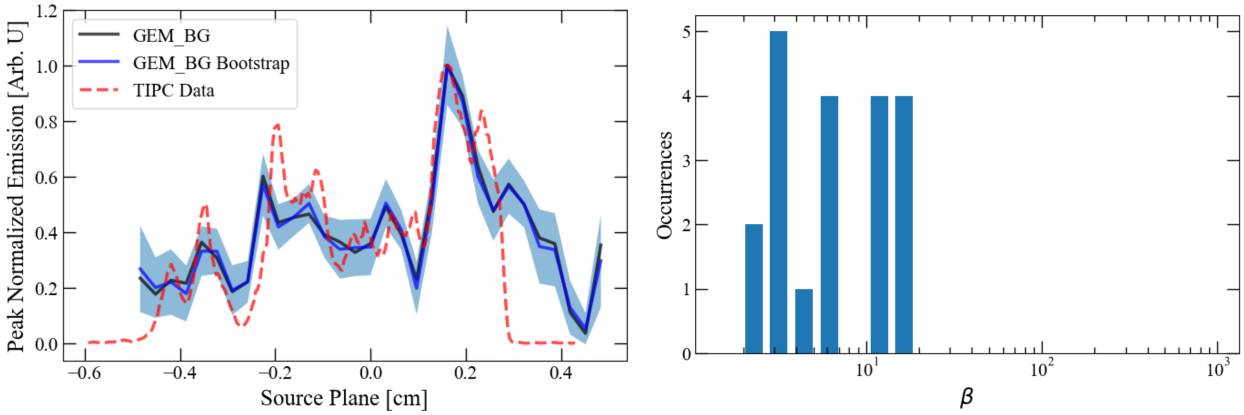

(a) (b)

Figure 5.15: z3926 ODIN reconstruction error estimation using CLT bootstrap method. (a) GEM_BG (black solid), TIPC (red dashed), and GEM_BG mean (blue solid) and standard deviation (blue shaded) of n = 20 bootstrapped datasets. (b) Optimal β distribution of bootstrapped reconstructions.

6. FUTURE SOURCE RECONSTRUCTION IMPROVEMENTS

Source reconstruction was shown to be successful when using a single CR-39 scan. However, the scans used were produced from some of the highest yield MagLIF experiments to date. This chapter describes possible approaches which may improve both high yield and low yield experiment reconstructions.

6.1 Implementation of Multiple CR-39 Scans

Multiple detector packages are placed in line with one another as previously described in Section 1.3.2. Each of the CR-39 pieces will contain the same spatial information and can be combined in various ways to improve the reconstructions. There are four to five detector packages used in each experiment, each containing a front and back CR-39 scan.

6.1.1 Summation of 2-D Data

One possible method to improve reconstructions is to simply accumulate the 2-D data and increase the total tracks in each detector bin. When using both front and back images, this can increase the SNR by a factor of $2n$, where n is the number of pieces of CR-39. It was shown in Section 4.2.1 that increasing the SNR reduces the variance of reconstructions. For a yield of 2×10^{12}, five scans summed together would create a SNR similar to that of one scan produced from a yield of 1×10^{13}. This approach has a significant benefit for the numerous ODIN datasets generated from lower yield MagLIF experiments.

6.1.2 Simultaneous Data Reconstruction

A second method that involves using multiple 2-D datasets is concatenating the 2-D data and solving for a single solution. This can be performed by using concatenated IRF matrices, background coefficient, and experimental data. The intrinsic background between each piece of CR-39 varies, and can be independently fit for each with this approach. With each added dataset, the number of data points fitted by a single solution will increase, however there is a sacrifice in SNR being unchanged. It is not clear at this time how the statistics will propagate through this method compared to the summation of 2-D data.

6.2 Data Processing Improvements

6.2.1 Discrimination Settings

All of the reconstructions thus far have been shown from CR-39 data produced from the back face. The contrast upper limit has been set to 10, but can be decreased further to better constrain tracks only to DD neutron generated tracks. This is at the expense of having a lower total number of tracks, but using multiple CR-39 scans may justify this sacrifice. Front face scans contain less total tracks and having a wider distribution of track diameter. Further investigation is needed to determine the optimal discrimination settings.

6.2.2 Detector Resolution Alteration

Bin size on the detector plane can also be changed to influence the number of tracks in each data point. As neutron yields increase, smaller bins can be used without sacrificing SNR. It is possible there is some threshold where further increase to the SNR does not significantly change the solution. At this point it may be beneficial to increase the number of data points for the solution to fit to.

6.2.3 Source Resolution Alteration

When determining the source reconstruction resolution, the previously calculated resolution was found to be $\sim$500 μm [8]. This corresponds to 21 source bins, over the 1 cm beryllium liner height. However, the approach of "super-resolution" image reconstruction can increase the resolution by using multiple images [46]. By using multiple images with spatial differences within a pixel size, a higher resolution source reconstruction can be performed. Reconstructions shown in this document have been set to a slightly higher resolution, $\sim$322 μm (31 source bins). Though we are using one 2-D image, the data columns across the non-resolving axis are essentially multiple snapshots of the same axial profile. Using multiple 2-D images for source reconstruction would further support this finer resolution.

6.3 β Optimization

The optimal regularization parameter, β, has shown to be challenging to determine as well as a key source of variance in some of the reconstruction methods. An alternative approach is needed to increase the accuracy and uncertainty quantification in this parameter. The current 2-D k-fold cross validation method is essentially picking a discrete maximum likelihood β value, and does not determine the probability distribution of β. Using a Bayesian inference method would allow β to be a hyperparameter solved for in the reconstruction method, similar to the background coefficients μ, and would generate a distribution of β to be sampled from for uncertainty quantification.

7. FIELDING RECOMMENDATIONS

The sensitivity analysis in Chapter 4 called attention to possible errors in the reconstructed source profiles from variations of fielding parameters. Edge effects caused by variations in these parameters were shown to be common when neutron emission was higher near the extremes of the source profile. While the experimental results from z3289 and z3926 appear to have peak emission away from the extremes, a uniformly emitting neutron stagnation column is what MagLIF strives to produce. As improvements to the uniformity of the axial neutron profile are made, variance in alignment parameters will begin to have a larger effect than shown in the sensitivity analysis. It is paramount that the fielding of ODIN is done properly if accurate source reconstructions are to be performed. This chapter outlines a few possible solutions to ensure this is achieved.

7.1 In-Chamber Alignment Measurements

It was demonstrated that incorrect alignments can alter the CR-39 detector response. While the effect may be drowned out by the uncertainty caused by statistical noise, more egregious errors may not be. If a few measurements were made of the most sensitive parameters during the in-chamber set up of ODIN, these values could be used to generate more accurate IRF matrices. This would especially be helpful in reducing edge effects produced by signal generated beyond the extent of the IRFs. Even if not being used for generating an IRF matrix, recording which parameters were irregular could provide insight into what type of source profile should be expected.

7.2 Monolithic Structure of Aperture and Detector Package

Another approach is to change the fielding of ODIN to be a monolithic structure. This would involve combining the aperture housing to the detector housing in order to reduce the variation in theta, one of the most sensitive parameters. It would also ensure correct alignment between the aperture and detector for each experiment. However, the main variation in Z_offset remains the shims placed under the target.

7.3 Magnification Optimization

Related to the monolithic structure for ODIN's aperture and detector would be the ability to change the D_slit parameter and alter the magnification. Both an increase and decrease in magnification have some merit on possibly improving data acquisition. The first is increasing the magnification in order to reduce the area between the outermost IRF peak and detector edge. We have shown that this area is the cause of edge effects due to intrinsic CR-39 background, reducing this area would lessen the need for background basis functions in the GEM_BG method.

By decreasing the magnification, a larger area between the outermost IRF peak and detector edge is produced. If the magnification becomes small enough, the decaying IRF tails would produce little signal in this area, allowing for a direct measurement of the CR-39 background. A background subtraction for each scan of CR-39 could then be performed.

8. CONCLUSIONS

MagLIF experiments have been performed on Sandia's Z facility in order to produce an $\sim$1 cm tall neutron emitting stagnation column. ODIN was developed to image the axial neutron emission profile of these experiments onto CR-39 nuclear track detectors. These neutron images contain spatial information valuable to understanding the underlying physical processes occurring in MagLIF implosions. Track discrimination and image scaling had been previously performed, but no image reconstruction had been attempted. The objective of this research was to improve the imaging of the spatial production of neutrons, by using image reconstruction methods.

An analytical forward model of ODIN's rolled edge aperture and CR-39 track detectors was developed and validated against MCNP simulations. The analytical model was employed to generate IRFs and synthetic datasets in order to test different image reconstruction methods. A sensitivity study of ODIN's fielding parameters was conducted to determine and quantify the effects of each parameter perturbation. Synthetic sources were reconstructed with LHS parameters to estimate the threshold of possible error in reconstructed sources. It was found that statistical noise is the predominant source of solution variance in low yield experiments, whereas parameter sensitivity becomes more significant as yields increase.

In neutron source reconstructions using experimental data, significant edge effects were observed, attributed to an unknown intrinsic background in the CR-39. These are mitigated by modifying the GEM reconstruction method and to include background subtraction using uniform and linear basis functions. The modified method, GEM_BG, was shown to be successful in reconstructions from single CR-39 scans. Through 2-D k-fold cross validation, the regularization parameter, β, was able to be consistently determined with each 2-D CR-39 scan. GEM_BG source reconstruction on experimental data from z3289 and z3926 showed quantitative agreement with TIPC x-ray data. Further improvements to image reconstruction include utilizing multiple CR-39 datasets and optimizing data processing steps. Fielding recommendations have been made to mitigate source reconstruction effects caused by parameter perturbations.

This research has established a repeatable and consistent method for reconstructing the axial neutron emission profile from MagLIF experiments. With a backlog of ODIN data awaiting analysis, future work will involve comparing reconstructed neutron profiles with other diagnostics to further support MagLIF experiment analysis. Specifically, comparing spatial neutron and x-ray yields along the stagnation column will aid in researching fuel mix effects.

REFERENCES

[1] D. B. Sinars, M. A. Sweeney, *et al.*, "Review of pulsed power-driven high energy density physics research on z at sandia," *Physics of Plasmas*, vol. 27, no. 7, p. 070501, 2020.

[2] H. Abu-Shawareb, R. Acree, P. Adams, *et al.*, "Lawson criterion for ignition exceeded in an inertial fusion experiment," *Phys. Rev. Lett.*, vol. 129, p. 075001, Aug 2022.

[3] D. N. Fittinghoff, N. Birge, and V. Geppert-Kleinrath, "Neutron imaging of inertial confinement fusion implosions," *Review of Scientific Instruments*, vol. 94, p. 021101, 02 2023.

[4] P. F. Schmit, P. F. Knapp, S. B. Hansen, M. R. Gomez, K. D. Hahn, D. B. Sinars, K. J. Peterson, S. A. Slutz, A. B. Sefkow, T. J. Awe, E. Harding, C. A. Jennings, G. A. Chandler, G. W. Cooper, M. E. Cuneo, M. Geissel, A. J. Harvey-Thompson, M. C. Herrmann, M. H. Hess, O. Johns, D. C. Lamppa, M. R. Martin, R. D. McBride, J. L. Porter, G. K. Robertson, G. A. Rochau, D. C. Rovang, C. L. Ruiz, M. E. Savage, I. C. Smith, W. A. Stygar, and R. A. Vesey, "Understanding fuel magnetization and mix using secondary nuclear reactions in magneto-inertial fusion," *Phys. Rev. Lett.*, vol. 113, p. 155004, Oct 2014.

[5] P. F. Knapp, P. F. Schmit, S. B. Hansen, M. R. Gomez, K. D. Hahn, D. B. Sinars, K. J. Peterson, S. A. Slutz, A. B. Sefkow, T. J. Awe, E. Harding, C. A. Jennings, M. P. Desjarlais, G. A. Chandler, G. W. Cooper, M. E. Cuneo, M. Geissel, A. J. Harvey-Thompson, J. L. Porter, G. A. Rochau, D. C. Rovang, C. L. Ruiz, M. E. Savage, I. C. Smith, W. A. Stygar, and M. C. Herrmann, "Effects of magnetization on fusion product trapping and secondary neutron spectra," *Physics of Plasmas*, vol. 22, no. 5, p. 056312, 2015.

[6] D. Yager-Elorriaga, M. Gomez, D. Ruiz, S. Slutz, A. Harvey-Thompson, C. Jennings, P. Knapp, P. Schmit, M. Weis, T. Awe, G. Chandler, M. Mangan, C. Myers, J. Fein, B. Galloway, M. Geissel, M. Glinsky, S. Hansen, E. Harding, D. Lamppa, W. Lewis, P. Rambo, G. Robertson, M. Savage, G. Shipley, I. Smith, J. Schwarz, D. Ampleford, K. Beckwith,

K. Peterson, J. Porter, G. Rochau, and D. Sinars, “An overview of magneto-inertial fusion on the z machine at sandia national laboratories,” *Nuclear Fusion*, vol. 62, p. 042015, Feb 2022.

[7] D. N. Fittinghoff, D. E. Bower, J. R. Hollaway, B. A. Jacoby, P. B. Weiss, R. A. Buckles, T. J. Sammons, J. McPherson, Leroy A., C. L. Ruiz, G. A. Chandler, J. A. Torres, R. J. Leeper, G. W. Cooper, and A. J. Nelson, “One-dimensional neutron imager for the Sandia Z facility,” *Review of Scientific Instruments*, vol. 79, p. 10E530, 10 2008.

[8] D. J. Ampleford, C. L. Ruiz, D. N. Fittinghoff, J. D. Vaughan, K. Hahn, B. Lahmann, M. Gatu-Johnson, J. Frenje, R. Petrasso, C. R. Ball, A. J. Maurer, P. F. Knapp, A. J. Harvey-Thompson, J. Fisher, P. Alberto, J. A. Torres, G. Cooper, B. Jones, G. A. Rochau, and M. J. May, “One dimensional imager of neutrons on the z machine,” *Review of Scientific Instruments*, vol. 89, no. 10, p. 10I132, 2018.

[9] P. Volegov, C. R. Danly, D. N. Fittinghoff, G. P. Grim, N. Guler, N. Izumi, T. Ma, F. E. Merrill, A. L. Warrick, C. H. Wilde, and D. C. Wilson, “Neutron source reconstruction from pinhole imaging at national ignition facility,” *Review of Scientific Instruments*, vol. 85, no. 2, p. 023508, 2014.

[10] S. A. Slutz, M. C. Herrmann, R. A. Vesey, A. B. Sefkow, D. B. Sinars, D. C. Rovang, K. J. Peterson, and M. E. Cuneo, “Pulsed-power-driven cylindrical liner implosions of laser preheated fuel magnetized with an axial field,” *Physics of Plasmas*, vol. 17, p. 056303, 03 2010.

[11] M. R. Gomez, S. A. Slutz, A. B. Sefkow, D. B. Sinars, K. D. Hahn, S. B. Hansen, E. C. Harding, P. F. Knapp, P. F. Schmit, C. A. Jennings, T. J. Awe, M. Geissel, D. C. Rovang, G. A. Chandler, G. W. Cooper, M. E. Cuneo, A. J. Harvey-Thompson, M. C. Herrmann, M. H. Hess, O. Johns, D. C. Lamppa, M. R. Martin, R. D. McBride, K. J. Peterson, J. L. Porter, G. K. Robertson, G. A. Rochau, C. L. Ruiz, M. E. Savage, I. C. Smith, W. A. Stygar, and R. A. Vesey, “Experimental demonstration of fusion-relevant conditions in magnetized liner inertial fusion,” *Phys. Rev. Lett.*, vol. 113, p. 155003, Oct 2014.

[12] W. E. Lewis, O. M. Mannion, D. E. Ruiz, C. A. Jennings, P. F. Knapp, M. R. Gomez, A. J. Harvey-Thompson, M. R. Weis, S. A. Slutz, D. J. Ampleford, and K. Beckwith, "Data-driven assessment of magnetic charged particle confinement parameter scaling in magnetized liner inertial fusion experiments on Z," *Physics of Plasmas*, vol. 30, p. 052701, 05 2023.

[13] D. C. Rovang, D. C. Lamppa, M. E. Cuneo, A. C. Owen, J. McKenney, D. W. Johnson, S. Radovich, R. J. Kaye, R. D. McBride, C. S. Alexander, T. J. Awe, S. A. Slutz, A. B. Sefkow, T. A. Haill, P. A. Jones, J. W. Argo, D. G. Dalton, G. K. Robertson, E. M. Waisman, D. B. Sinars, J. Meissner, M. Milhous, D. N. Nguyen, and C. H. Mielke, "Pulsed-coil magnet systems for applying uniform 10–30 T fields to centimeter-scale targets on Sandia's Z facility," *Review of Scientific Instruments*, vol. 85, p. 124701, 12 2014.

[14] P. K. Rambo, I. C. Smith, J. L. Porter, M. J. Hurst, C. S. Speas, R. G. Adams, A. J. Garcia, E. Dawson, B. D. Thurston, C. Wakefield, J. W. Kellogg, M. J. Slattery, H. C. Ives, R. S. Broyles, J. A. Caird, A. C. Erlandson, J. E. Murray, W. C. Behrendt, N. D. Neilsen, and J. M. Narduzzi, "Z-beamlet: a multikilojoule, terawatt-class laser system," *Appl. Opt.*, vol. 44, pp. 2421–2430, Apr 2005.

[15] A. J. Harvey-Thompson, M. Geissel, C. A. Jennings, M. R. Weis, M. R. Gomez, J. R. Fein, D. J. Ampleford, G. A. Chandler, M. E. Glinsky, K. D. Hahn, S. B. Hansen, E. C. Harding, P. F. Knapp, R. R. Paguio, L. Perea, K. J. Peterson, J. L. Porter, P. K. Rambo, G. K. Robertson, G. A. Rochau, C. L. Ruiz, J. Schwarz, J. E. Shores, D. B. Sinars, S. A. Slutz, G. E. Smith, I. C. Smith, C. S. Speas, K. Whittemore, and D. Woodbury, "Constraining preheat energy deposition in MagLIF experiments with multi-frame shadowgraphy," *Physics of Plasmas*, vol. 26, p. 032707, 03 2019.

[16] M. Savage, K. LeChien, W. Stygar, J. Maenchen, D. McDaniel, and K. Struve, "Overview and status of the upgraded z pulsed power driver," in *2008 IEEE International Power Modulators and High-Voltage Conference*, pp. 93–93, 2008.

[17] D. V. Rose, D. R. Welch, E. A. Madrid, C. L. Miller, R. E. Clark, W. A. Stygar, M. E.

Savage, G. A. Rochau, J. E. Bailey, T. J. Nash, M. E. Sceiford, K. W. Struve, P. A. Corcoran, and B. A. Whitney, “Three-dimensional electromagnetic model of the pulsed-power z-pinch accelerator,” *Phys. Rev. ST Accel. Beams*, vol. 13, p. 010402, Jan 2010.

[18] M. E. Savage, K. LeChien, M. Lopez, B. Stoltzfus, W. Stygar, D. Artery, J. Lott, and P. Corcoran, “Status of the z pulsed power driver,” in *2011 IEEE Pulsed Power Conference*, pp. 983–990, 2011.

[19] B. G. Cartwright, E. K. Shirk, and P. B. Price, “A nuclear-track-recording polymer of unique sensitivity and resolution,” *Nuclear Instruments and Methods*, vol. 153, no. 2, pp. 457–460, 1978.

[20] J. A. Frenje, C. K. Li, F. H. Séguin, D. G. Hicks, S. Kurebayashi, R. D. Petrasso, S. Roberts, V. Y. Glebov, D. D. Meyerhofer, T. C. Sangster, J. M. Soures, C. Stoeckl, C. Chiritescu, G. J. Schmid, and R. A. Lerche, “Absolute measurements of neutron yields from dd and dt implosions at the omega laser facility using cr-39 track detectors,” *Review of Scientific Instruments*, vol. 73, no. 7, pp. 2597–2605, 2002.

[21] F. H. Séguin, J. A. Frenje, C. K. Li, D. G. Hicks, S. Kurebayashi, J. R. Rygg, B.-E. Schwartz, R. D. Petrasso, S. Roberts, J. M. Soures, D. D. Meyerhofer, T. C. Sangster, J. P. Knauer, C. Sorce, V. Y. Glebov, C. Stoeckl, T. W. Phillips, R. J. Leeper, K. Fletcher, and S. Padalino, “Spectrometry of charged particles from inertial-confinement-fusion plasmas,” *Review of Scientific Instruments*, vol. 74, pp. 975–995, 01 2003.

[22] M. Gatu Johnson, “Charged particle diagnostics for inertial confinement fusion and high-energy-density physics experiments,” *Review of Scientific Instruments*, vol. 94, p. 021104, 02 2023.

[23] B. Lahmann, M. Gatu Johnson, J. A. Frenje, Y. Y. Glebov, H. G. Rinderknecht, F. H. Séguin, G. Sutcliffe, and R. D. Petrasso, “CR-39 nuclear track detector response to inertial confinement fusion relevant ions,” *Review of Scientific Instruments*, vol. 91, p. 053502, 05 2020.

[24] C. J. Werner, J. S. Bull, C. J. Solomon, Jr., F. B. Brown, G. W. McKinney, M. E. Rising, D. A. Dixon, R. L. Martz, H. G. Hughes, III, L. J. Cox, A. J. Zukaitis, J. C. Armstrong, R. A. Forster, III, and L. Casswell, "MCNP Version 6.2 Release Notes," Tech. Rep. LA-UR-18-20808, Los Alamos National Laboratory, Los Alamos, NM, USA, 2018.

[25] D. B. Pelowitz, J. T. Goorley, M. R. James, T. E. Booth, F. B. Brown, J. S. Bull, L. J. Cox, J. W. Durkee, Jr., J. S. Elson, M. L. Fensin, R. A. Forster, III, J. S. Hendricks, H. G. Hughes, III, R. C. Johns, B. C. Kiedrowski, R. L. Martz, S. G. Mashnik, G. W. McKinney, R. E. Prael, J. E. Sweezy, L. S. Waters, T. A. Wilcox, and A. J. Zukaitis, "MCNP6 User's Manual," Tech. Rep. LA-CP-13-00634, Los Alamos National Laboratory, Los Alamos, NM, USA, May 2013. This document is provided in the MCNP6 release package available from RSICC and is not accessible from the MCNP website. Code Version 6.1.

[26] K. D. Hahn, G. A. Chandler, C. L. Ruiz, G. W. Cooper, M. R. Gomez, S. Slutz, A. B. Sefkow, D. B. Sinars, S. B. Hansen, P. F. Knapp, P. F. Schmit, E. Harding, C. A. Jennings, T. J. Awe, M. Geissel, D. C. Rovang, J. A. Torres, J. A. Bur, M. E. Cuneo, V. Y. Glebov, A. J. Harvey-Thompson, M. C. Herrman, M. H. Hess, O. Johns, B. Jones, D. C. Lamppa, J. S. Lash, M. R. Martin, R. D. McBride, K. J. Peterson, J. L. Porter, J. Reneker, G. K. Robertson, G. A. Rochau, M. E. Savage, I. C. Smith, J. D. Styron, and R. A. Vesey, "Fusion-neutron measurements for magnetized liner inertial fusion experiments on the z accelerator," *Journal of Physics: Conference Series*, vol. 717, p. 012020, may 2016.

[27] C. L. Lawson and R. J. Hanson, *Solving Least Squares Problems*. Society for Industrial and Applied Mathematics, 1995.

[28] R. Bro and S. De Jong, "A fast non-negativity-constrained least squares algorithm," *Journal of Chemometrics*, vol. 11, no. 5, pp. 393–401, 1997.

[29] W. H. Richardson, "Bayesian-based iterative method of image restoration$*$," *J. Opt. Soc. Am.*, vol. 62, pp. 55–59, Jan 1972.

[30] L. B. Lucy, “An iterative technique for the rectification of observed distributions,” *The Astronomical Journal*, vol. 79, p. 745, jun 1974.

[31] A. J. Rockmore and A. Macovski, “A Maximum Likelihood Approach to Emission Image Reconstruction from Projections,” *IEEE Transactions on Nuclear Science*, vol. 23, pp. 1428–1432, Aug. 1976. Conference Name: IEEE Transactions on Nuclear Science.

[32] A. P. Dempster, N. M. Laird, and D. B. Rubin, “Maximum Likelihood from Incomplete Data via the EM Algorithm,” *Journal of the Royal Statistical Society. Series B (Methodological)*, vol. 39, no. 1, pp. 1–38, 1977. Publisher: [Royal Statistical Society, Wiley].

[33] V. Gelfgat, E. Kosarev, and E. Podolyak, “Programs for signal recovery from noisy data using the maximum likelihood principle: I. general description,” *Computer Physics Communications*, vol. 74, no. 3, pp. 335–348, 1993.

[34] T. Hebert and R. Leahy, “A generalized EM algorithm for 3-D Bayesian reconstruction from Poisson data using Gibbs priors,” *IEEE Transactions on Medical Imaging*, vol. 8, pp. 194–202, June 1989. Conference Name: IEEE Transactions on Medical Imaging.

[35] P. C. Hansen, “Numerical tools for analysis and solution of fredholm integral equations of the first kind,” *Inverse Problems*, vol. 8, p. 849, dec 1992.

[36] P. C. Hansen, “The l-curve and its use in the numerical treatment of inverse problems,” in *Computational Inverse Problems in Electrocardiology*, vol. 4, pp. 119–142, 01 2001.

[37] C. M. Bishop, *Pattern Recognition and Machine Learning (Information Science and Statistics)*. Berlin, Heidelberg: Springer-Verlag, 2006.

[38] M. D. McKay, R. J. Beckman, and W. J. Conover, “A comparison of three methods for selecting values of input variables in the analysis of output from a computer code,” *Technometrics*, vol. 21, no. 2, pp. 239–245, 1979.

[39] B. Efron, “Bootstrap Methods: Another Look at the Jackknife,” *The Annals of Statistics*, vol. 7, no. 1, pp. 1 – 26, 1979.

[40] T. Hastie, R. Tibshirani, and J. Friedman, *The Elements of Statistical Learning: Data Mining, Inference, and Prediction*. Springer series in statistics, Springer, 2009.

[41] M. Carlton and J. Devore, *Probability with Applications in Engineering, Science, and Technology*. Springer Texts in Statistics, Springer New York, 2014.

[42] G. F. Knoll, *Radiation detection and measurement*. New York: John Wiley & Sons, Cop, 2010.

[43] S. A. Ricketts, M. A. Mangan, P. Volegov, D. N. Fittinghoff, W. E. Lewis, O. M. Mannion, J. E. Morel, M. L. Adams, and D. J. Ampleford, "Neutron source reconstruction using a generalized expectation–maximization algorithm on one-dimensional neutron images from the Z facility," *Review of Scientific Instruments*, vol. 95, p. 033501, 03 2024.

[44] P. F. Knapp, M. E. Glinsky, M. A. Schaeuble, C. A. Jennings, M. Evans, J. Gunning, T. J. Awe, G. A. Chandler, M. Geissel, M. R. Gomez, K. D. Hahn, S. B. Hansen, E. C. Harding, A. J. Harvey-Thompson, S. Humane, B. T. Klein, M. Mangan, T. Nagayama, A. J. Porwitzky, D. E. Ruiz, P. F. Schmit, S. A. Slutz, I. C. Smith, M. R. Weis, D. A. Yager-Elorriaga, D. J. Ampleford, K. Beckwith, T. R. Mattsson, K. J. Peterson, and D. B. Sinars, "Estimation of stagnation performance metrics in magnetized liner inertial fusion experiments using Bayesian data assimilation," *Physics of Plasmas*, vol. 29, p. 052711, 05 2022.

[45] L. A. McPherson, D. J. Ampleford, C. A. Coverdale, J. W. Argo, A. C. Owen, and D. M. Jaramillo, "High energy X-ray pinhole imaging at the Z facility," *Review of Scientific Instruments*, vol. 87, p. 063502, 06 2016.

[46] S. C. Park, M. K. Park, and M. G. Kang, "Super-resolution image reconstruction: a technical overview," *IEEE Signal Processing Magazine*, vol. 20, no. 3, pp. 21–36, 2003.